**Improved Modelling of Long-Span
Highway Bridge Traffic Loading**
Dong Guo
Bachelor of Engineering (Honours)

A thesis submitted for the degree of Master at
Monash University in 2018
Department of Civil Engineering

COPYRIGHT NOTICE

ABSTRACT

Bridges play an important role in transportation systems. Their design is dependent on the estimated lifetime traffic load effect. Codes of practice stipulate the use of notional traffic load models to represent actual traffic. These load models are based on many conservative assumptions, which is prudent, but can be costly, especially when considering long-span bridges. To address some sources of conservatism in long-span bridge load modelling, three aspects are considered in this work:

- Axle-to-axle gap: Current methods of simulating congestion (the critical case for long-span bridges) make assumptions about the axle-to-axle gaps maintained between vehicles. There is a potential improvement in traffic load modelling if accurate data on axle-to-axle gaps can be obtained.
- Load model design: In the design of a notional load model for a code, both load magnitude and configuration are variables to consider. Most attention so far has been given to the load magnitude. This work proposes quantitative tools for the design of the load model configuration.
- Traffic load patterning: The load patterning stipulated by codes of practice may be impossible to achieve by real traffic. A less conservative more faithful approach for long-span bridges is developed here, which is especially useful for the assessment of existing bridges.

This dissertation aims to reduce the conservatism in load effect estimation for long span bridges. The major achievements are:

- A newly-proposed wheel detection algorithm which achieves high efficiency and accuracy, compared with other object detection algorithms.
- New vehicle and bridge influence line metrics are proposed to design the notional load model configurations, termed concentration and peakedness.
- A proposed traffic load patterning method is shown to improve the estimation of the actual load, compared to the traditional approach.
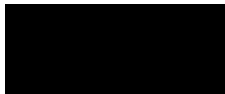
The implications of these results can be applied to current bridge design and assessment practices. They work together to provide more economical and efficient designs for bridges. Furthermore, the cost of maintenance and rehabilitation of existing bridges is considerable. The improved accuracy resulting from this work could help postpone, or even cancel such maintenance works.

Further research is recommended to analyse more complicated cases in traffic microsimulation, such as considering multi-lane factors, bidirectional traffic, and dynamic effects.

DECLARATION

This thesis contains no material which has been accepted for the award of any other degree or diploma at any university or equivalent institution and that, to the best of my knowledge and belief, this thesis contains no material previously published or written by another person, except where due reference is made in the text of the thesis.

Signature: ▮▮▮▮▮

Print Name: Dong Guo

Date: 30 May 2018

ACKNOWLEDGEMENTS

This study cannot be completed without the help of many people. The master thesis is both my affirmation of my two years of challenging work and my proud capital. At this moment, I would like to thank them.

To Dr Colin C. Caprani, I have been "bothering" you for three years if the undergraduate part counts. You consistently allowed this research to be my own work but steered me in the right the direction whenever you thought I needed it. I would like to thank you for the guidance, advice and help in these years. 1375 emails related to you tell everything. As my supervisor, you lead by example how to learn the knowledge. I hope you happy with the result.

To Monash University, it is my pleasure to study in this top-ranking university. The friendly staffs, comfortable environment and well-maintained facilities provide the best for me to complete the research. This research was also supported by Faculty of Engineering International Postgraduate Research Scholarship (FEIPRS).

To Junyong Zhou, thanks for your help during the half-year collaboration. You helped me to get a deeper understanding of the bridge engineering and provoked the new ideas when brainstorming with you.

To University College Dublin team, it was great teamwork. Everybody contributes the work. It is my honour to join you.

To my whole family, thank you for your unfailing concern, support and encouragement. You provide me with the best, and I hope you are proud of what I have achieved.

To Can Ji, as my girlfriend but not staying with me in Australia, you offered me the best understanding and infinite supports. The conversation with you every night is not much but indispensable. I love you!

To Chengyu Qiu, it was a wonderful time to study and have meals with you together. Though we do not research on the same topic, your humour influenced me a lot. Best wishes for your PhD study!

Finally, I would like to thank all those people helped and shared the knowledge with me.

CONTENTS

LIST OF FIGURES

LIST OF TABLES

TABLE OF ABBREVIATIONS

Abbreviations	Explanations
CF	Circularity Factor
CoV	Coefficients of Variation
DPM	Deformable Part-based Model
EUDL	Equivalent Uniformly Distributed Load
GEV	Generalized Extreme Value
GILF	Generalized Influence Line Function
GVW	Gross Vehicle Weight
HCT	Homogenous Congested Traffic
HLP	Heavy Load Platform
IDM	Intelligent Driver Model
IL	Influence Line
LE	Load Effect
MAD	Mean Absolute Deviation
MOBIL	Minimising Overall Braking Induced by Lane changes
NLM	Notional Load Model
OCT	Oscillating Congested Traffic
PWF	Pseudo-Wavelet Filter
SEV	Standard Extremal Variate
SGW	Stop-and-Go Waves
SIMBA	Simulation for Bridge Assessment
UDL	Uniformly Distributed Load
WIM	Weigh-In-Motion

CHAPTER 1
INTRODUCTION

1.1 Background

Long span bridges are essential to society's functioning. However, as costly assets, whether to be built or already built, it is imperative to construct or maintain them as economically as possible.

The current approach to estimate traffic load is contributing to very notable visible features on new bridges. For example, the newly opened (2017) Queensferry Crossing of the firth of Forth, Scotland, is a cable-stay bridge with two 650 m spans (Kite et al., 2011). The Eurocode load model was used in its design, with patterned traffic load causing significant bending moments in the central tower (Figure 1-1). As a result, it was necessary to overlap the stay cables at both mid-spans, to reduce the tower bending moment. As another example, the Norwegian Public Roads Administration is proposing a multi-span suspension bridge on floating supports to cross the Bjørnafjorden, as part of its efforts to remove ferries from its E39 route (Figure 1-2). This proposed bridge has three spans of 1385 – 1325 – 1385 m. Due to the longitudinal bending caused by patterned live loading, it was found necessary to introduce a longitudinal horizontal cable to connect the tops of each tower (Villoria et al., 2017b). This top cable is adding significant complexity to the design. It must be heavily tensioned to avoid going slack in the extreme scenario adding significantly to the foundation design and complexifies the combined wind and wave vibration design (Villoria et al., 2017a).

(a) Overlapping cables

(b) Central tower bending moment due to the traffic load patterned on one span

Figure 1-1. Design of Queensferry Crossing (after Jacobs and Arup, 2009).

Figure 1-2. Bjørnafjorden concept design (after Villoria et al., 2017b).

Of course, the approach to traffic load estimation does not only affect new designs but potentially has even worse implications for existing long-span bridges. For example, around 25% of the long-span bridges in North America are reaching the end of their 75-year design lives, and only 63% long-span bridges are reportedly in good condition (Maria et al., 2018). It estimated that the US's backlog of bridge maintenance is at US$123 billion (ASCE, 2017). Given the strong correlation between poor condition and reduced load capacity (Wang et al., 2011), if a more precise live load model and patterning method are used, many bridges may be found to be a safe as-is, and substantial portion of the maintenance or rehabilitation cost could be avoided.

1.2 Scope of the Work

The objective of this study is to improve the traffic loading estimation on long-span bridges. Precisely, we consider the improvement on the axle-to-axle gaps, the basis of the load models and the traffic load patterning method. In detail, with considering the previous works, the tasks are:

- Using existing object detection algorithms to detect wheels;
- Proposing a better solution to detect wheels with high accuracy and efficiency;
- Investigating the fundamental relationship among bridges, vehicles and its load effects (LEs);
- Developing a rational and convenient tool for the next-generation load model design;
- Illustrating the conservatism of the traditionally patterned traffic topology for long-span bridges;
- Putting forward a more rational proposal for traffic load patterning for long-span bridges.

The refined work on wheel detections involves three existing algorithms, including Hough Transform, Template Matching and Deformable Part-based Models (DPM) method, and newly proposed pseudo-wavelet filter-based (PWF-based) algorithm. In total, 80 cropped vehicle images are tested for each algorithm.

The relationship among bridges, vehicles and LEs are quantitative. Only bridge influence line (IL) features and vehicle load concentrations are discussed. We consider the six load models for the new load model development tool. They are Australian load model S1600 and M1600, European load model LM1, British load model in BS5400, American load model HL93 and Chinese load model in JTG-D60. The uniformly-distributed load (UDL) part of each load model is not considered, as there is no possible variation to its configuration other than magnitude, which is not the aim of the present study.

The load patterning work focuses on the long span bridges. As it is known that the governing condition for long-span bridges is congestion traffic, several types

of the congested traffic flows are considered in the traffic load patterning simulation. Multi-lane factors and dynamic interactions of the vehicles are not considered, and the congestion traffic is a unidirectional traffic.

In summary, this research examines the current loading on the bridge and the means of applying it. Better wheel detection algorithms supplement the work with better accuracy in traffic load estimations. The new 3D plot tool for load model design can help to compare the load models and design the load models with the actual traffic loads and ILs in a more rational manner. The innovative load patterning method not only significant benefits in the design of new bridges, but more probably in the assessment of existing bridges, where the costs of additional strength are significant.

1.3 Outline of the Thesis

Chapter 1 of this thesis is an introduction to the whole research. It briefly discussed the problems in the bridge loading estimation and thus, the motivation of the research. The objectives, scope of the work and the merits of the study are followed.

Chapter 2 reviews the previous algorithms for the object detection, including Hough transform, template matching and DPM method. International bridge design standards regarding the load model patterning and the load model history in Australia, China, Europe, UK and US are also introduced. It also listed some previous traffic simulation methods. A qualitative finding of the loaded length and loaded density is also included.

Chapter 3 presents the technical methodology that used in the study. The microsimulation tools involve the Intelligent Driver Model (IDM) and Minimising Overall Braking Induced by Lane changes (MOBIL) models. The in-house program Simulation for Bridge Assessment (SIMBA) is also discussed with typical input parameters. Several congestion types are introduced, and traffic loading is closely related to them. Generalized extreme value (GEV) distribution is introduced, and we used that to do the data extrapolation.

Chapter 4 gives the refined work about wheel location detection. A new image processing technique is proposed to detect wheels in variable light conditions. The proposed method is based on a PWF that amplifies circles, in conjunction with an algorithm that weights features in the image according to their circularity. This novel approach is compared to the Hough Transform, Template matching and DPM method previously developed.

Chapter 5 introduces new metrics to represent the shape of the IL and the concentration of the vehicle loads, termed peakedness and concentration, respectively. The relationship among bridges, vehicles and LEs is discussed, and six load models are also compared quantitatively. A design tool is developed for the load model design.

Chapter 6 firstly examines design standards' approach to load patterning. Traffic microsimulation is adopted to simulate the traffic flows on a generic 1200 m bridge. We consider the possible road topologies that might give rise to design standard loading patterns. The LEs results are extrapolated to 5, 75 and 1000 years, representing common assessment and design return periods respectively (Lipari et al., 2017). From these results, a rational and practical load patterning method is proposed, based on the real topologies obtained from a combination of congested and free flow traffic. Two case study bridges are then analysed based on the new traffic load patterning method.

Chapter 7 summarises the findings and concludes the research performed for the scope of the thesis. As well, it specifies the recommendations.
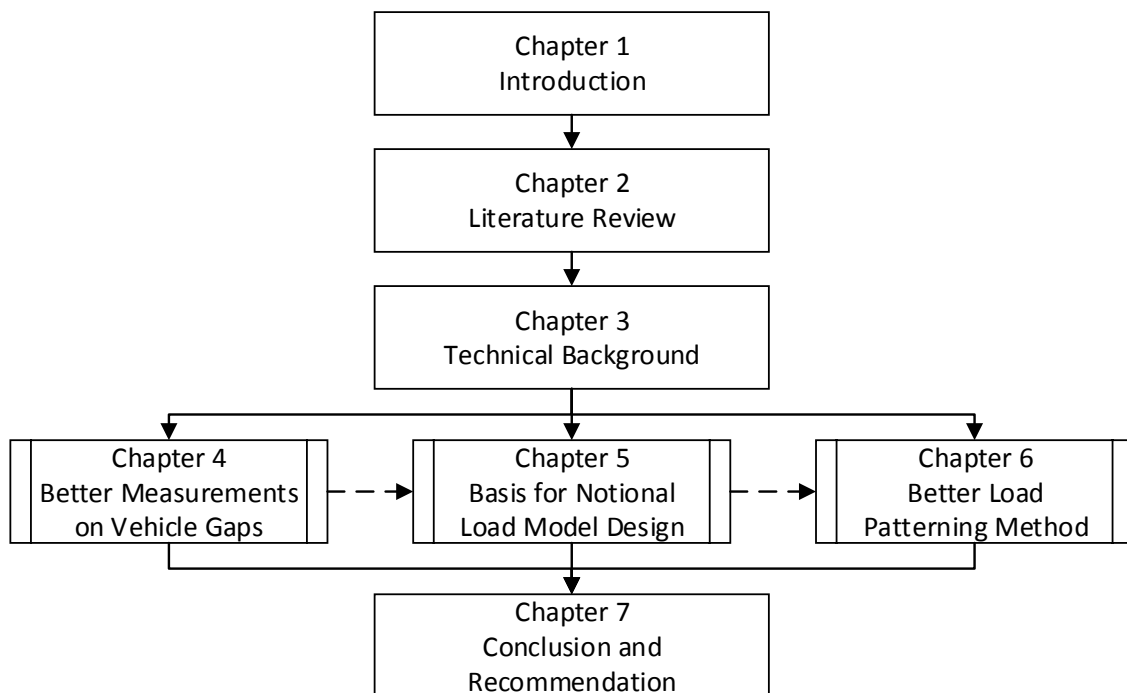
Figure 1-3. The dissertation flow chart

CHAPTER 2
LITERATURE REVIEW

2.1 Image-Based Wheel Detection

This part of the work was done in collaboration with other researchers. The contribution of this author made specific in Chapter 4.

Automatic identification of features in images is a much-studied area. Applications of feature identification are wide-ranging, including fingerprint identification, traffic monitoring, medical imaging, and face verification for security systems. For locating linear features, the Hough Transform is popular. This can also be generalised to locate other shapes, such as ellipses and circles. Where the feature to be identified is known exactly, such as in fingerprint recognition systems, Template matching is a quick and accurate method.

In traffic applications, several methods have been used to extract vehicle features. Some of these methods are specific to the camera used or the application, and so are not discussed in greater detail here. Examples are Hirose et al. (2009) and Chen et al. (2000). For traffic scenes where the lighting, location and appearance of wheels can vary, the most popular method is the Hough Transform. However, learning methods based on Template matching have also shown potential (Achler and Trivedi, 2004a; Achler and Trivedi, 2004b). The DPM (Felzenszwalb et al., 2008; Felzenszwalb et al., 2010) has been used for object detection in recent years.

2.1.1 Hough Transform

The Hough Transform is a popular method due to its general nature. Initially used for locating linear features in images, this transform can also be used to detect ellipses and circles and was generalised by Ballard (1981) to allow completely arbitrary shapes to be detected. Although the method does not need to be 'trained', the image must be converted to a binary, "edges-only" image using edge detection (Gonzalez et al., 2009). The Hough Transform is used by Frenze (2002) to count the number of axles on trucks. Success rates are variable and highly dependent on lighting conditions, ranging from 56% detection in poor light, to 93% in good light. False positives are twice as frequent as true wheel detections. The high rate of false positives is attributed to noise interference from edges belonging to non-wheel features. Fung et al. (2006) also use the Hough Transform for wheel counting. Although they do not report the success rates of

their application, they also comment on interference from edge points not belonging to wheels. Both studies comment on the computational intensity of the algorithm, which is of order $O(n^3)$, where n is the number of edge points detected.

2.1.2 Template Matching

Template Matching is a method that searches for a specimen, or template, the image within another image yielding a high response when the template is matched in the main image. It is often carried out using normalised cross-correlation (Lewis, 1995). It is particularly successful in cases where the appearance of the object to be found is known exactly. Examples of this are given by Sao and Yegnanarayana (2007), Baohua et al. (2009), and Liu et al. (2009). However, the appearance of an object such as a wheel is not known exactly. To overcome this difficulty, learning-based approaches to Template Matching have been used. Jiang and Lin (2006) make the case that, while learning based methods are robust in vehicle detection, they are restricted in classification due to the variety of vehicle types. Interestingly though, Achler and Trivedi (2004a; 2004b) develop a wheel detection method with success rate varying between 60% and 71%, although significant rates of false positives are reported. In their method, a pixel is convolved with several filters and the responses are normalized. These normalized responses are compared to templates of road and wheel responses. The templates are modelled using Gaussian Mixture Models and are constructed using a training set. Although not focused specifically on wheel identification, Jia et al. (2005) also use Gaussian Mixture Models as templates.

2.1.3 Deformable Part-based Model (DPM)

The DPM was proposed by Felzenszwalb et al. (2008) for object detection. It can be considered as an improved version of the Histogram Oriented Gradients (HOG) method (Dalal and Triggs, 2005). The algorithm compares the object and model using some parts. If these parts of the object are located close to the supposed locations and are stored in the model, the object is identified. The algorithm has been used for traffic applications, e.g., bicycle detection (Cho et al., 2010), pedestrian detection (Cho et al., 2012) and vehicle detection (Leon and Hirata Jr, 2012; Li et al., 2012; Li et al., 2015).

2.1.4 Summary

Despite positive indications from feasibility type studies (Fung et al., 2006; Radford and Houghton, 1989), except DPM, existing methods have not been widely found to provide sufficiently accurate and consistent detection when applied to large sets of traffic images (Frenze, 2002; Achler and Trivedi, 2004a; Achler and Trivedi, 2004b; Razavi et al., 2011). The poor accuracy reported in the literature for both Template Matching and the Hough Transform is supported by the work of Kastrinaki et al. (2003). In their review of commercial systems available for traffic monitoring, the authors conclude that most algorithms place more emphasis on high processing speeds than on the accuracy of the results. For the present application, it is vital that wheels be accurately identified through a succession of frames to determine the traffic characteristics contributing to bridge loading properly.

2.2 Load Model History

Before developing the numerical tools for notional load model (NLM) design, it is useful to describe the basis used for developing NLMs of notable international codes of practice of Australia, China, Europe, UK, and the USA. In each case, the historical background is briefly traced, so the evolution of load models is apparent. This puts the later work in context and illustrates the often-non-technical basis for the configurations of contemporary load models in particular.

2.2.1 Australia Standard

Taplin and Al-Mahaidi (1997) summarised the early load model history in Victoria, Australia. In the early 1900s, the design load was based upon a 15-ton steam roller. Later in 1926, the most severe case of a uniform load of 120 pounds per square foot or a vehicle load of 20 t was adopted. In 1936, the loading was increased to a combination of the two. From 1948, the Australian load model was based on the American standards (HS20-44/MS18). The American Association of State Highway and Transportation Officials (AASHTO) standard allowed for vehicles with a mass of up to 36 US tons (32.7 t) at that time.

In 1976, a new load model was adopted in Australia, called T44 loading (NAASRA, 1976). It is a revised version of the American load model (H20-S16), following truck surveys. The total weight was increased by one third and tandem groups replaced the trailer axles. T44 loading contains three parts; the T44 truck, L44 lane loading, and the Heavy Load Platform (HLP). The T44 truck is a five-axle truck with a total load of 432 kN, more closely reflecting real trucks at the time. L44 lane loading combines a uniformly-distributed load of 12.5 kN/m plus a point load of 150 kN. HLP is a total loading of either 320 tonnes or 400 tonnes. The standard requires that all bridges are to be designed for the worst of T44 or L44. HLP is to be applied to those required to carry exceptional heavy loads.

In the decades that followed, T44 loading was recognised as underestimating the real traffic loading on bridges. Heywood (1995) indicates that T44 loading becomes an average extreme daily event on short-span bridges. As bigger and more massive vehicles such as B-doubles and even B-triples, became desired by freight operators in Australia, it became necessary to design a new load model.

Pearson and Bayley (1997) defined several vehicles based on their densities [mass/(length×width×height)], such as S73 and L58 vehicle. These vehicles were believed to be the upper limits of the contemporary freight task, vehicle technology, safety, and pavement damage. They implicitly consider future increases in the allowable limits of vehicle loads. Heywood et al. (2000) proposed a new bridge load model to match LEs with those of the S73 and L58 vehicles. Monte Carlo simulation was also considered in the design, and a linear relationship was found between the total vehicle weight and vehicle length. Based on these, they designed the SM1600 configuration and UDL. From 2004, Australian Standards adopted the SM1600 load model (Standards Australia, 2017). Mainly, SM1600 consists of an 80-kN wheel load, a 160-kN axle load (two wheels), the M1600 moving traffic load and the S1600 stationary traffic load. M1600 and S1600 are shown in Figure 2-1.
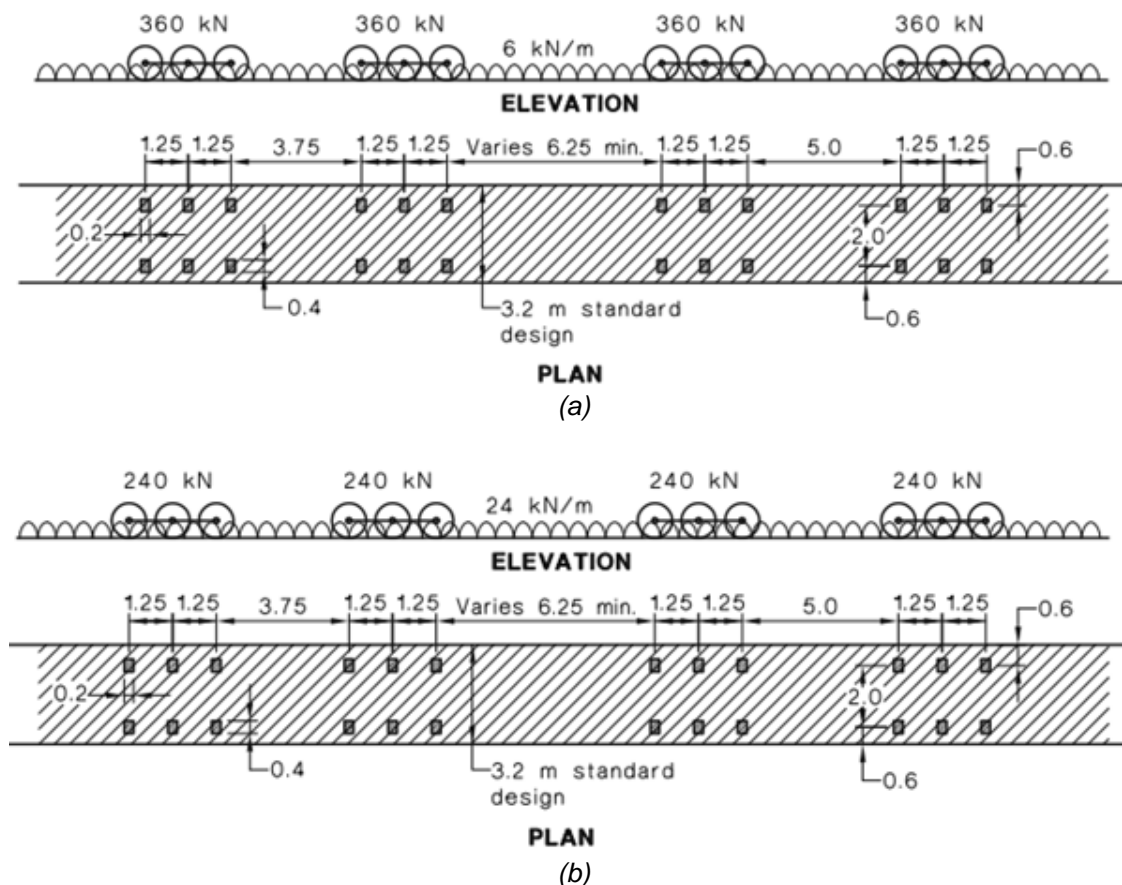
Figure 2-1. SM1600 in Australian standard (after Standards Australia, 2017): (a) M1600, for moving traffic, to which dynamic load allowance factors are applied; (b) S1600 for stationary traffic, more critical for longer spans.

2.2.2 China Standard

The early history of Chinese standard development is described by Wang (2005). Around 1940, there was no generally applicable load model, but different stipulated capacities for different bridge types. Later, due to the requirement for transporting heavy weapons, all bridges were required to carry at least 15 t vehicles. A road project design standard was published in 1954 which included five different vehicle load models. These load models are types of truck fleet, but the total loads are different. In the following years, significant revisions were made. However, the load models were not changed substantially, but some parameters adjusted such as: adding more vehicle load models for different road classes, adding equivalent vehicle conversion coefficient and extreme case loads. These changes were drive by increasing heavy traffic loads.

In the 1990s, the Ministry of Communications (MOC) commissioned reliability analysis for bridges and roads (Li et al., 1997). Weigh-in-motion (WIM) traffic data was collected in the main traffic lane at four typical sites. Special concern was given to the congested traffic scenarios and the overloading cases. Probability distributions for the LEs were determined and extrapolated to a 100-year design life. These LEs were then used to calibrate the proposed load model consisting of a concentrated load plus UDL.

In 2004, the MOC published a new standard JTG D60 – 2004 (MOC, 2004). The traffic load models were separated into two levels, based on road classes, and the checking loads removed. The load model comprises vehicle loads and lane loads. The lane loads are used for global structure analysis, while vehicle loads are for local stress analysis. In 2015, the lane load model was renewed with adjusted load values (MOC, 2015). Figure 2-2 shows the current lane load models. Q_k is 10.5 kN/m, and P_k is a piecewise function (ranging from 270 to 360 kN), depending on the span length.
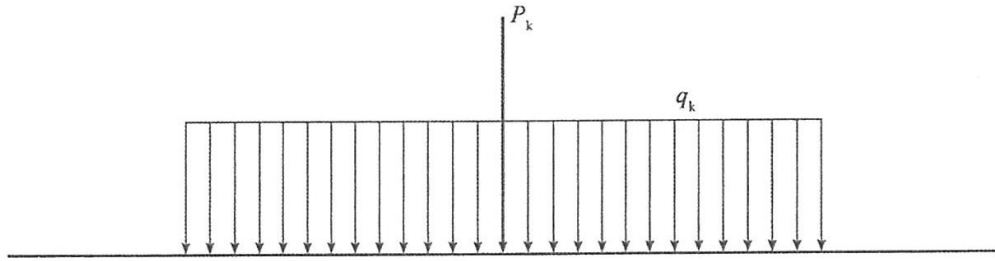
Figure 2-2. Lane load model in PRC's standard after 2015 (after MOC, 2015).

2.2.3 EU Standard

In 1975, the Commission of the European Community started to consider eliminating the cross-border obstacles in technical fields. A part of this generated the series of technical standards for the design of construction works in the member states of the European Economic Community (EEC) (Dawe, 2003)—the Eurocodes.

The development of the main highway bridge load model (LM1) in Eurocode 1 is thoroughly described in Bruls et al. (1996a). Based on Monte Carlo simulation of WIM data from across Europe, LEs for nine ILs, and spans up to 200 m were determined and extrapolated to a 1000-year return period. These actions are then considered the target values for the load model to replicate. Following consideration of various configurations and load values, a balance between accuracy and ease-of-use was sought, and the now well-known Load Model 1 was developed. Variation of the load model with increasing span was considered but neglected for simplicity. Multiple axles (point loads) were considered, but it was found that more axes did not improve the accuracy of the load model in matching the target LEs, and so for ease-of-use, the minimum number that gave acceptable accuracy was adopted. The resulting Load Model 1 is shown in Figure 2-3, for which the UDL and axle load magnitude for the first lane is 9 kN/m^2 and 300 kN when the national adjustment factors ("alpha-values") are taken as unity.
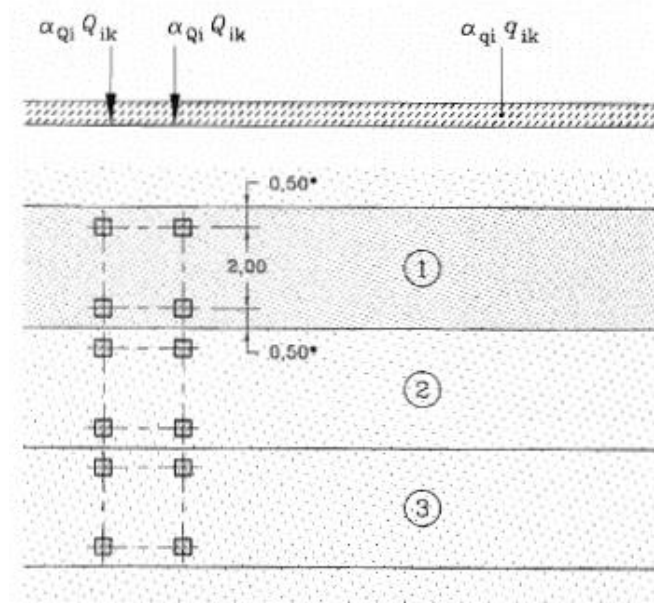
Figure 2-3. Load Model 1 in Eurocode (after CEN, 2003).

2.2.4 UK Standard

Henderson (1954) gives a brief history of bridge loading in the UK (In the following, note that 1 imperial ton is about 1.016 metric tonnes). In 1875, a live load for the design of new bridges was specified in the UK: "Professor Unwin suggested 'a load of 120 lb. per square foot (about 5.4 kN/m^2), or the weight of a heavily loaded wagon, say, 10 to 25 tons on four wheels'". Later, following the First World War, the Ministry of Transport (MOT) introduced the standard loading train in 1922. It consisted of a 20-ton tractor pulling three 13-ton trailers. Although the load model is based on a specific train of vehicles, it is quite inflexible due to the fixed values. Further, it proved very difficult for practitioners to use, due to the complexity of the computations. Consequently, in 1931, the MOT introduced the well-known MOT loading curve, consisting of a UDL that reduces magnitude with increasing span, and a knife-edge load (KEL)—a point load spread across the full width of the lane. This new load model greatly simplified the application of live loading in design.

In the 1950s, Henderson (1954) observed that some actual traffic differs from the standard loading train. He recommended categorising the traffic loads into "normal" traffic loads and "abnormal" vehicles for bridge design—now known as HA and HB loading respectively. Interestingly he notes that for modelling normal

traffic: "A train of vehicles or an equivalent distributed load is the obvious selection for this purpose. Trains have the disadvantage of being awkward and cumbersome to use; when they are specified it is common practice to compute equivalent uniformly distributed loads (EUDLs) as a substitute". Following calculations using some observations, Henderson (1954) updates the MOT loading curve somewhat. This loading curve was then subsequently fit with an equation (Dawe, 2003), and adopted into the well-known BS 5400: Part 2 (BSI, 1978). For HA loading, it consists of a lane UDL (Figure 2-4) and a KEL of 120 kN per lane.
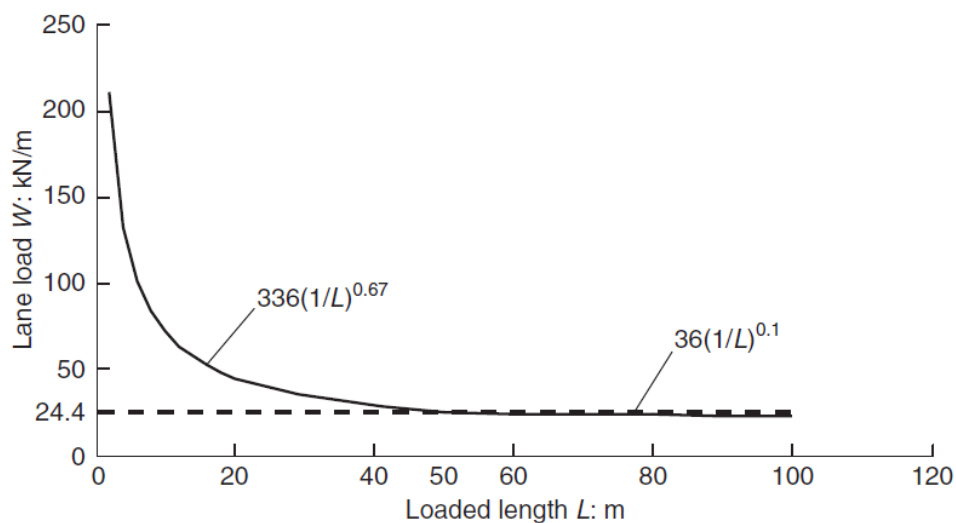
Figure 2-4. HA loading in British standard BS 5400 (after BSI, 1978)

2.2.5 USA Standard

Kulicki and Mertz (2006) summarise the development of the US load model. Specifications were first published in the transactions of the American Society of Civil Engineers (ASCE). Based on this, in 1931 the 1st edition of the American Association of State and Highway Transportation Officials' (AASHTO's) Standard Specification for Highway Design presented a truck and a group of trucks in the load design (AASHTO, 1931). For short bridges, a 20-ton single unit truck was used, termed H20. Lighter variations of this vehicle (H15 and H10) were also considered for secondary roads. Groups of H15 with occasional H20 were applied on longer bridges as a truck train.

In the early 1940s, the truck was extended to a tractor-semi-trailer (HS20) (AASHTO, 1944). This load model consists of 3 axles. The steering axle weighs 8 kips and other two on the semi-trailer weight 32 kips. The spacing on the semi-trailer varied from 14 to 30 ft., and the other spacing is fixed at 14 ft. Notably, HS20 was an idealisation and did not represent any real truck. This load model became the foundation of many load models around the world, including Australia as noted earlier.

In 1953, slight changes are made to the traffic lane numbers and multilane factors, but the HS20 truckload and lane loads remained unchanged. In the following years, only minor modifications to the axle weights and spacings were made.

To better reflect contemporary traffic, and the load and resistance factor (LRFD) design philosophy, a new code was introduced in 1994, designated the HL93 load model. This load model provided for more uniform safety for various groups of bridges, and consists of the HS20 truck plus a UDL (Nowak, 1993; Nowak, 1995). The model was derived from truck surveys, WIM measurements, and statistical extrapolations. Based on the measurements, simple span moments, shears and negative moments are calculated for various lengths. Then, extreme 75-year loads were determined by extrapolation. The primary objective in the design of the NLM was a uniform bias factor (mean-to-nominal ratio). HL93 includes both a design truck or tandem; and a lane load. Figure 2-5 illustrates current design truckload model in the USA.
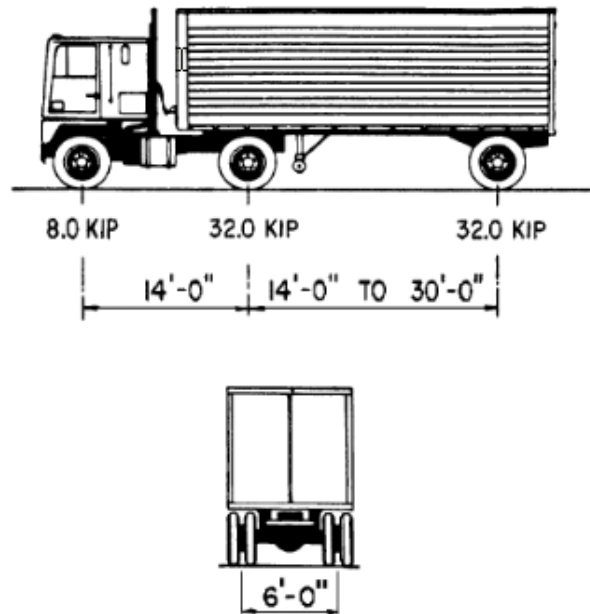
Figure 2-5. Design truck of HL93 load model (after AASHTO, 2017).

2.2.6 Summary

Based on the previous discussions, some general points about the development of load models can be made:

1. Load models are continually evolving. In the main, the reason for this is to better match both actual traffic configurations and load magnitudes.

2. Load models are often developed from small changes to a predecessor. Thus, modern load models can have a configuration and load magnitude like that from many decades past.

3. A typical modification to an existing load model is to increase the total weight. Configurations are rarely changed.

4. Most load model magnitudes have been developed to match LEs from surveys, measurements, or simulations of real traffic. In more recent years, statistical predictions of extreme LEs have been used as the target.

5. Most load model configurations have been selected to resemble real vehicles closely. BS5400 and the Eurocode are notable exceptions in which it is visually apparent that the load models are 'notional'.

6. Uniquely, the Australian load model is based on a hypothesized freight density and maximum truck volume, implicitly accounting for future growth.

Overall, it can be said that while the magnitude of a load model is calibrated to achieve target LEs of real traffic, the configuration of the load model originates from a far less objective basis. A quantitative tool to allow the investigation of both magnitude and configuration simultaneously should support future development of design code load models.

2.3 Load Patterning in Notable Codes

Australian load model SM1600 (Standards Australia 2017) requires that the UDL component be continuously or discontinuously applied to produce the most adverse effect. Similarly, the Eurocode (2003) load model LM1 requires that the UDL be applied only in the unfavourable parts of the influence surface. AASHTO (2007) also requires patterning the UDL of HL-93 to produce the extreme force effects. Many other codes follow the same approach (Figure 2-6).

Step1. Given a four-span bridge

Step2. Influence line

Step3. Load pattern on positive influence line region only
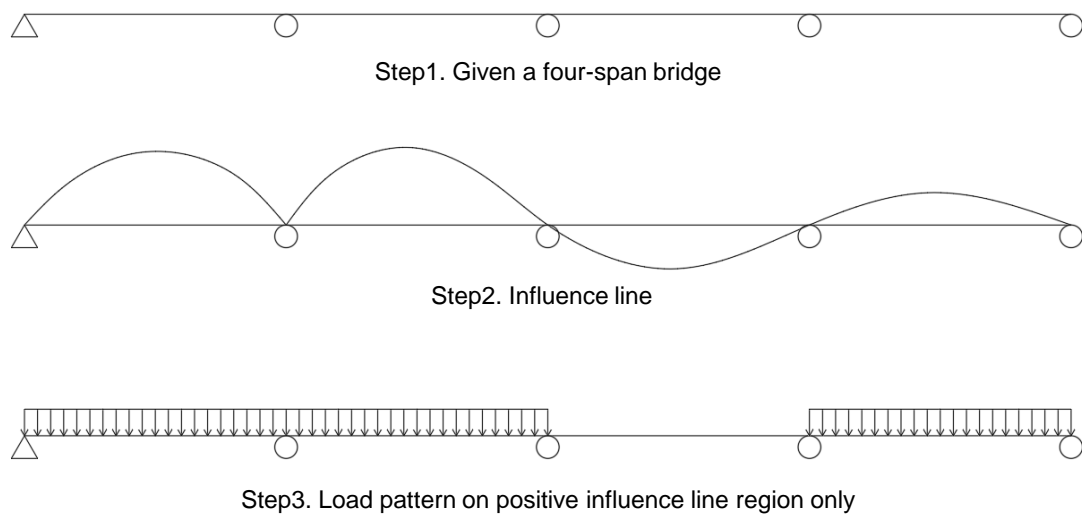
Figure 2-6. Traditional load patterning approach

The technical issue with the traditional load patterning approach is that it is a joint extreme: it combines both extreme loading values and an extreme loading topology. The probability of this joint occurrence of extreme loads and arrangements has not been studied in detail (as will be seen later). As a result, bridge engineering practice has followed a worst-case scenario approach combining extreme (lifetime) levels of loading in the extreme (lifetime) possible traffic topologies. Of course, it is reasonable that traffic is somehow patterned since it is apparently not uniformly distributed, due to truck queue formations and other traffic phenomena. Thus, a more rational basis for this patterning is required to estimate traffic action effects at the lifetime level.

2.4 Relationship between Load Magnitude and Loaded Length

A previous study indicated the relationship among bridge IL, vehicle loads and LEs. Burgoyne (1987) used a tide line to illustrate that vehicle length, or vehicle weight is not the only factor that causes the worst load case scenario on the bridges (See Figure 2-7). When the loaded length is smaller, the load density becomes more substantial (Figure 2-4). Therefore, the product of the loaded length and load density (i.e., load) will have a turning point, and it leads to a maximum LE. In other words, compact vehicles still can cause the worst LE even it is lighter than a long vehicle. However, the research is qualitative.
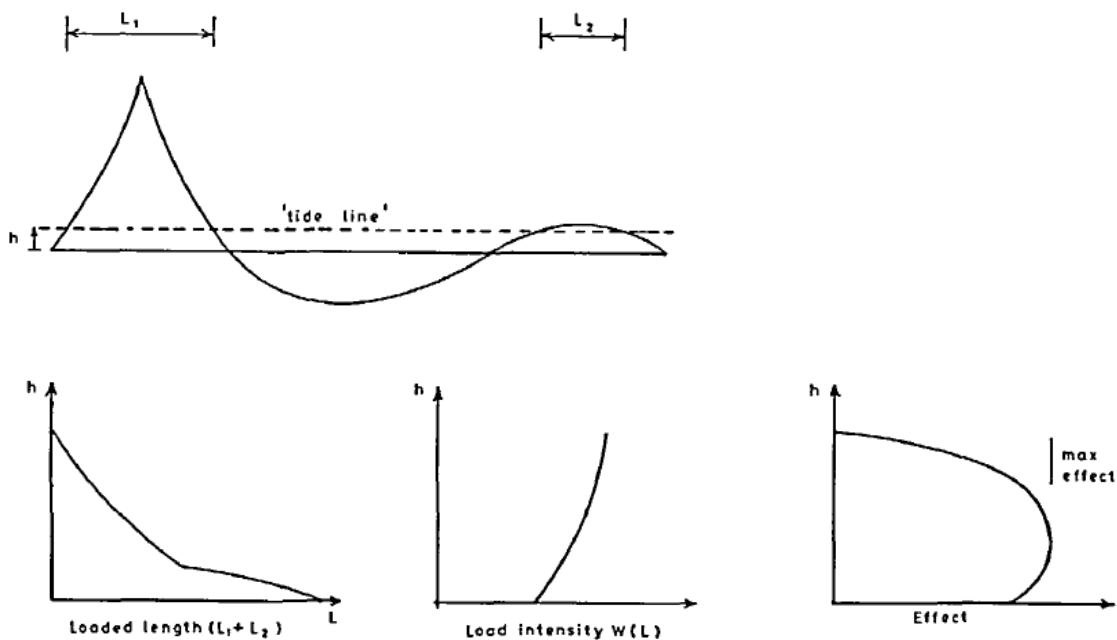
Figure 2-7. Tide line (after Burgoyne, 1987)

2.5 Traffic Loading on Long Span Bridges

Long span bridge traffic loading is governed by many vehicles, typically congested. A large amount of work is based on the mixed vehicles and fixed vehicle gaps (Ivy et al., 1954; Buckland, 1981; Ditlevsen and Madsen, 1994; Nowak et al., 2010; Caprani et al., 2012). Such work assumes cars and trucks are at a minimum bumper-to-bumper distance and the weight data is taken from on-site surveys or WIM data. However, WIM data is captured from free flow traffic as the sensor is not accurate in congestion (OBrien et al., 2015). Consequently, these measurements cannot be directly used for long span bridge loading. Another noticeable feature of the traffic is that the vehicle compositions can be entirely different across lanes. For example, car drivers tend to change lanes to overtake a slower moving truck. This results in slower lanes having a greater-than-average percentage of trucks. This phenomenon is more severe in the breakdown to congestion, often forming long truck platoons in the slow lane (Carey et al., 2017). Therefore, the direct use of a survey or WIM data can be unrealistic. To overcome this challenge, some researchers have used videos of congested traffic (Ricketts and Page, 1997; Nowak et al., 2010; OBrien et al., 2012). Many observations are obtained from the video, such as the typical traffic jam scenario, but it is difficult to get quantitative data.

A recent approach to overcome the problems with WIM noted above is the use of traffic microsimulation to create congested traffic from free-flow traffic measurements. In introducing IDM, Treiber et al. (2000) used traffic microsimulation to reproduce the observed congested patterns on the road. They introduced the bottleneck strength and discussed its relationship with the congested pattern types. Caprani and OBrien (2008) first used this microsimulation approach for bridge traffic loading. Later, Caprani et al. (2016) verified the relationship between bottleneck strength and congested traffic patterns. They used microsimulation to analyse the LEs of multi-lane traffic. Counter to the prevailing wisdom, it is found that the full-stop traffic is not the worst case of the bridge loading. Instead, slow-moving traffic can return the highest loading event, because there is more opportunity for critical vehicle arrangements to occur.

Not much work has been done to consider patterned traffic loading. Zhou et al. (2015) considered patterned traffic LEs for multi-span large bridges. In this study, traffic on the beneficial parts of the IL is ignored. It is found that the LEs of patterned traffic can be up to 8 times that of normal congested traffic on the bridge, which indicates the magnitude of conservatism in current code approaches. Nevertheless, many engineers would propose that patterned traffic is intended to replicate situations such as traffic accidents, and other interruptions to normal vehicular flow. Only a few previous works have considered this aspect. Recently, Lipari et al. (2017) proposed an integrated approach to determine lifetime levels of traffic loading considering the probability of occurrence of traffic incidents incorporating the level of interruption to traffic flow (the 'bottleneck strength'). In doing so, they use traffic microsimulation to determine the traffic topology and resulting LEs for such incidents. This approach demonstrates that traffic microsimulation is a suitable tool to analyse the LEs due to hypothesised traffic incidents and their topology. This approach is therefore adopted in this study.

CHAPTER 3
TECHNICAL BACKGROUND

3.1 Traffic Microsimulation

Microsimulation models consist of car-following models and lane-changing models to simulate the vehicle movements on the road. The position, direction, speed, axle arrangement, and other features of one single vehicle can be captured at any time, making it very useful for bridge loading studies. Microsimulation models are widely used in traffic analysis with different levels of accuracy in the recent years (Orosz et al., 2010). As the data is simulated, it should be calibrated and validated with real traffic to ensure its validity (Treiber et al., 2000). Brockfeld et al. (2004) compared ten different microsimulation models (including IDM) and found it is almost impossible to calibrate results to within 10%. The common range of differences is 14 to 16%, and the performances of various models are quite similar.

3.1.1 IDM & MOBIL Models

The IDM is a car-following model, developed by Treiber et al. (2000). The model is collision-free with several parameters to control single vehicle driving behaviour in one lane. Many research studies use IDM to simulate traffic, and the results can match the observed real traffic quite well (Treiber et al., 2000; Kesting and Treiber, 2008; Helbing et al., 2009; Chen et al., 2010; Caprani, 2012).

In the IDM, vehicle acceleration is given by:

$$\frac{dv}{dt} = a\left[1 - \left(\frac{v(t)}{v_0}\right)^4 - \left(\frac{s^*(t)}{s(t)}\right)^2\right] \qquad (1)$$

where a is the maximum acceleration of the current vehicle; $v(t)$ is the speed of the current vehicle at time t; v_0 is the desired speed of the current vehicle; $s(t)$ is the bumper-to-bumper gap from the current vehicle to the front vehicle at time t; and $s^*(t)$ is the minimum desired bumper-to-bumper gap at time t, given by:

$$s^*(t) = s_0 + Tv(t) + \frac{v(t)\Delta v(t)}{2\sqrt{ab}} \qquad (2)$$

where s_0 is the minimum bumper-to-bumper distance from the current vehicle to the front vehicle; T is the safe time headway; $\Delta v(t)$ is the speed difference between the current vehicle and front vehicle; and b is the comfortable

deceleration. Caprani et al. (2011) find that the driving behaviour could be inconsistent when front vehicle is much faster, and so they set a minimum gap distance s_0 as the lower limit in the simulation process, which is also used in this study.

Kesting et al. (2007) introduced a lane-changing model called MOBIL. Symmetric (US) or asymmetric (EU) passing rules can be implemented. In MOBIL, a vehicle will change lane if there is a sufficient acceleration advantage to be gained:

$$\tilde{a}_c(t) - a_c(t) > \Delta a_{th} + p\big[\big(a_n(t) - \tilde{a}_n(t)\big) + \big(a_o(t) - \tilde{a}_o(t)\big)\big] \qquad (3)$$

where Δa_{th} is the acceleration threshold, and $a(t)$ is the acceleration at time t, which is calculated by Equation (1). The subscript indicates the vehicle: old follower (o), new follower (n) and current vehicle (c) and the tilde identifies the situation after a hypothetical lane-changing. The politeness actor, p, controls how much consideration a driver gives to the impact of the lane change on surrounding vehicles' accelerations.

3.1.2 SIMBA and Parameters

Commercial traffic microsimulation software does not include bridge LE calculation. Consequently, since 2006, Caprani et al. (2012) developed a software program called SIMBA. It uses IDM and MOBIL for vehicle movements, coupled with LE calculation based on ILs at each time step of the simulation. The model input parameters are shown in Table 3-1. These parameters were used in previous works since they have been shown to replicate real traffic behaviour quite well (Treiber et al., 2000; Kesting and Treiber, 2008; Caprani et al., 2012; OBrien et al., 2015).

Table 3-1. IDM and MOBIL parameters.

Parameters	Car	Truck
Safe time headway, T(s)	1.6	1.6
Maximum acceleration, a(m/s^2)	0.73	0.73
Comfortable deceleration, b(m/s^2)	1.67	1.67
Minimum jam distance, s_0(m)	2	2
Elastic jam distance, s_1(m)	0	0
Desired velocity, v_0(km/h)	120±20%	80±20%
Acceleration exponent, Δ	4	4
Lane change politeness factor, p	0.2	0.2
Outside lane bias factor, ΔA_{bias}	0	0
Lane change threshold, ΔA_{th}(m/s^2)	0.4	0.4
Maximum safe deceleration, B_{safe}(m/s^2)	4	4

3.2 Congestion Types and Bridge Loading

Interestingly, traffic conditions are not a binary choice between free-flow traffic and congested flow traffic. Instead, traffic conditions occur on a spectrum, with many different forms of congested traffic, such as stop-and-go waves (SGW), oscillating congested traffic (OCT), and the most severe—homogenous congested traffic (HCT). The occurrence of these traffic types is mostly governed by the difference between demand and capacity, termed the bottleneck strength. Usually, the higher bottleneck strength, the lower road capacity in that region. Treiber et al. (2000) discussed the relationship between the bottleneck strength and different congestion types using a phase diagram (*Figure* 3-1). The bottleneck strength (or the dynamic capacity difference) ΔQ is the local decrease of the traffic capacity:

$$\Delta Q = Q_{out} - Q'_{out} \tag{4}$$

where Q_{out} is the maximum dynamic road capacity on the (hypothetically) free road and Q_{out}' is the maximum dynamic road capacity with the bottleneck in place. Bottleneck strength can be introduced locally by either directly decreasing the desired speed v_0 (e.g. a speed limit) or by increasing the safe time headway T (driver response time, leading to bigger desired gaps). Both can reduce the capacity of the road, but the latter is more effective (Treiber et al., 2000) and is used in this study. For the different level of the bottleneck strength, the traffic before the bottleneck can be different.
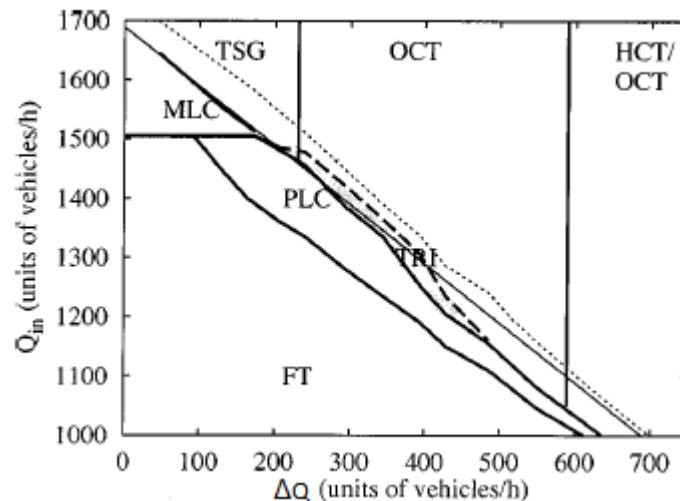
Figure 3-1. Phase diagram, indicating regions of the different traffic types (after Treiber et al., 2000). The main forms of traffic identified are: FT is free-flow traffic; TSG is triggered stop and go traffic (or SGW); OCT is oscillating congested traffic, and; HCT is homogenous congested traffic.

Caprani et al. (2012) and OBrien et al. (2015) studied different types of congestion and their influence on long-span bridge traffic LE. The densest type of traffic, HCT, is that intended to be replicated by bridge live load models. However, since it is a continuous heavy stream of traffic, it has little innate patterning.

Conversely, SGW has both dense and free-flow regions, and of course, these can become coincident with adverse and beneficial parts of an IL, leading to critical loading situation. Figure 3-2 illustrates this case. However, no previous research covering this point is known. This paper discusses the LE from SGW and uses it as a prototype to develop a proposal for traffic load patterning.
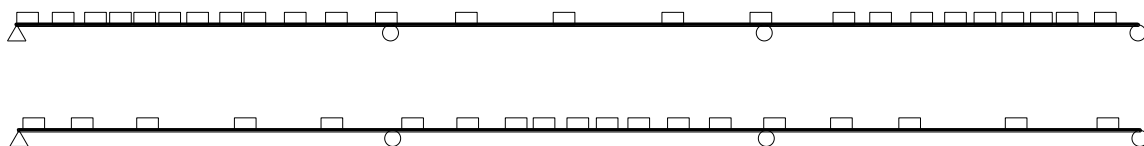
Figure 3-2. A graphic example of SGW. The rectangles are the moving vehicles on the bridge.

3.3 Extreme Value Statistical Extrapolation

Following extreme value theory (Castillo, 2012), GEV distribution is used to fit the block (hourly) maximum data of LE, given by:

$$G(x) = \exp\left[-\left(1 + \xi\left(\frac{x-\mu}{\sigma}\right)\right)^{-\frac{1}{\xi}}\right] \tag{5}$$

where x is the LE; μ is the location parameter; σ is the scale parameter; and ξ is the shape parameter. The LE at the required return period x^* is determined by:

$$x^* = G^{-1}\left(1 - \frac{1}{T_R}\right) \tag{6}$$

where T_R is the return period for the LE. It is considered that there are 250 working days per year (Caprani, 2005), and so $T_R = 250\,Y$, where Y is the required return period in years. A standard extremal variate (SEV) derived from the GEV distribution as: $\text{SEV} = -\log(-\log(1 - 1/T_R))$. For $Y = 75$ years, SEV = 9.84.
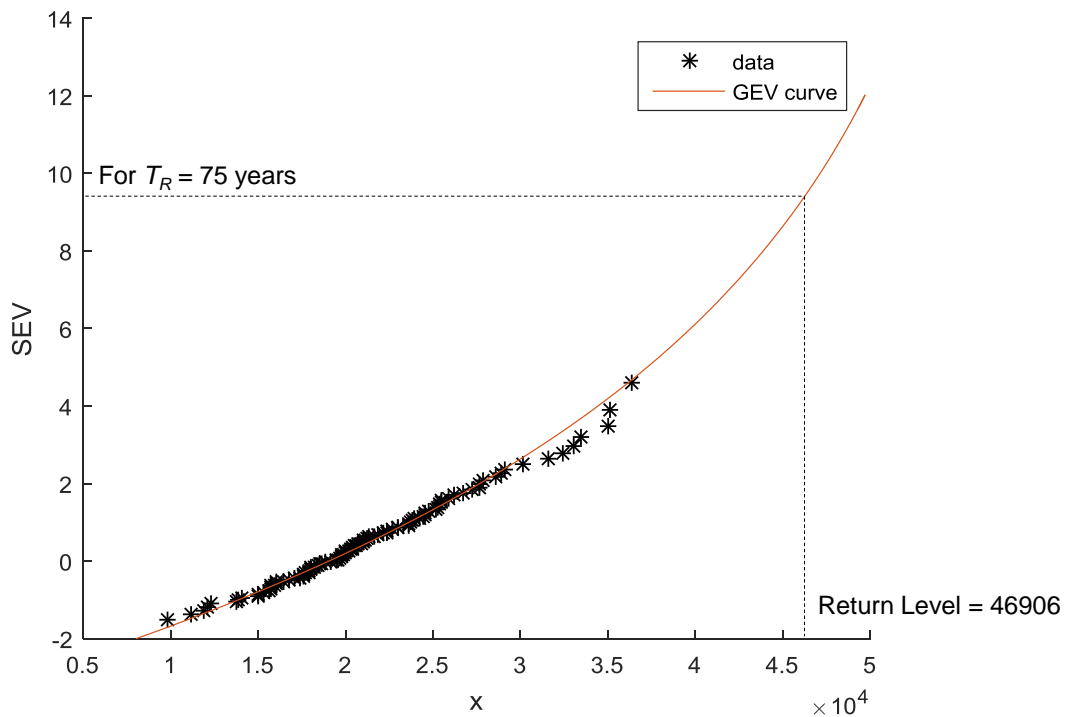
Figure 3-3. An extrapolation example on Gumbel paper

CHAPTER 4
BETTER MEASUREMENT OF VEHICLE GAPS

4.1 Statement of Contribution

The work described in this chapter is a collaboration between Dr. Colin Caprani, and Mr. Dong Guo of Monash University, Australia and Prof. Eugene J. OBrien, Ms. Serena Blacoe and Dr. Abdollah Malekjafarian at University College Dublin, Ireland. The author completed the work of the DPM, described in section 4.5. The collaborators worked on the Hough Transform algorithm, Template Matching Algorithm and developed the proposed PWF Algorithm, described in Sections 4.3 and 4.4.

4.2 Introduction

Among all the vehicle data, wheel locations are of importance as these are the locations at which the weight of the vehicle is transferred to the bridge. It is proposed that a vision system can provide the locations of the wheels of vehicles, regardless of the traffic state. Such a vision system will make it possible to track vehicles through successive frames to find the statistical distributions of axle-to-axle gaps in all types of traffic. This data is not currently available due to the limitations of existing data collection systems. Identifying wheels is a complex task. Wheels can vary in appearance between classes of vehicle and within a single class of vehicle.

This chapter illustrates the use of a camera to collect wheel location. A new image processing technique is proposed to detect wheels in variable light conditions. The proposed method is based on a PWF that amplifies circles, in conjunction with an algorithm that weights features in the image according to their circularity. This new approach is compared to the Hough Transform, Template matching and the DPM methods previously developed.

4.3 PWF-Based Algorithm for Wheel Detection

An overview of the proposed algorithm for the detection of circular objects is presented in this section along with the theoretical basis. Implementation details are given in section 4.4. The concept for this algorithm is based on wavelets, which amplify changes in signal (or colour) of a particular nature and can search for these changes at different scales. The PWF concept developed here amplifies changes in colour around the circumference of a disc or circle. The aim is to amplify circles and, hence, wheels. By using multiple PWFs of differing sizes, wheels of different size (or scale) can be amplified.

Following amplification using PWF, each point in the image is assigned a weighting based on its circularity. The circularity factor (CF) weights the location based on how closely the colour change matches that of an ideal circle or disc, which has an entirely consistent colour change along its circumference.

The combined filtering result is given by multiplying the PWF response for a location by its CF. This is carried out at every location in the image. Selection of an appropriate threshold allows for peaks in the combined result to be identified. These peaks correspond to the centres of wheels in traffic scenes.

4.3.1 Pseudo-Wavelet Filter (PWF)

The PWF is constructed in filter space, centred on the origin. Each location (*x*, *y*) of the filter space is described in polar coordinates, ρ and θ from the centre of the filter space. The PWF is based on the hyperbolic cosecant function and defined by:

$$F(x, y; r) = \mathrm{csch}(\rho - r) \qquad (7)$$

$$F_{min} \leq \mathrm{csch}(\rho - r) \leq F_{max} \qquad (8)$$

where *r* is the sought wheel radius and ρ is the radius represented by the point (*x*, *y*) with the centre located at the centre of the filter space: $\rho = \sqrt{x^2 + y^2}$. F_{min} and F_{max} represent thresholds to ensure that the filter only returns a non-zero response if there is a colour change around the circumference of a circle centred at the location. These thresholds are discussed in more detail in section 4.1.

Although the PWF shares many features with a wavelet, it cannot be directly scaled and so is referred to here as a pseudo-wavelet.

A three-dimensional image of the filter function is shown in Figure 4-1(a) and a section through the centre is shown in Figure 4-1(b). The purpose of the algorithm is to obtain a high response at a point for which there is sharp contrast around a circle centred on it. Using the hyperbolic cosecant allows for values outside the sought radius to be positively amplified and values inside the sought radius to be negatively amplified. If the values inside and outside the sought radius are the same, the result will be zero. By varying the sought radius, r, circles of different size can be amplified.

The response of a location (x,y) in the image to the PWF is calculated by convolution. The square filter is centred on the image cell (pixel) of interest. Each cell in the PWF overlaps a single image cell. The PWF response, R_{PW}, for the sought radius, r, is then given by:

$$FR_{PW}(x,y;r) = \sum_{x=1}^{n}\sum_{y=1}^{n}|F(x,y;r)I(x,y)| \qquad (9)$$

where n is the number of rows and columns in the square filter. This calculation is carried out for all points within the image. Because the algorithm must amplify all circular shapes, and not just dark shapes on a light background, the absolute value of the response is taken.

4.3.2 Circularity Factor (CF)

A CF is introduced to weight the PWF response of an image location according to how closely the colour change around the circumference resembles that of an ideal circle or disc. The CF is required because the PWF alone cannot distinguish between circles with modest intensity changes and non-circular shapes with regions of extreme intensity change.

For an area of the image space with the same dimensions as the filter space, the mean pixel intensity, $\bar{I}$, of the circumference at a radius r^+ is calculated, where r^+ is equal to a radius marginally larger than the sought radius, r. The reasoning for

using a slightly larger radius is that pixilation at the sought radius can cause artificially low circularity factors for true circles. This is explained later.

A location's CF is based on the standard deviation of the pixel intensities at r^+:

$$\sigma(x, y, r) = \sqrt{\sum_{\theta=0}^{2\pi} \frac{[I(\theta) - \bar{I}]^2}{N}} \tag{10}$$

where $I(\theta)$ is the pixel value at angle θ and N is the number of pixels at a radius r^+. The CF for a location (x,y) at the sought radius, r, is then defined as:

$$R_{CF}(x, y, r) = 1 - \frac{\sigma(x, y, r)}{\sigma_{max}} \tag{11}$$
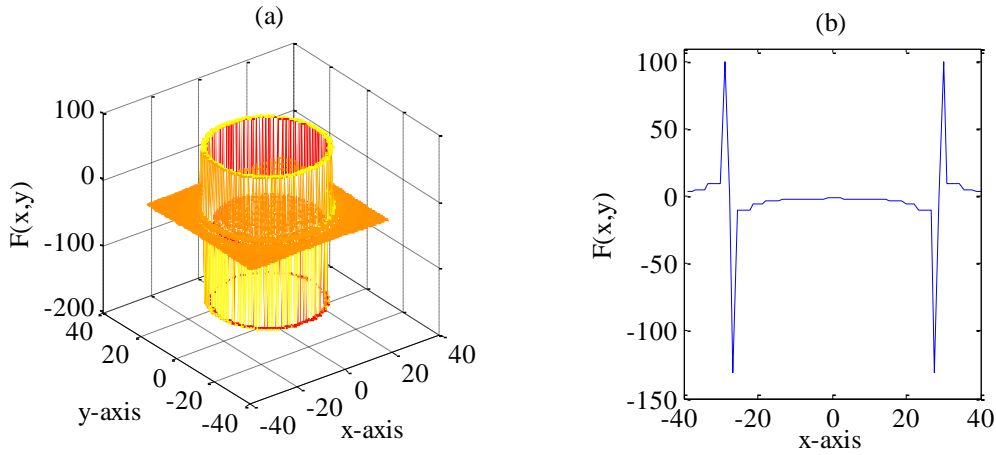
Figure 4-1. Proposed PWF in filter space.

This formulation ensures that the CF for a location lies between 0 and 1, where 1 indicates perfect circularity and 0 indicates no circularity. The maximum possible standard deviation, σ_{max}, represents a case where the pixels at r^+ alternate between black and white. The value of σ_{max} varies depending on the image representation (e.g. black and white, greyscale, etc.). It is given by:

$$\sigma_{max} = \frac{1}{2}\left[\sqrt{(I_{max} - I_{med})^2} + \sqrt{(I_{min} - I_{med})^2}\right] \tag{12}$$

where I_{max} and I_{min} represent the maximum and minimum possible pixel values respectively, and I_{med} is the median value of pixel intensity for the chosen image

representation. $\sigma_{\max}$ is a function only of the image representation and so will have the same value for all points in the image. Where the image representation denotes I_{min} as zero, as is common, Equation 12 simplifies to:

$$\sigma_{\max} = \frac{I_{max}}{2} \tag{13}$$

In 8-bit unsigned grayscale representation, $\sigma_{\max}$ = 127.5 and in 16-bit unsigned representation, $\sigma_{\max}$ = 32767.5.

4.3.3 Combined Response

The combined response is obtained by element-wise multiplication of the PWF response, R_{PW}, and the CF response, R_{CF} for the selected centre pixel at (x, y) and for the considered radius, r:

$$R(x, y; r) = R_{PW}(x, y; r) R_{CF}(x, y; r) \tag{14}$$

Real traffic contains wheels of many different sizes. Therefore, multiple radii must be considered, in the range r_{min} to r_{max}. The range of the radii of interest, $r_{min} \leq r \leq r_{max}$, is discretised into a number of radii of separation, Δr. The combined PWF-CF response at a location is calculated separately for each radius, $R(x, y; r)$. The result is a three-dimensional array, with each layer in the z-direction representing the combined response at a particular radius. These layers are summed to give the multiple radii or total combined response for each location:

$$R(x, y) = \sum_{r=r_{min}}^{r_{max}} R(x, y; r) \tag{15}$$

4.4 Implementation of Proposed Algorithm

4.4.1 Pseudo-Wavelet Filter (PWF)

Inherent to filtering of images are problems associated with borders. For pixels close to the edge of the image, part of the filter will be located outside the image borders. To overcome this problem and ensure that values of R_{PW} are obtained for all pixel locations, the image is 'padded' before being analysed (Gonzalez et al., 2009). The amount by which the image is padded is half the dimension of the PWF. Although the dimension of the filter is dependent on the sought radius, this does not cause problems when considering multiple radii. Responses to the filter are not calculated for pixels in the padded region, and so the response matrix is of the same dimensions as the original image.

Equation 8 describes the PWF limits the maxima and minima to high and low thresholds. These thresholds exist because the hyperbolic cosecant tends towards positive and negative infinity as $\rho - r$ tends towards zero. Maxima are limited to an empirically chosen high threshold of 100. To set a low threshold, the discretization of the filter space must be accounted for, and this is explained with reference to Figure 4-2. In this figure a light coloured pixelated disc is seen against a darker coloured background. The white circle gives the location of the high peaks in the PWF, r^+, and the black circle gives the location of the low peaks, r^-. From Figure 4-2 it can be seen that the low peaks form a ring inside the high peaks. Because of the larger radius, the ring of high peaks incorporates more cells then the ring of low peaks. The difference in the number of high and low peaks means that, if the high and low peaks have the same value, a non-zero response will be returned in areas of constant intensity. Further, this could cause a zero response where there is a change in intensity. In setting the capping thresholds, the difference in the number of high and low peaks must be considered so as to ensure a zero response where no change in intensity occurs. To do this, the absolute sum of the low peaks is set to equal the absolute sum of the high peaks, as given by:

$$F_{min} = \frac{N_{high}F_{max}}{N_{low}} \tag{16}$$

where N_{high} and N_{low} are the number of high and low peaks, respectively.
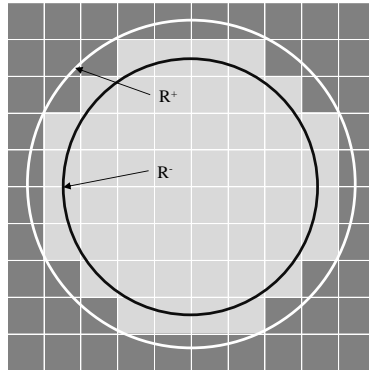
Figure 4-2. Locus of high and low PWF peaks.

4.4.2 Circularity Factor (CF)

The CF described in Section 4.3.2 is calculated at a radius r^+. The reason it is not calculated at the sought radius, r, is that the pixels at the colour boundary can be quite inconsistent: some of the pixels at the sought radius will be the outer colour, whilst some will be the inner colour, and some may be an intermediate colour. To account for this, the radius at which the CF is calculated is increased by two pixels ($r^+ = r + 2px$). This was empirically found to be as close to the boundary as possible without encountering pixelation problems.

The use of r^+ rather than r^- (a radius marginally smaller than the sought radius) is to eliminate the effect of hubcap features. If the wheels were perfect discs surrounded by tires, the use of either r^+ or r would not be critical. However, many hubcaps have spokes and cut-outs. These features are often present at the radius r and cause a low circularity for the location. By calculating at r^+, the CF for true wheels is high due to consistent colour around the circumference.

Finally, a threshold criterion is applied to the CF. If the CF for a centre point is less than 0.9, or 90% circular, the CF for that point is set to zero. Thus, only centre points of high circularity can be considered as wheel centres, regardless of the magnitude of the intensity change.

4.4.3 Illustrative Example

There are three inputs to the proposed algorithm – a grayscale image; the range of sought radii given in pixels, and a circularity threshold. To demonstrate the

proposed algorithm, a synthetic grayscale image is used. Only the correct radius is considered here, and the circularity threshold is set at 90%. The test image comprises a disc and half-disc of differing contrasts to the background, as shown in Figure 4-3(a). For (b)-(d), zero is shown as black with increasing values being shown as increasingly lighter shades of grey. As can be seen in Figure 4-3(b), the PWF response from the half-disc is higher than the response from the full disc. This is due to the significantly higher contrast between the half-disc and background (I(white) = 0; I(black) = 256; I(grey) = 195). Figure 4-3(c) shows the circularity factors for the image, before the threshold criterion of 90% circularity is applied. From this, it is clear that the full-disc shows much higher circularity than the half-disc. After the circularity threshold criterion is applied, the combined response is found from Equation 14 and the result shown in Figure 4-3(d). The only non-zero point that remains is the pixel at the centre of the full disc.

(a) Test Image

(b) PWF response

(c) CF response

(d) Combined response
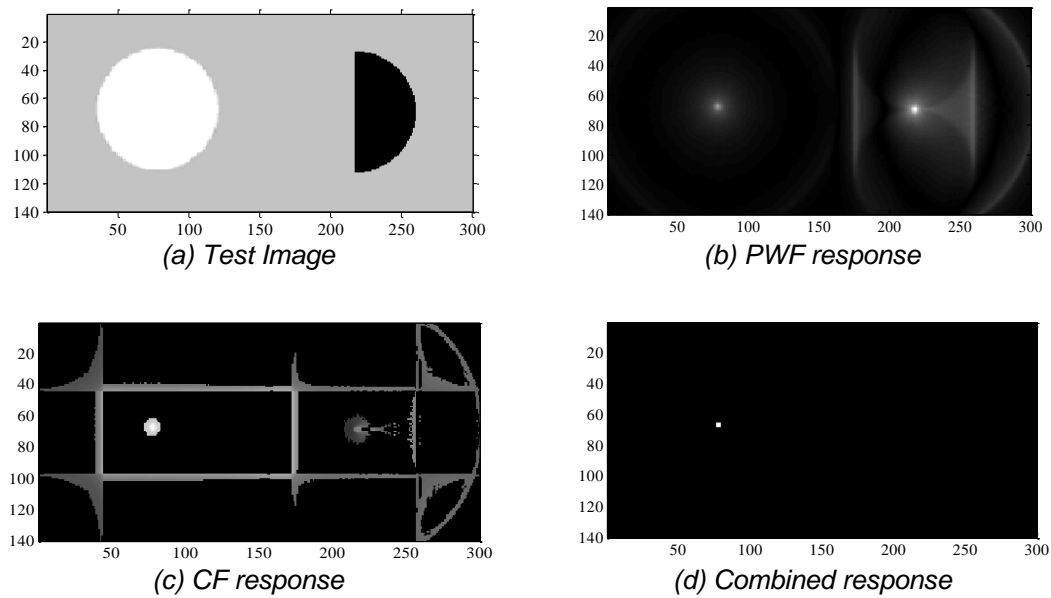
Figure 4-3. Illustrative example showing the sequence of operations.

4.5 Application and Accuracy

4.5.1 Image Acquisition

To test the proposed algorithm on real vehicles, a sequence of traffic containing 100 cars was recorded. The camera used is a monochrome IDS uEye LE USB camera, model number 1245M. It was used in conjunction with the Theia technologies SY125M lens, which is a wide-angle aspherical lens. This allows for a field of vision in excess of 165 degrees with minimal distortion. Images were captured at a rate of 10 frames per second with a shutter speed of 1/500 s. The camera was positioned approximately 2 m from the closest vehicle wheel and was focused on the near lane of traffic. The size of the captured images is 1280×1024 pixels, which is later cropped to a strip in which wheels are to be found. This typically results in images of the bottom of cars of 550×110 pixels. The site layout is shown in Figure 4-4.
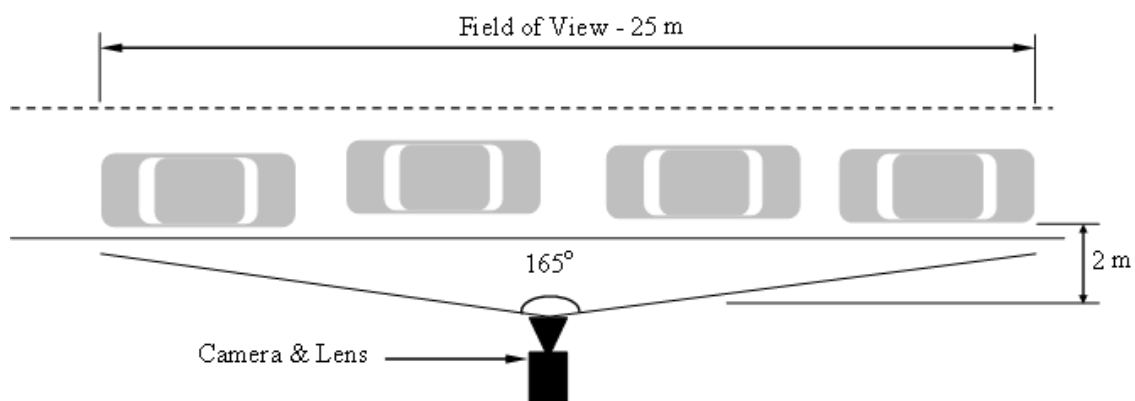
Figure 4-4. Site Layout.

In total 100 wheels were measured to select an appropriate radius range for the algorithm. The radii ranged from 17 cm to 26 cm. The average radius is 20.62 cm with a standard deviation of 1.54 cm. The algorithm operates in image space and so physical radii are converted as follows:

$$r_{pixels} = \frac{W_{image} r_{physical} f}{D W_{sensor}} \tag{17}$$

where r_{pixels} is the radius in image (or pixel) space; W_{image} is the width of the un-cropped image in pixels; $r_{physical}$ is the wheel radius in physical space; f is the

focal length of the lens; D is the distance between the wheel and the camera sensor, and W_{sensor} is the width of the camera sensor.

The lateral positioning of the vehicles can affect the imaged size of the wheels, so this was accounted for in the selection of the radius range. The radius range without accounting for lane wander is 24 pixels to 32 pixels. To allow for lane wandering of ± 0.5 m, the radius range was extended to encompass radii from 21 pixels to 35 pixels. This radius range was considered in increments of three pixels.

4.5.2   Algorithm Performance

The captured sequence of 100 cars is divided into sets of 20 and 80. The sequence of 80 cars is analysed using the Hough Transform, Template Matching, DPM and the proposed pseudo-wavelet-based algorithm. The set of 20 cars is employed as a training set for DPM. To carry out the Hough Transform, the images are first converted to binary "edges" images using the Canny edge detector (Canny, 1986). For Template Matching, synthetic templates are constructed and matched using normalised cross-correlation. A range of templates is constructed and shown in Figure 4-5. These templates have an inner disc representing the wheel or hubcap (intensity 127), with a dark ring around it representing the tire (intensity 0) on a lighter grey background (intensity 195). The radii of the inner discs are the same as the radii sought in the Hough Transform and the proposed algorithm, i.e. from 21 to 35 pixels, in increments of 3 pixels.

Figure 4-5. Synthetic templates used in evaluating the performance of Template Matching algorithm.

Three criteria are used for evaluating the performance of the algorithms:

1. Wheel location: The algorithms are deemed to have correctly located a wheel if a peak is detected within 15 cm on either side of the centre of the wheel. This tolerance is deemed acceptable on the basis that over the

2. False positives: If the peak occurs more than 15 cm from the wheel centre, a false positive is recorded. Recording false positives increases the number of axles recorded, potentially overestimating the load to which a bridge is subject.

3. Full vehicle identification: The third criterion evaluates the number of vehicles for which both wheels are correctly located without any false positives.

Two images are used here to demonstrate the application of the four methods. The first, a relatively easy one, is a case where the wheels have hubcaps that are clear and distinct. It is expected that all four methods should perform well. The identified wheel locations are shown in Figure 4-6. In this case, both the PWF and DPM algorithms and Hough Transform are deemed to have correctly located the wheels, with the PWF based algorithm having better accuracy. In the case of Template Matching, the dark bumpers against the light road more closely match the template than the black tire against the black car body. Although it may seem that the solution, in this case, is to modify the template so that the dark ring representing the tire is against a dark background, the template must be general enough to cope with many different colours of vehicles. This highlights a disadvantage with Template Matching methods because both the proposed PWF-based algorithm and the Hough Transform are effective in many colours of vehicles.

(a)

(b)

(c)

(d)

Figure 4-6. Example application of the four algorithms to a relatively easy image. (a) PWF-based algorithm, (b) DPM algorithm, (c) Hough Transform and (d) Template Matching.

A second, more difficult, image is also considered, shown in Figure 4-7. There are no hubcaps and the whole wheel is dark and difficult to distinguish from the tire, even by eye. Of the four algorithms tested, the DPM algorithm performs best. The PWF-based algorithm also performs well. Although neither wheel is located on the true wheel centre, both wheels are located within the 15 cm tolerance. The Hough Transform identifies a wheel at the edge of the 15 cm tolerance, and another at the rear bumper. The false positive at the rear bumper is a result of interference due to the identification of road texture as edges. Although modifying the edge detection threshold could reduce the number of road points identified as edges, no wheel details would then be identifiable as edge points either. For this image, the Template Matching algorithm detects the rear wheel of the vehicle but fails to detect the front wheel, for similar reasons as before.

(a)

(b)

(c)

(d)
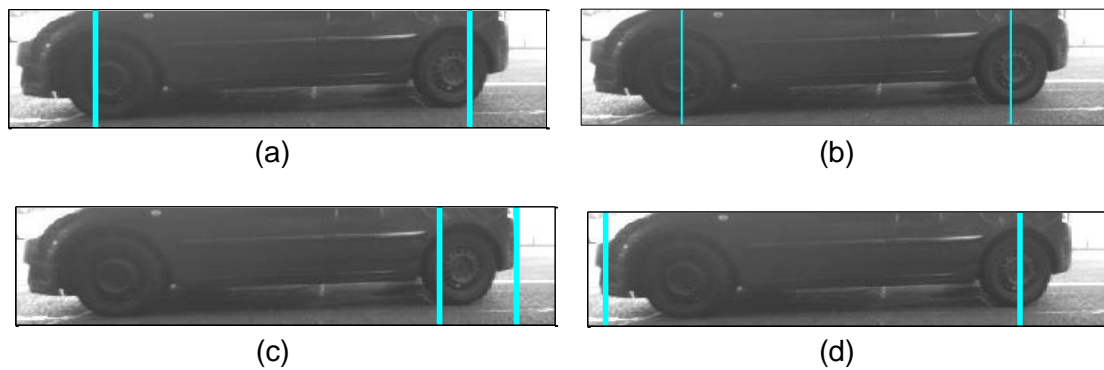
Figure 4-7. Example application of the four considered algorithms to a difficult image. (a) PWF based algorithm, (b) DPM algorithm, (c) Hough Transform and (d) Template Matching.

Table 4-1. Results of application to 80 images of cars.

Method	Criterion 1	Criterion 2	Criterion 3
	Wheels Detected	False Positives	Full Vehicles Identified
PWF-based algorithm	96.9%	11	90%
DPM method	97.5%	2	94%
Hough Transform	54.5%	164	23%
Template Matching	68.5%	31	49%

The results of the application of the four algorithms to the 80-image sequence are given in Table 4-1. It shows that the proposed algorithm and DPM provide the most accurate results with 96.9 and 97.5% of the wheels detected, respectively. The proposed algorithm significantly outperforms the Hough

Transform and Template Matching algorithms and provides a similar level of accuracy as DPM. It correctly locates about 97% of all wheels, but notably, 90% of vehicles have their wheel locations accurately determined, with no false positives present. This compares with 54.5% and 68.5%-wheel detection and 23% and 49% correctly analysed vehicles for the Hough Transform and Template matching respectively. It is also observed that PWF runs faster than DPM which is a more complicated algorithm and needs extra time for training. No training or validation is needed for the PWF-based algorithm which makes it more user-friendly. Because 90% of vehicles are analysed correctly, there is good indication that the proposed algorithm is an effective means of locating wheels in images of cars.

CHAPTER 5
BASIS FOR THE DESIGN OF NOTIONAL LOAD MODELS

5.1 Introduction

Bridges vary enormously in their structure (such as simply-supported, continuous, suspension, cable-stayed.) and relevant LEs (such as shear, bending, reactions). Therefore, the set of ILs across the bridge network of a region or country varies tremendously. Alongside this, the vehicle fleet that uses the bridges in the network also differ hugely. Commonly, the number of axles comprising vehicles ranges from 2 to 6, and the gross vehicle weight (GVW) varies from 2 to 100 t (ABS, 2017). Further, the vehicle configuration differs significantly due to varying axle loads and spacings. Currently, it is accepted that heavy vehicles govern short bridges, while the total vehicle load governs long bridges (Harman et al., 1984; Nowak, 1993; OBrien et al., 2012; OBrien et al., 2014; Caprani et al., 2016). However, in the face of the wide variation of both ILs and vehicles, there is no quantitative method to evaluate this understanding of the bridge traffic load phenomenon.

Compounding the difficulty of developing a standard, and the difficulty of identifying critical loading arrangements, the volume and composition of the traffic fleet is continuously evolving. According to the World Health Organization (2017), there was a 16% increase in the number of registered vehicles between 2010 and 2013. Furthermore, the loads that trucks are permitted to carry are also increasing. In Australia, this tendency is estimated to be 10% per decade (Heywood and Ellis, 1998; Heywood et al., 2000), and a similar situation exists in other countries (Cohen et al., 2003). This is to be expected given the economic benefits of increasing truck limits (McKinnon, 2005). A further consequence of changing legal limits is new vehicle configurations, such as tractor-trailer-trailer combinations. With the above changes in both magnitude and configuration of traffic loads taking place, NLMs ought to be continuously revised and updated to ensure bridge safety. However, NLMs in most standards are rarely updated, in part because there is no numerical approach to assist with updating the NLM configuration.

To facilitate the development and updating of NLMs in standards, we introduce quantitative metrics of both vehicle configuration and IL shapes. A peakedness metric is introduced to characterise IL shape. A generalised influence line

function (GILF) is introduced to represent any real IL, explicitly using peakedness as a parameter. A concentration metric is introduced to characterise the configuration of vehicle loading. The relationship between peakedness, concentration, and LE is established. This is done for the NLMs of existing standards for Australia, China, EU, UK, and the USA. Further, it is done for real traffic from both Australia and the EU. As a result, the quality of the NLM representations of real traffic can be quantitatively and rationally assessed. Finally, it is shown how by working backwards using a prescribed concentration and peakedness an NLM can be readily designed. Consequently, this chapter should facilitate the development of standards with improved NLMs that better target specific configurations of vehicle loading, or traffic loading more generally.

As NLMs are usually different, it can be understood that only one of NLMs is the most critical for a certain bridge. But the most critical NLM varies when bridge length changes. Take two bridges and two NLMs as an example. The ILs are triangle ILs with bottom length of 30 m and 100, but the heights are the same (1). The live load is from the load models of S1600 (Figure 2-1) and LM1 (Figure 2-3). Results are shown in Table 5-1.

Table 5-1. LEs for different bridge lengths and load models. Numbers outside the brackets are the results of NLMs with UDL parts. Numbers inside the brackets are the result of NLM without considering the UDL parts.

LE (kNm)	AU-S1600	EU-LM1
30 m bridge	827 (467)	981 (576)
100 m bridge	2010 (810)	1942 (592)

The Eurocode (LM1) governs the short bridge (30 m), and Australian NLM (S1600) governs the long bridge (100 m). The difference can be even more evident if UDL part of the load model is ignored. It is not rational to say which NLM is more accurate as they all virtual vehicles. However, it can be inferred that for different bridge length, the critical traffic loading is not always the same. It is necessary to study the load models for different circumstances.

This chapter provides new metrics that quantify the effect of the IL shape and the concentration of vehicle axle loads. The relationship is found to be complicated as there are many variables involved in the concentration of the loads. NLMs from many international codes are quantitatively evaluated against real traffic from Europe and Australia using these new metrics.

5.2 The Generalized Influence Line Function (GILF)

To study the entirety of potential IL lobe shapes, it is useful to introduce a general function that can represent an extensive range of lobe shapes. Such a function allows discrete ILs which are common in practice, to be represented on a continuum by fitting. Further, it is most useful if the parameters of this function can be directly linked to metrics of interest, such as peakedness. The GILF proposed here is a simplified function based on a wide range of IL functions given in Larnach (1964). The GILF is given by:

$$y = (a_1 r + a_2 r^2 + \cdots + a_n r^n)(r - 1) + bm \tag{18}$$

where r is the non-dimensional distance (x/L); x and y are the IL coordinate; L is the total length for the lobe; a_i ($i = 1, 2\ldots, n$) and b are shape parameters; and m is a piecewise function, given by:

$$m = \begin{cases} \dfrac{x}{s}, & x \leq s \\ \dfrac{x - L}{s - L}, & x > s \end{cases} \tag{19}$$

where s is the skewness parameter.

For convex IL lobes, $n = 2$ is found to be sufficient. On the other hand, for concave lobes, $b = 0$, and n is usually less than four but increases for higher static indeterminacy. Figure 5-1 shows several lobes generated using the GILF. The ILs are seen to be good representations of lobes of common ILs.
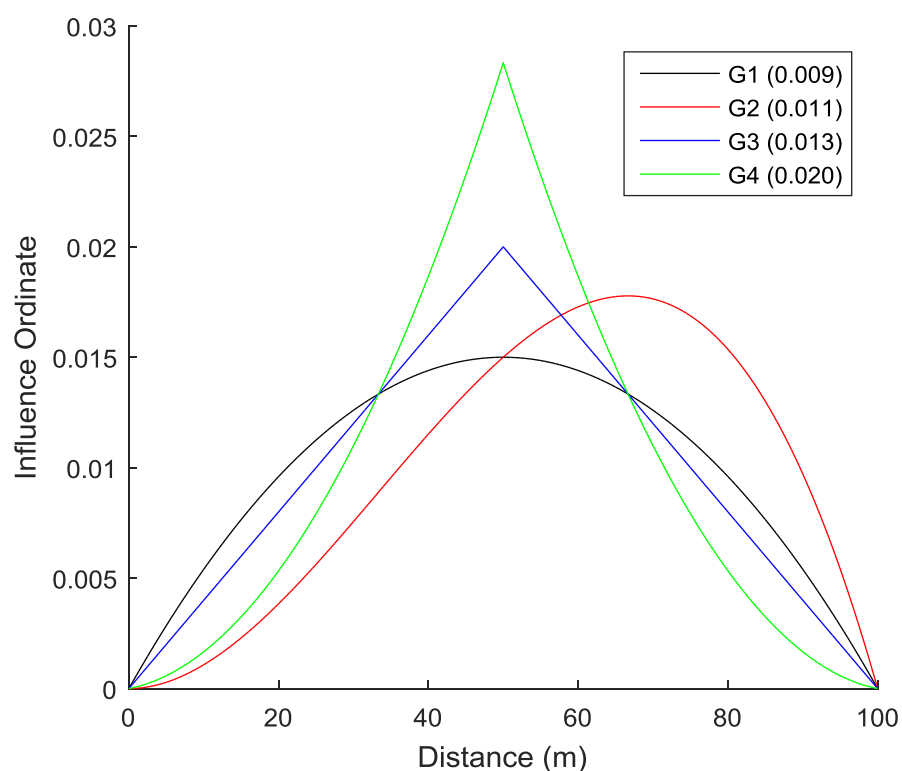
Figure 5-1. ILs generated by GILF. The parameters are shown in Table 5-2. The numbers in parentheses are the peakedness values (section 4.2) and are seen to reflect intuition.

Table 5-2. Parameters for the curves from GILF curve fitting

Curve No.	l	a_1	a_2	a_3	r	b
G1	100	0.06	0	0	0	0
G2	100	0	0.12	0	0	0
G3	100	0	0	0	0.5	0.02
G4	100	-0.1	0	0	0.5	0.0533
T1	100	0	0	0	0.5	1
T2	100	-4	0	0	0.5	2
T3	100	4	0	0	0	0
T4	100	0	0	0	0.5	2
T5	50	0	0	0	0.5	1
T6	50	0	0	0	0.5	2
GGB(b)	398.22	24895	-66	0	0.504	-19596
GGB(c)	446.59	16733	-11672	-4699	0	0

5.3 The IL Metric – Peakedness

An IL is the variation of a LE at a point as a unit load traverses the structure. A multi-span large bridge can have a long and complicated IL, and it can be divided into several sections based on where it crosses the zero LE line (*x*-axis). These IL sections are termed lobes. For different ILs, there are convex (or leptokurtic) lobes and concave (or platykurtic) lobes (see Figure 5-2). Consequently, the LE responses for different shapes of IL lobes vary significantly. However, although the terms tend to be understood, 'convex' and 'concave' are qualitative descriptions of the lobe shape. To investigate the relationship between IL and resulting LE (for a given vehicle), a quantitative metric for representing the shape of IL is needed. More specifically, a means to measure the 'peakedness' or concentration of the lobe about the maximum point, is required.
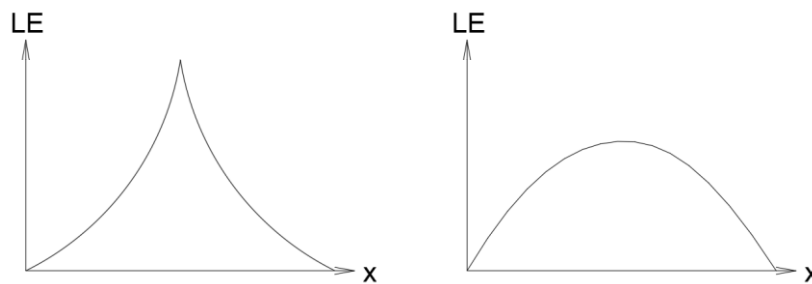
Figure 5-2. A typical convex IL lobe (left) and concave IL lobe (right).

Pearson (1905) defined the fourth standardised moment of a curve as kurtosis. He termed "leptokurtic", "mesokurtic" and "platykurtic" to show the degree of flat-toppedness. Since then, much research (Kitchenham et al., 2001) has used this metric to indicate the peakedness, especially in probability theory. However, recently some work has pointed out that this concept is flawed, and instead kurtosis represents tail extremity (Darlington, 1970; DeCarlo, 1997). Therefore, although appealing, kurtosis cannot be used to represent the peakedness of the ILs.

To measure the peakedness of IL lobes, a new peakedness metric, *p*, is introduced, defined by:

$$p = \frac{y_0 - h}{\sqrt{A}} \tag{20}$$

where, with regard to the lobe, A is the area underneath; y_0 is the maximum ordinate, and; h is the ordinate to the centroid of the lobe. Note that all variables are taken as absolute values. The parameters of this metric are illustrated in Figure 5-3. The peakedness metric is invariant with respect to with different lobe lengths and heights (Figure 5-4), or influence ordinate values. Higher peakedness indicates that the shape of the IL is more convex (or leptokurtic), and vice versa. For example, the peakedness for a rectangular lobe of unit height is $p = (1 - 0.5)/\sqrt{L} = 1/(2\sqrt{L})$, and for a triangular lobe of unit height, $p = (1 - 0.33)/\sqrt{0.5L} = \sqrt{8}/(3\sqrt{L})$.
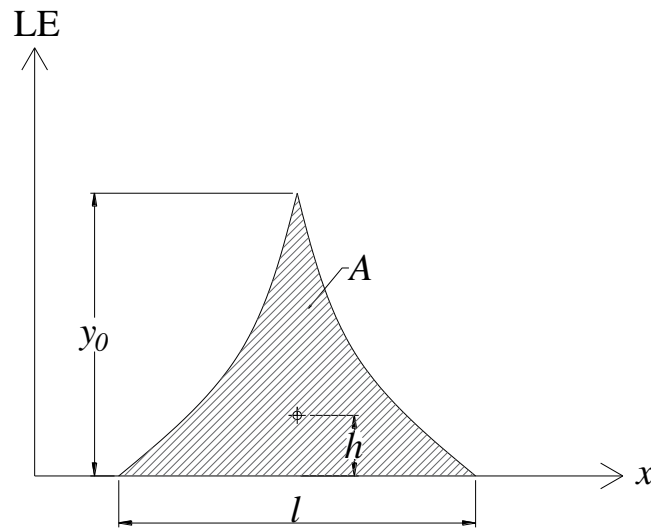
Figure 5-3. An illustration of the parameters in the peakedness algorithm.
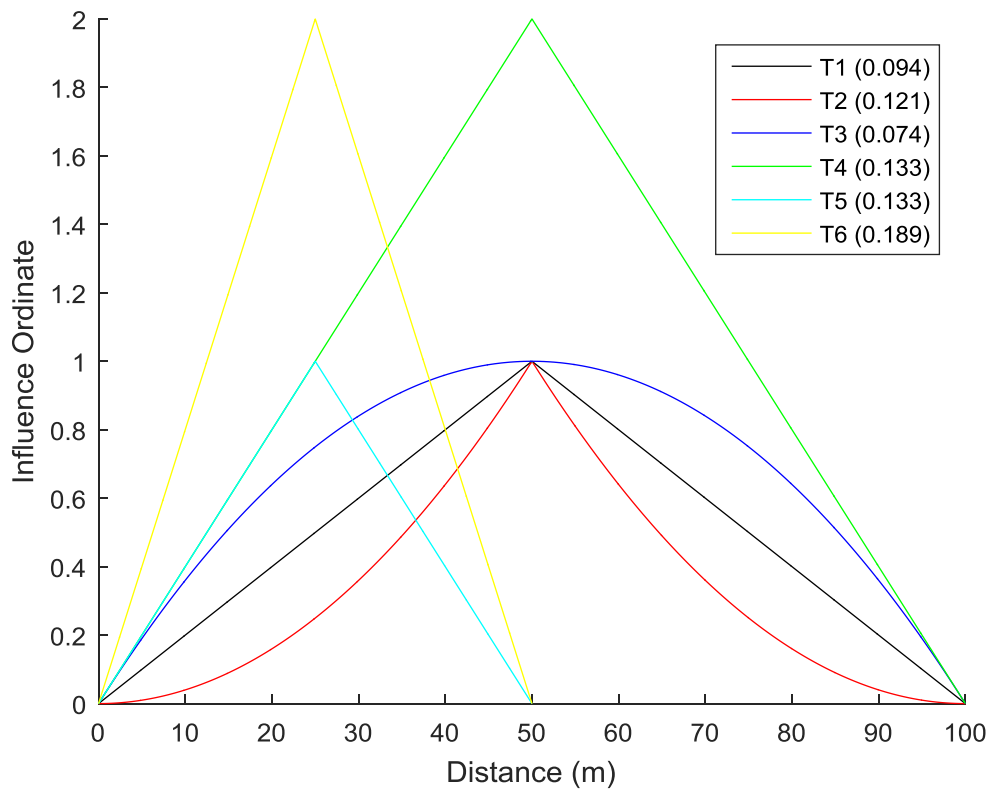
Figure 5-4. A peakedness test for ILs with various shapes and scales. The numbers in the bracket are the peakedness. The parameters are shown in Table 5-2.

The proposed peakedness metric is given in Figure 5-4 for the lobes generated using the GILF. Again, the results are consistent with intuition. The peakedness of real ILs can also be determined by curve fitting using the GILF. Figure 5-5 illustrates the latter method for an IL for the Golden Gate Bridge taken from Enright et al. (2013). Two lobes are fit: one convex and one concave. The GILF is seen to fit the IL data quite well. Notably, the fitting curve indicates the vertex in the convex case, which is not included in the actual IL data points. The calculated peakedness values are 6.11 and 2.02 respectively, which again reflect intuition about the curves.

(a)

(b)

(c)
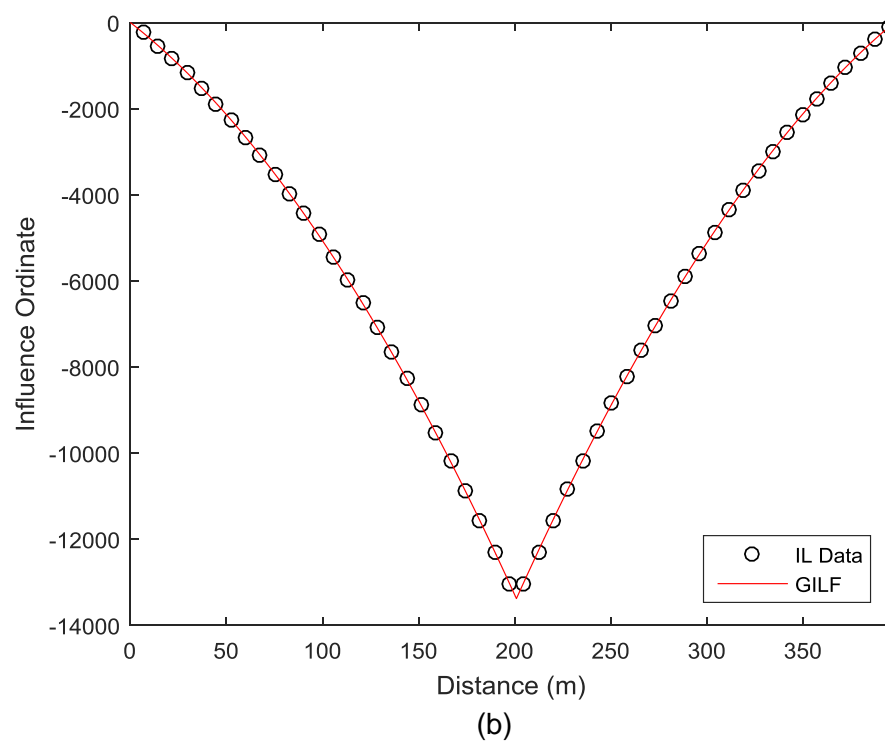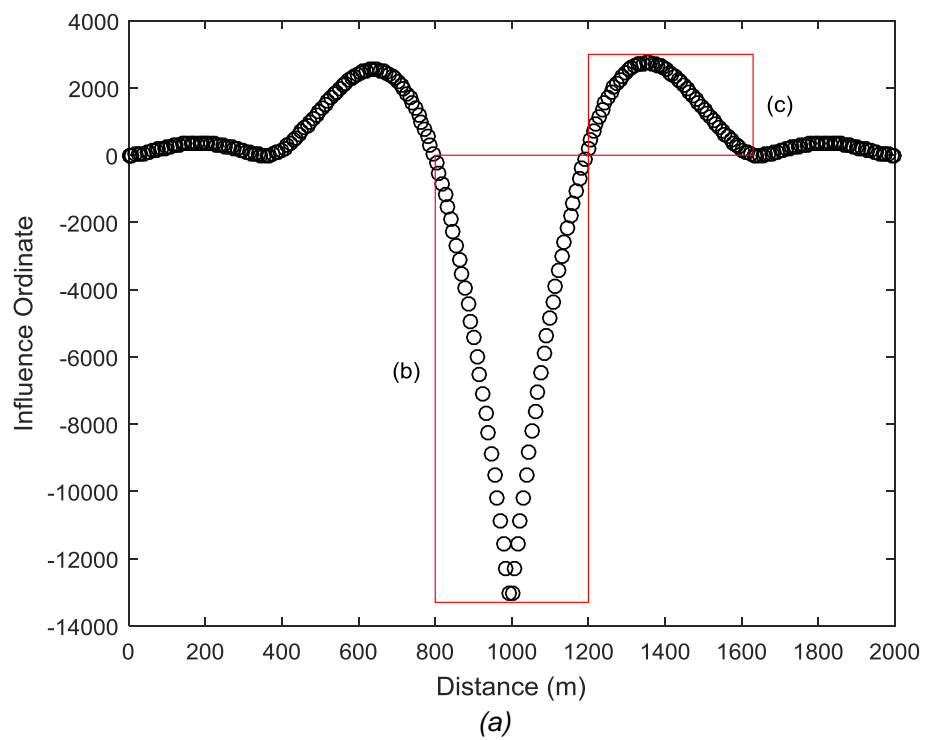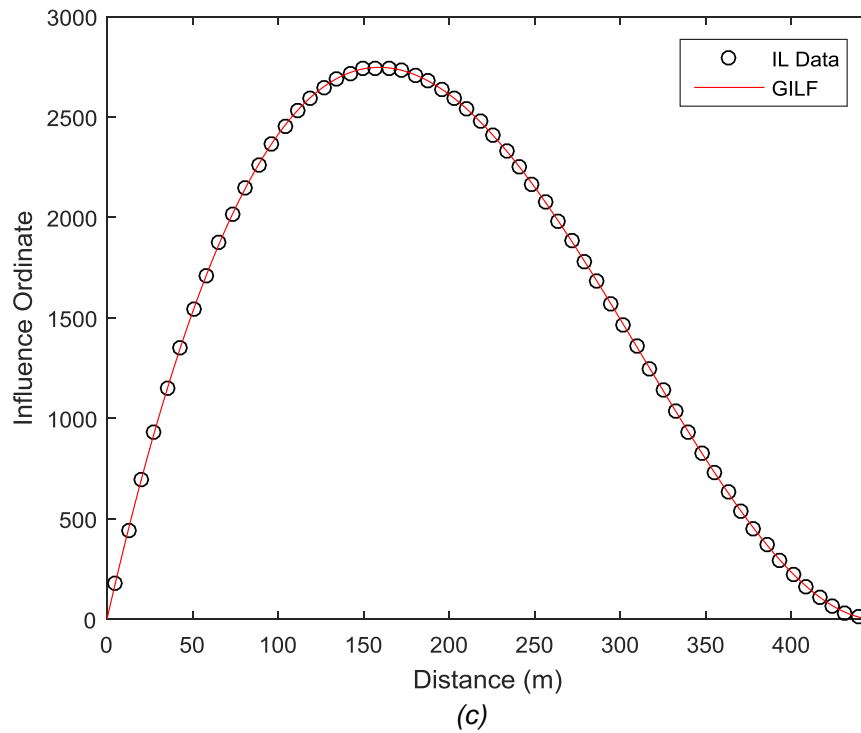
Figure 5-5. IL of mid-span girder bending moment for the Golden Gate Bridge (after Enright et al., 2013): (a) discrete points at 7.62 m spacing, determined from a finite element model; (b) Curve fitting a convex lobe (from 795.45 m to 1193.43 m) using the GILF, for which the peakedness is 6.11; (c) A concave lobe (from 1193.43 m to 1640.02 m) fitted by GILF, for which the peakedness is 2.02. Fitting parameters are shown in Table 5-2.

5.4 The Vehicle Metric – Concentration

For a given IL, the distribution of axle loads over the length of a vehicle apparently plays an essential role in the resulting LE. In developing a metric to capture this effect, it is vital to avoid invariance with respect to axle position – this is because the sequence of axle loads is critical to the LE. This requirement removes 'global' vehicle metrics from consideration, such as standard deviation of axle loads (invariant to axle position). Following presentation of the proposed metric, explanation of the rationale and meaning behind the various quantities is given.

To measure the concentration of load for a particular vehicle configuration, the concentration metric, c, is given by:

$$c = \frac{1}{n_e} \sum_{i=1}^{n} q_i \qquad \left[\frac{\text{Force}}{\text{Length}} \right] \tag{21}$$

in which, n_e is an equivalent number of axles for the n-axle vehicle and, q_i is the effective UDL for each axle. The equivalent number of axles, n_e, is given by:

$$n_e = n - \frac{1}{2} \cdot \max \left[n^2 D_a ; (n-1)^2 D_s \right] \tag{22}$$

where the mean absolute deviation (MAD) of axle loads, D_a, and the MAD of axle spacing, D_s, are given by:

$$D_a = \frac{1}{n} \sum_{i=1}^{n} \left| \omega_i - \bar{\omega} \right| \tag{23}$$

$$D_s = \frac{1}{n-1} \sum_{i=1}^{n-1} \left| \xi_i - \bar{\xi} \right| \tag{24}$$

in which $0 \leq \omega = w_i / W \leq 1$ is the relative weight of an axle, and $0 \leq \xi = s_i / S \leq 1$ is the relative spacing for axle i, given GVW is W and the vehicle length is S. Overbars represent mean quantities.

Running from $i = 1, \mathrm{K}, n-1$, the effective UDL for the i-th axle is given by:

$$q_i = \min \left[\frac{w_i^H}{\Delta \bar{x}^H + 1} \right], \quad H \in \{L, R\} \tag{25}$$

in which H is the left (L) or right (R) hand side outermost axle and $\Delta\bar{x}^H$ is the shift that occurs in the position of the vehicle's resultant weight should the considered axle be removed. Depending on which axle (L or R) gives the minimum, that axle is removed, and the effective UDL calculated again for the remaining vehicle configuration. This procedure continues until there is just one axle left, for which the effective UDL is calculated by taking a unit length: $q_n = w_n/1 = w_n$. The general calculation procedure is illustrated in Figure 5-6 and followed by an example.
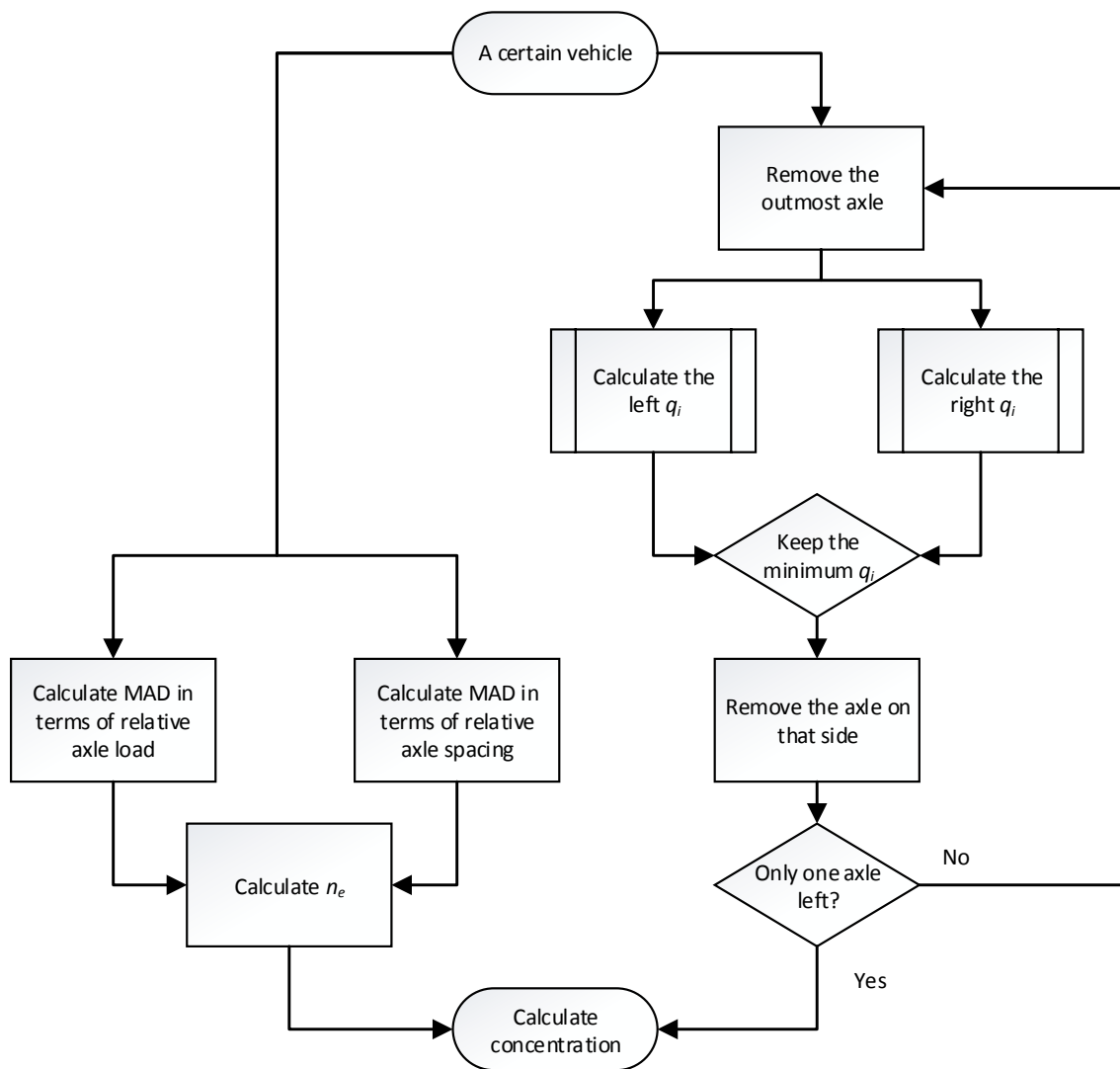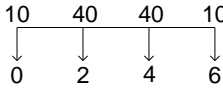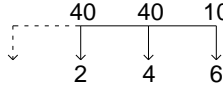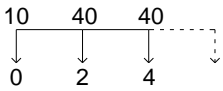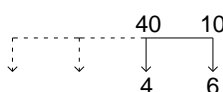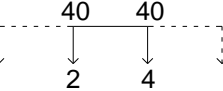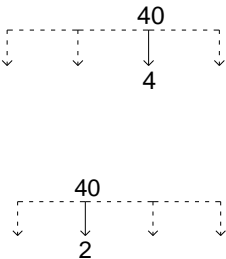
Figure 5-6. A flowchart of the concentration calculation procedure.

5.4.1 Example Calculation

An example of concentration calculation for a four-axle vehicle with 100 total weight is given in Table 5-3.

Table 5-3. An example of concentration calculation for a four-axle vehicle.

10 40 40 10 0 2 4 6	Step1: Calculate the equivalent number of axles: $$D_a = \frac{2\,\lvert 0.1-0.25\rvert + 2\,\lvert 0.4-0.25\rvert}{4} = 0.15$$ $$D_s = \frac{3\,\lvert 0.333-0.333\rvert}{3} = 0$$ $$n_e = 4 - 0.5\ \max(4^2 \cdot 0.15,\, 3^2 \cdot 0) = 2.8$$
  40 40 10 2 4 6 10 40 40 0 2 4 40 10 4 6 40 40 2 4	Step2: Remove the outmost axle round by round until only one axle left. Calculate the effective UDL at each round. $$x_0 = \frac{10 \cdot 0 + 40 \cdot 2 + 40 \cdot 4 + 10 \cdot 6}{100} = 3$$ Assume to remove the left axle at round 1: $$x_1^L = \frac{40 \cdot 2 + 40 \cdot 4 + 10 \cdot 6}{90} = 3.333$$ $$q_1^R = \frac{10}{\lvert 3.333 - 3\rvert + 1} = 7.5$$ Assume to remove the right axle at round 1: $$x_1^L = \frac{10 \cdot 0 + 40 \cdot 2 + 40 \cdot 4}{90} = 2.667$$ $$q_1^R = \frac{10}{\lvert 2.667 - 3\rvert + 1} = 7.5$$ $$q_1 = \min(7.5, 7.5) = 7.5$$ Therefore, the left axle is removed. Assume to remove the left axle at round 2: $$x_2^L = \frac{40 \cdot 4 + 10 \cdot 6}{50} = 4.4$$ $$q_2^L = \frac{40}{\lvert 4.4 - 3.333\rvert + 1} = 19.355$$ Assume to remove the right axle at round 2: $$x_2^R = \frac{40 \cdot 2 + 40 \cdot 4}{80} = 3$$ $$q_2^R = \frac{10}{\lvert 3 - 3.333\rvert + 1} = 7.5$$ $$q_2 == 7.5$$ Therefore, the right axle is removed.

  	Assume to remove the left axle at round 3: $$q_3^L = \frac{40}{|4 - 3| + 1} = 20$$ Assume to remove the right axle at round 3: $$q_3^R = \frac{40}{|2 - 3| + 1} = 20$$ $$q_3 = \min(20, 20) = 20$$ Therefore, the left axle is removed, and only one axle is left.
	Calculate the concentration with previous results. $$c = (7.5 + 7.5 + 20 + 40)/2.8 = 26.786 \approx 27$$

Note:

- Steps 1 and 2 can be switched.
- For q_i, if the left and right values are the same in the same round, any of them is okay to be removed. The example removes the left one as a default.

5.4.2 Essence of the Concentration Metric

In essence, the concentration metric is a mean effective UDL for an axle in the vehicle, with unit force/length. It is determined by finding the effective UDL for each axle in turn and dividing by an equivalent number of axles. Concentration itself is a multiple of GVW since the effective UDLs are multiples of GVW (equation (8)). The term q_i is the effective UDL contributed by the axle; the +1 in the denominator is to ensure that for very small axle spacings, the term does not become infinite. By selecting the axle for removal that contributes the minimum effective UDL, the more significant loads are retained for the next iteration. The expression for the equivalent number of axles arises by correcting the true number of axles for small axle weights or spacings. For example, a 3-axle vehicle may only have 2.4 effective axles because the last two axles are close, and the first axle is relatively light. The equivalent number of axles is found by considering the relative MADs of the actual vehicle axle weights and spacings to those for a hypothetical case in which all the vehicle weight is concentrated on just one outside axle. Concentration could be made dimensionless by normalising by the vehicle length-to-weight ratio. However, this would mean that short evenly-loaded vehicles would return the same metric as longer heavier but still even-

loaded vehicles. Consequently, the metric is dimensioned in consistency with the force and length units used in the IL and resulting LE also.

5.4.3 Concentration for Simulated Vehicles

To illustrate the performance of the proposed metric, Figure 5-7 shows the concentration calculated for different vehicle lengths, load distribution, load sequence and axle numbers. It is assumed that the total weight of all vehicles is the same, equal to 100 units. In general, the concentration algorithm identifies different types of vehicle with intuitive relative measures of concentration. Its mean effective axle weight measure corresponds with the limiting cases of a point load (V1) and a UDL (V9), distinguishing between intermediate cases.
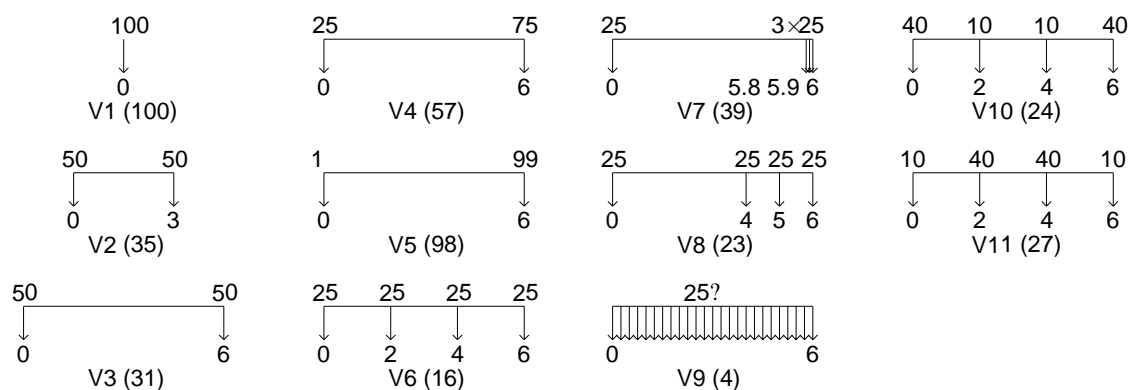
Figure 5-7. Configuration and calculated concentration for hypothetical non-dimensional vehicles. (The axle weight is shown above each axle, and the distance to each axle from the left-hand side is shown below.)

5.4.4 Concentration for NLMs

The concentration metric is next applied to several NLMs, including the Australian load model M1600 and S1600, American load model HL93, European load model LM1, Chinese load model and traditional British load model HA. Note UDL parts are not considered for all NLMs because we are only concerned about how the load model represents vehicles. The results are shown in Figure 5-8; the Chinese load model is the most concentrated, due to its single heavy axle configuration; the Australian load model S1600 has the lowest concertation. This is intuitive, as it has a long vehicle length with 12 relatively light axle loads.

Figure 5-8. Configuration and concentration [kN/m] for load models. Note that relative concentration can be examined by dividing concentration by total weight of the load model.

5.4.5 Concentration for Traffic Data

The concertation metric is next applied to Australian and French truck traffic data obtained from WIM. The Australian data is taken from a site at the West Gate Bridge (Foong and Caprani, 2016), and the French data is from the Auxerre site used to calibrate the Eurocode (Bruls et al., 1996a). The histograms of truck concentrations for the two sites are shown in Figure 5-9. Clearly, the vehicle configurations are entirely different between two locations. Australian vehicles are less concentrated than the French vehicles. The French truck fleet has a broader spread of concentrations, approximately in the range 60-80 [kN/m]. In contrast, the Australian concentrations are mostly confined to the range 20-30 [kN/m]. Based on this, for a given IL shape, Australian and French truck fleets would impart different LEs (even neglecting differences in vehicle weights).

Figure 5-9. Concentration [kN/m] frequency in Australia and France.

The relationship between the concentration metric and vehicle weight, for a given number of axles, is shown in Figure 5-10 for the Australian and French truck data. Also shown are various NLMs. There is a strong linear trend between GVW and the concentration metric for each vehicle type (as defined by number of axles), with decreasing slope with increasing number of axles. Interestingly this phenomenon also exists for the NLMs: the single axle load models of UK and CN are in the top left, while the 12-axle AU load models are in the bottom right. The Eurocode and American load models are also located on the supposed trendlines; for which the US one fits quite well for both sets of traffic data. Further, it is clear that the AU load models have much higher total weight compared to the real vehicles, while other load models are closer. Regarding the representation of real vehicle concentrations, unsurprisingly the single-axle CN and UK load models do not represent real vehicle configurations well; nor does the two-axle Eurocode. According to this metric, the most representative load model of real vehicles is the US load model, both regarding weight and configuration. Nevertheless, NLMs are not intended to replicate real vehicles, but

rather the LEs that result from extreme combinations of real vehicles traversing bridges. Consequently, it is not appropriate to evaluate NLMs solely on concentration, but rather the interaction of both concentration (representing vehicles) and peakedness (representing ILs).

For helping designing load model, it is expected that the new load model should correspond to the local traffic. Take Australian traffic as an example, the new load model should be located on these trendlines, and the total weight is no less than 900 kN with concentration no higher than 120. For European traffic, the new load model should be located on these trendlines as well, but the total weight is no less than 700 kN with concentration no higher than 150. If possible, a larger dataset is recommended.
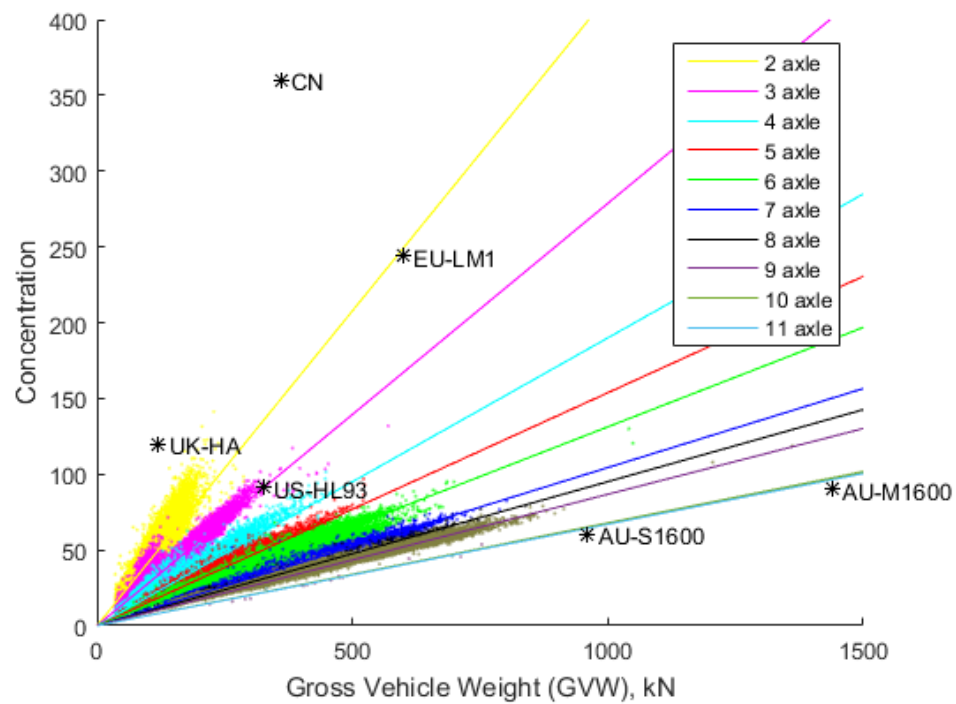
(a) Australian data
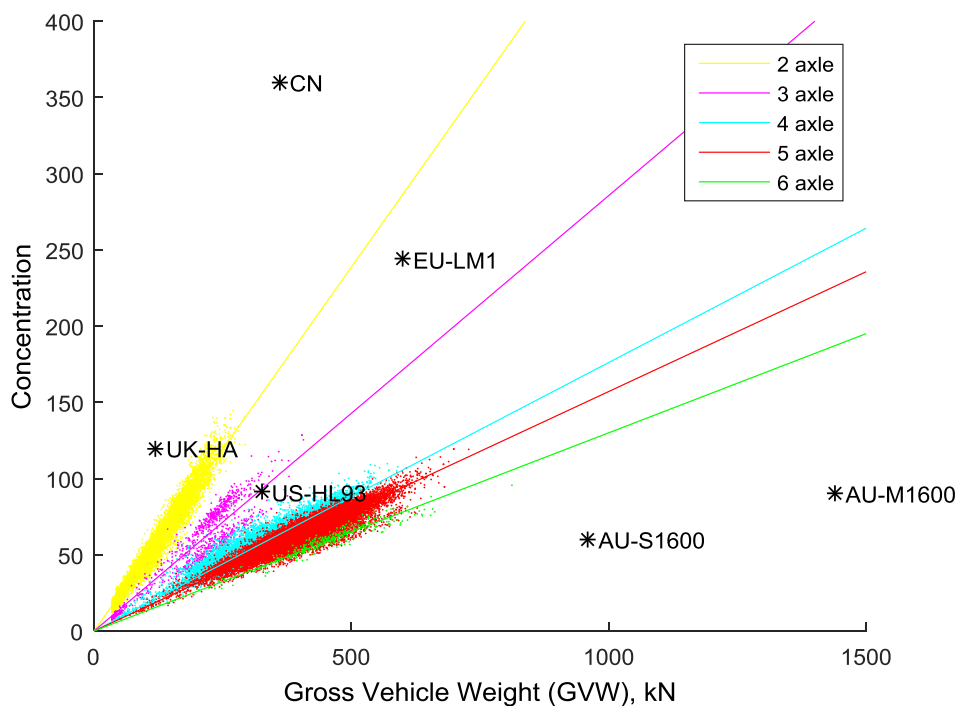
(b) French data

Figure 5-10. Relationship between GVW and concentration metric, showing trendlines for each vehicle type (by number of axles), and various NLMs.

5.5 Interaction between Peakedness and Concentration

The previous sections discuss the metrics peakedness and concentration separately. However, the primary purpose for them is to analyse how these two metrics combine to govern the LE. There are several tests conducted for quantitative measurement. As the peakedness represents the shape of the ILs, the test ILs are set to have same lengths (50 m) and same heights (1), ensuring the only variable is the shape (Figure 5-11). Concentration represents the load distribution of the vehicles. Therefore, the test vehicles have same total weight (100 kN) and same total length (10 m). However, there are many variables, other than previous two, involve in vehicles. In this paper, two variables are analysed in test 1 and test 2, respectively.
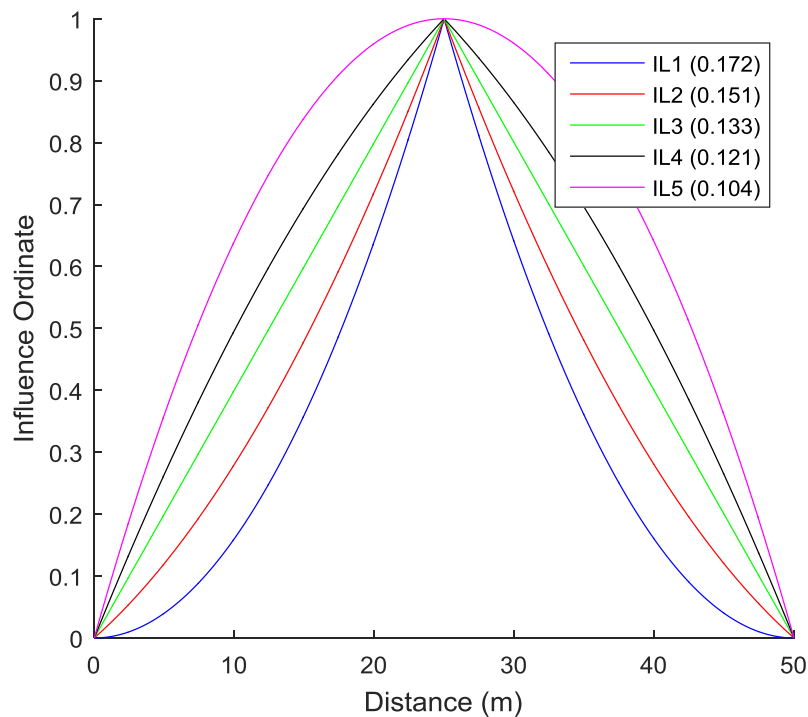
Figure 5-11. Test ILs. The numbers in the bracket are the peakedness.

Test 1 and Test 2 each change one single parameter of a standard vehicle (Figure 5-12). To analyse the impact of the axle loading bias, the loading in the middle axle varies in Test 1. The ratio of the middle axle load to other axle loads ranges from 1 to 64. Test 2 is to analyse the impact of the axle numbers. The axle number range increases from 5 to 64. Note these increase and changes are discrete in the tests.

```
    20    20    20    20    20
    |     |     |     |     |
    ↓     ↓     ↓     ↓     ↓
    0     1     2     3     4
```
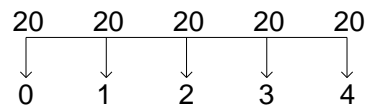
Figure 5-12. A standard vehicle for the Test 1 and 2.

The summarised result is shown in Figure 5-13. Assorted colours represent the LE from different ILs. It is evident that the less peak ILs are less sensitive to the variation of vehicle configurations and higher peakedness leads to lower LEs. This is reasonable as ILs with higher peakedness have lower ordinates.

As for concentration, it was believed that more separated loadings (or lower concentration) leads to lower LE. However, this result indicates it does not. The reduction of the LE depends on what is the reason behind for that concentration. The lower concentration from axle load bias can dramatically reduce the LE but, on the contrary, the lower concentration due to the axle number increases it. Though the impact of the load bias is much more severe, the relationship between the concentration and LE is not positive as previously expected. In the tests, the highest LE is from the single axle load case. The lowest is from the 2-axle load with no bias on loadings.

Vehicle configuration is complicated. The axle number and axle loads can have an impact on the LE. The axle load sequence can also impact the LE, especially when vehicle axle number is higher. There is no single rule which can illustrate the trend for different concentration vehicles.
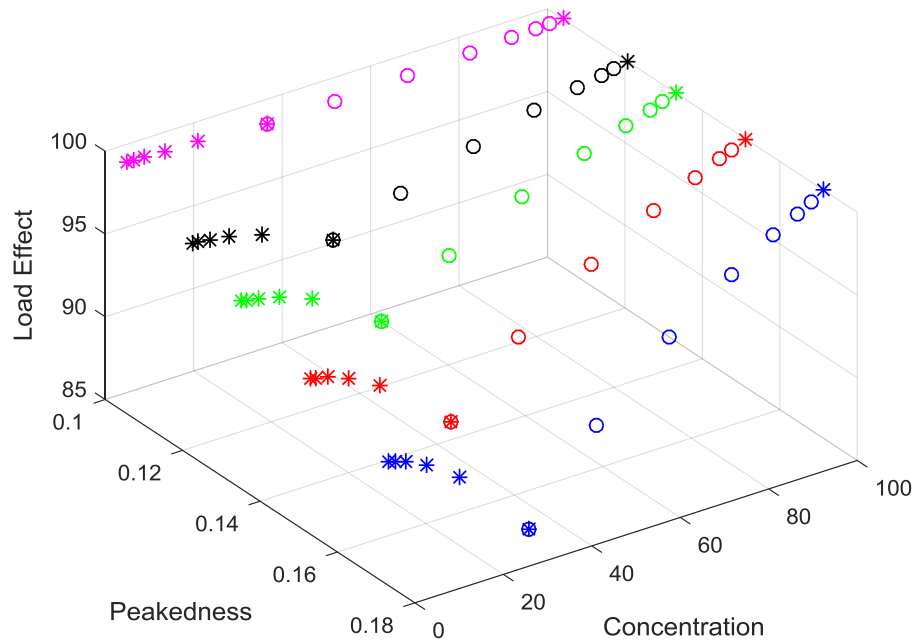
Figure 5-13. LE of varies ILs with different vehicles (cycles indicate the result from Test 1, Stars indicates the result from Test 2).

For actual vehicles, the relationship is slightly different. Actual vehicles tend to have more axle numbers when vehicle length gets longer. Meanwhile, the total weight increases but the axle loads decrease. An illustration is shown in Figure 5-14. It also illustrates that even the total load increases, the concentration decrease. Those vehicles are applied to the previous ILs, and the result is shown in

(c)

Figure 5-15. It verifies the previous research conclusion (Burgoyne, 1987). There is a peak in the LE result, and this peak is not located at the most concentrated end or the least concentrated end. Besides, for different peakedness ILs, the peak location is different. The critical case for low peakedness (concave) ILs is when the vehicle is less concentrated. The counterpart in the high peakedness (convex) ILs is when the vehicle is more concentrated. If to compare between ILs, no matter what vehicle concentration is, the low peakedness IL always governs. For the new load model design, it is recommended to consider the IL shape at first. Then the sensitivity range for vehicles are determined.
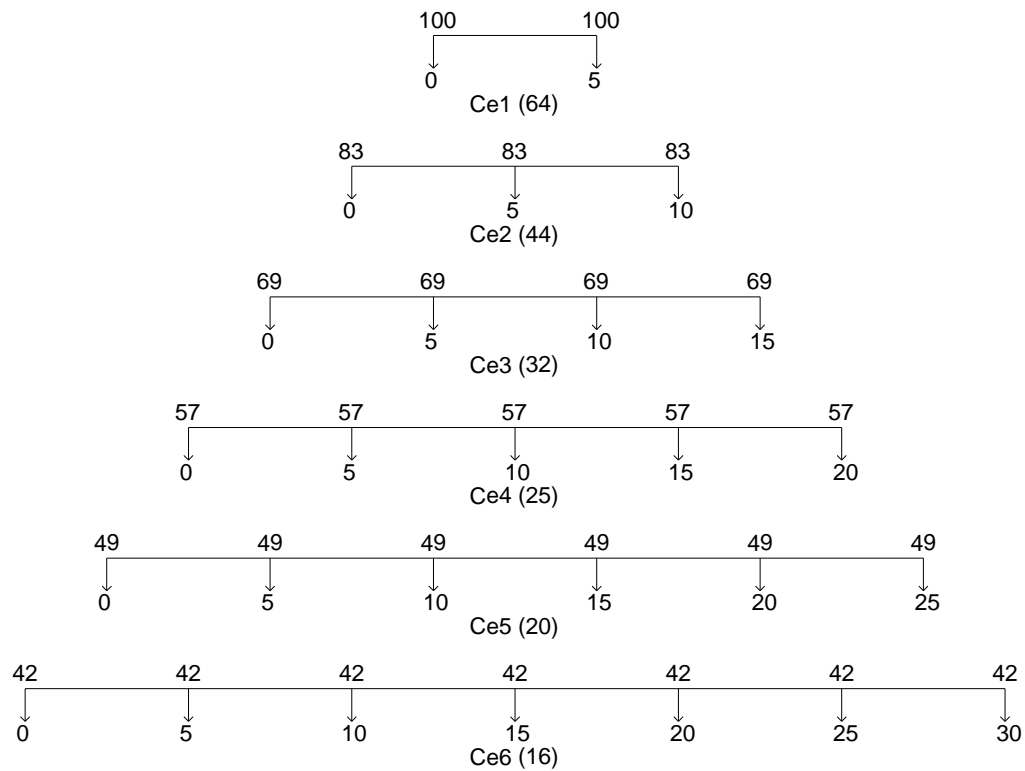
Figure 5-14. Examples of the reasonable cases. Ce is the concentration of each real example.

(a)
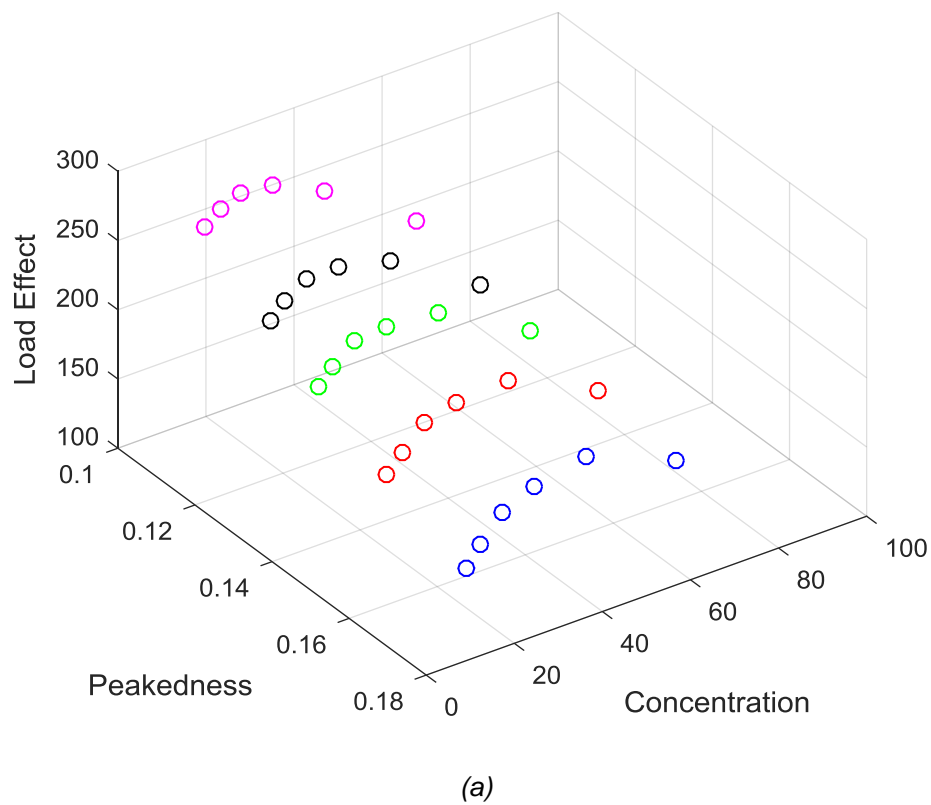
Figure 5-15. LE result for reasonable cases. (a) is a 3D view plot. (b) and (c) are 2D plot compressed from two different directions in (a). In the plot, assorted colours represent different ILs.

5.6 Load Models Application

Major load models with the test ILs are tested to see how different the load models are. The IL bottom length varies from 20 m to 220 m with 50 m steps, and the height is kept the same. The shape of the IL is the variable rather than the bridge length. Others are the same as Figure 5-11 shows, and the results are shown in Figure 5-16. The LE in the figure is the ratio of the original LE value with the maximum LE value among all cases. UDL parts in load models are not considered.

(a)

(b)

(c)
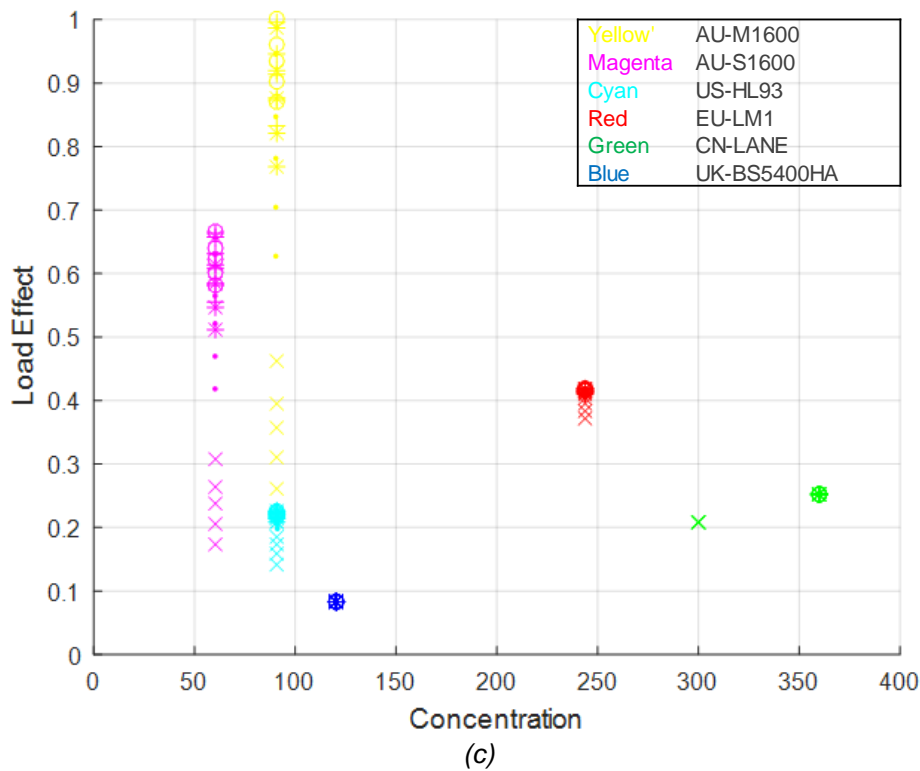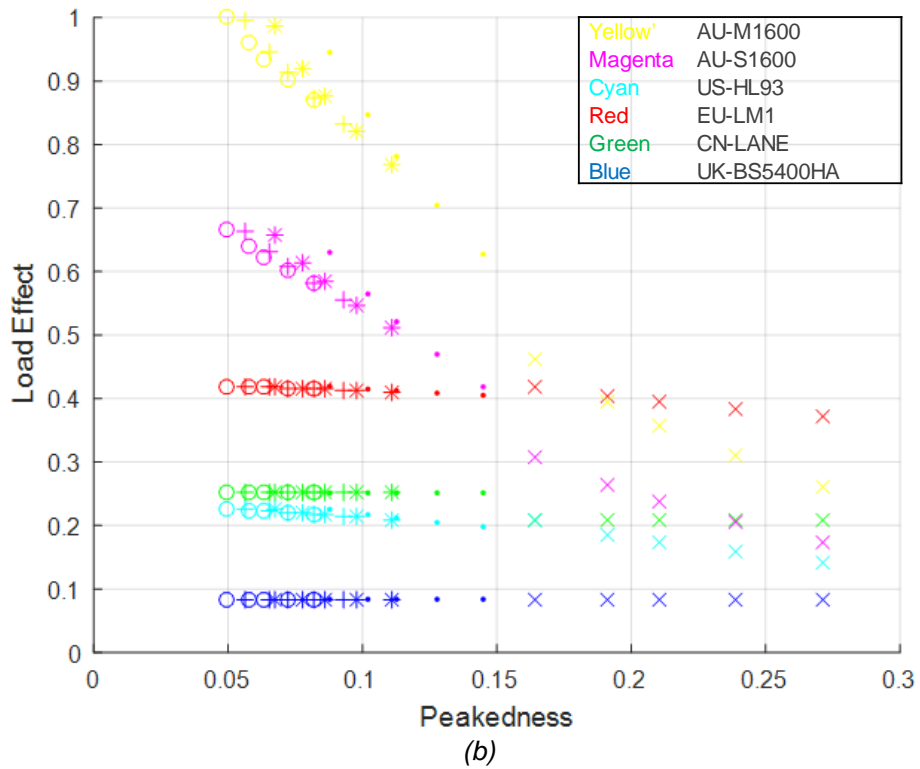
Figure 5-16. The LE from varies load models with different ILs. (a) is a 3D view plot. (b) and (c) are 2D plot compressed from two different directions in (a). In the plot, assorted colours represent different load models, and different marker type represents the different bridge length.

From Figure 5-16b, it can be referred that the Australian M1600 load model is the most conservative load model among all the tested load models, especially in the low peakedness ranges. European load models tend to govern the cases when it comes to the high peakedness ranges. On the contrary, UK-HA loading always is the lowest case regarding the LE, no matter what peakedness is. Moshiri and Montufar (2013) made a comparison of international bridge formulas. Though the view is from the allowable vehicle weights on the bridge, it also reflects that the Australian limit is the highest, compared with others, and US limit is the lowest. Figure 5-16c is a more random-like image. EU and CN have much higher concentrations while the rest is lower. There is no simple relationship between the concentration and LE.

Actual vehicles are imported into the image to show whether the load model can represent the actual vehicles. 50 vehicles are randomly selected from the Australian and European dataset, and they are plotted in Figure 5-17 and Figure 5-18, respectively.

(a)

(b)

(c)

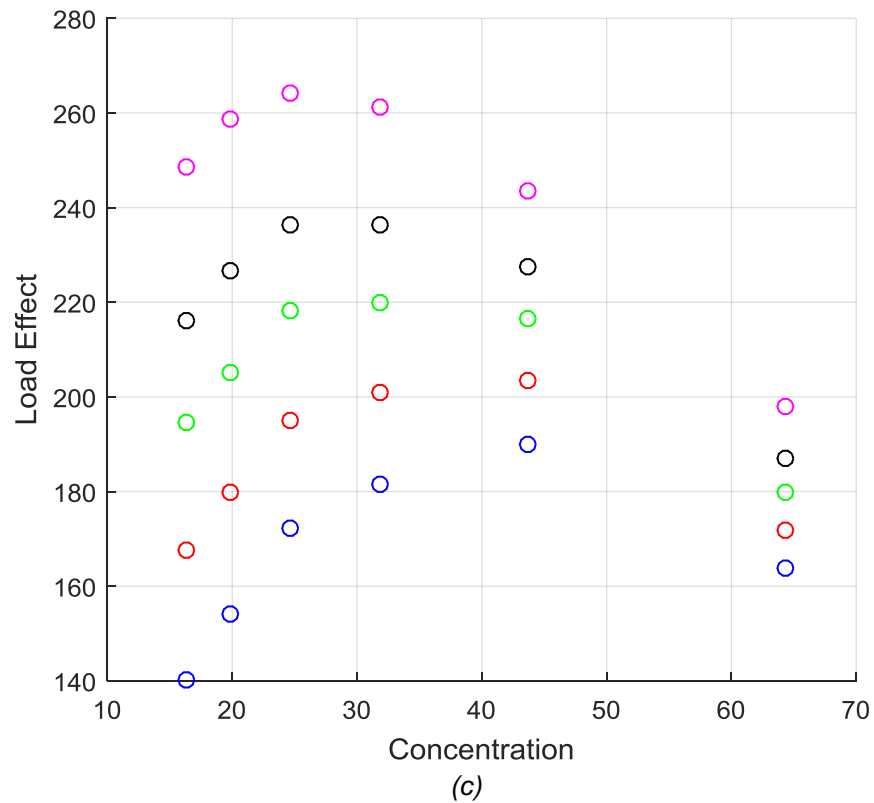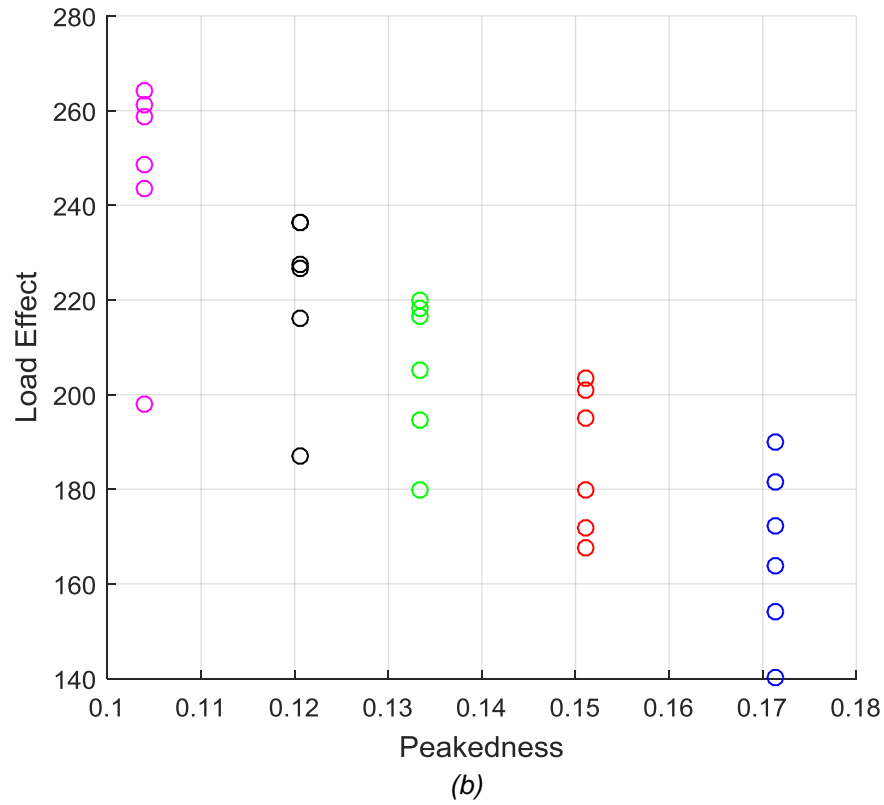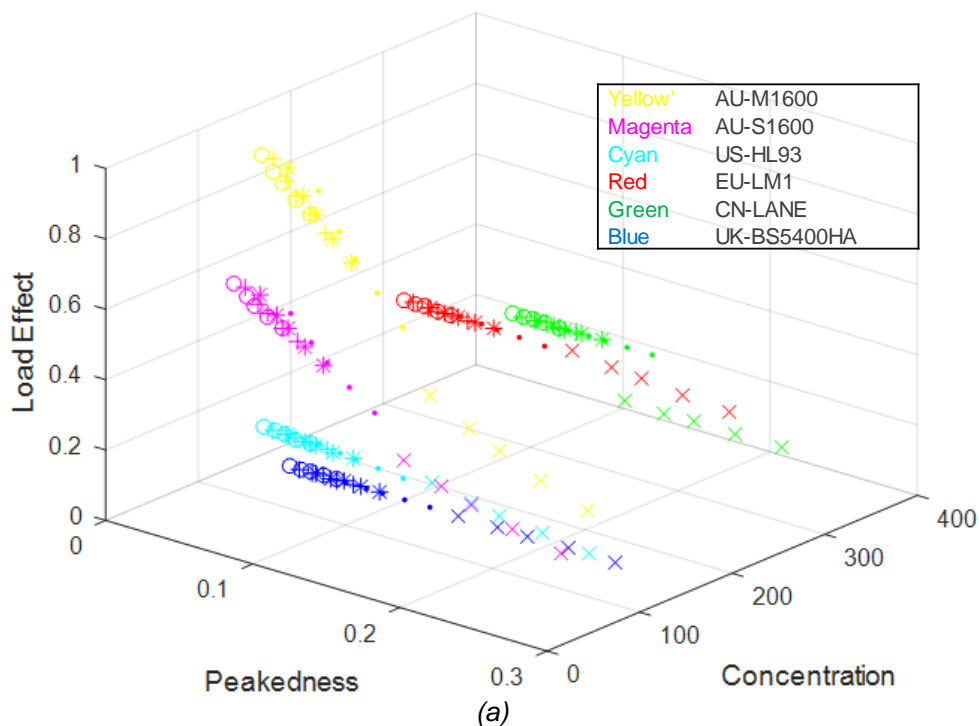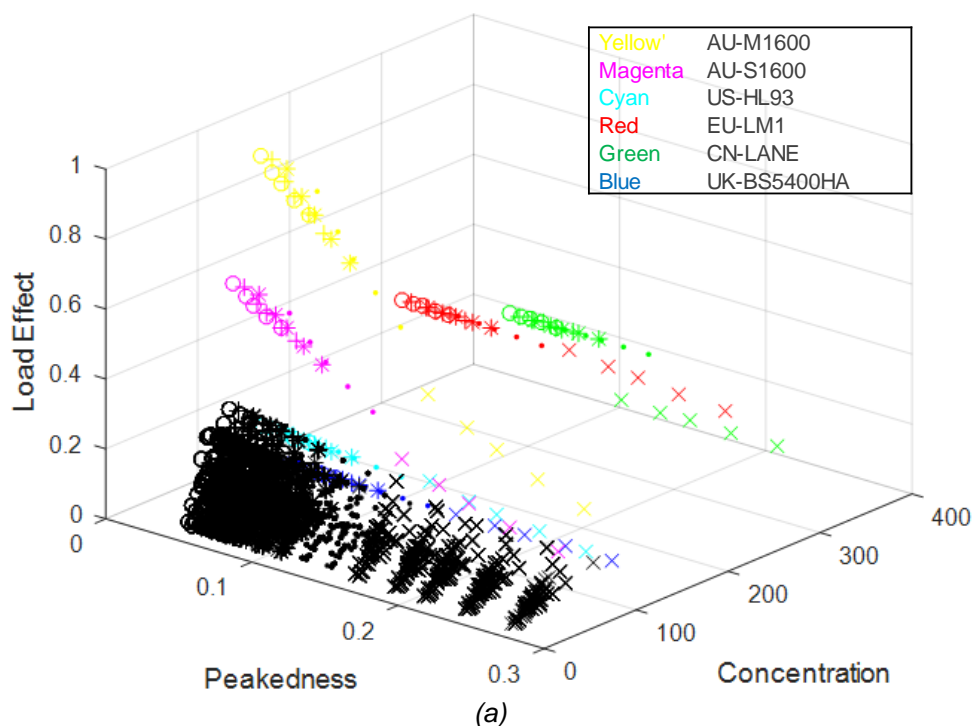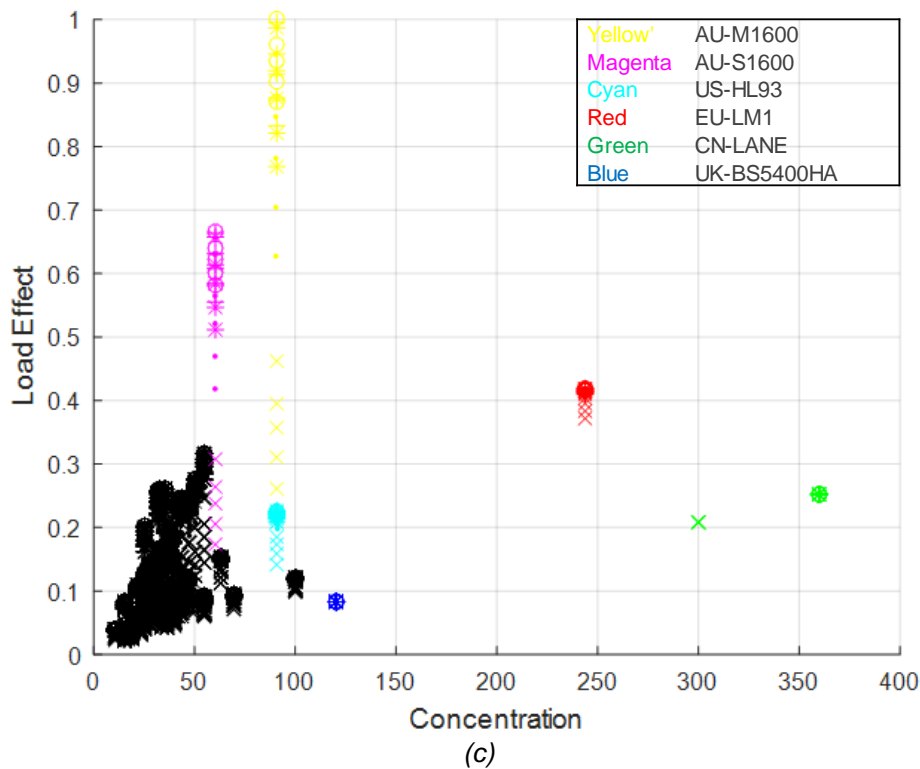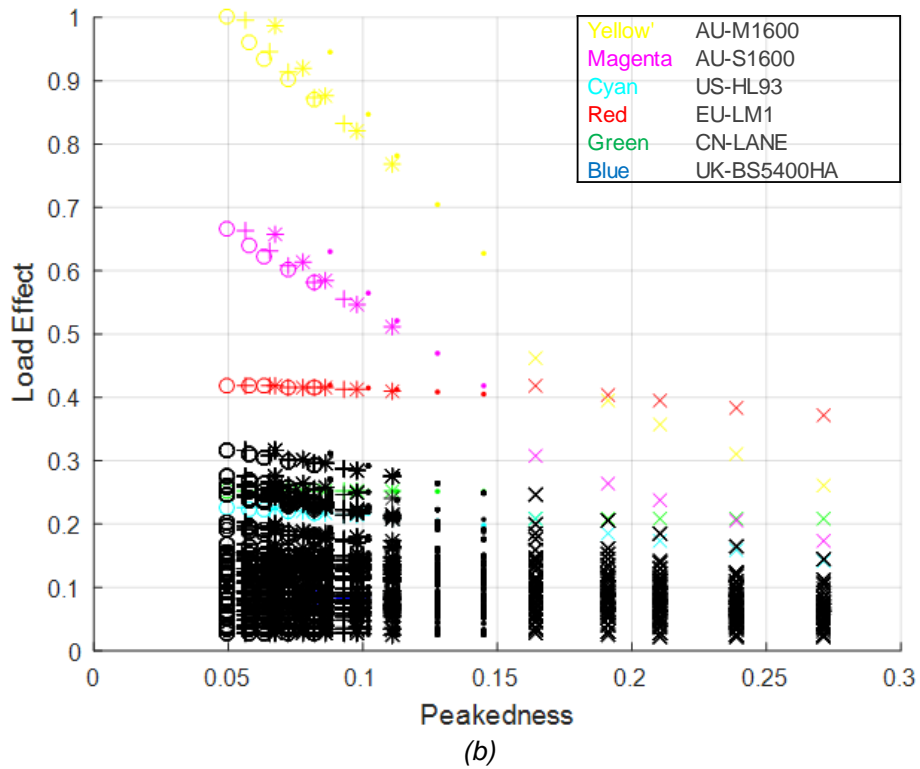*Figure 5-17. The LE from varies load models and actual vehicles from Australia dataset. (a) is a 3D view plot. (b) and (c) are 2D plot compressed from two different directions in (a). In the plot, assorted colours represent different load models, and different marker type represents the different bridge length.*

(a)

(b)

Yellow	AU-M1600
Magenta	AU-S1600
Cyan	US-HL93
Red	EU-LM1
Green	CN-Lane
Blue	UK-BS5400HA

(c)
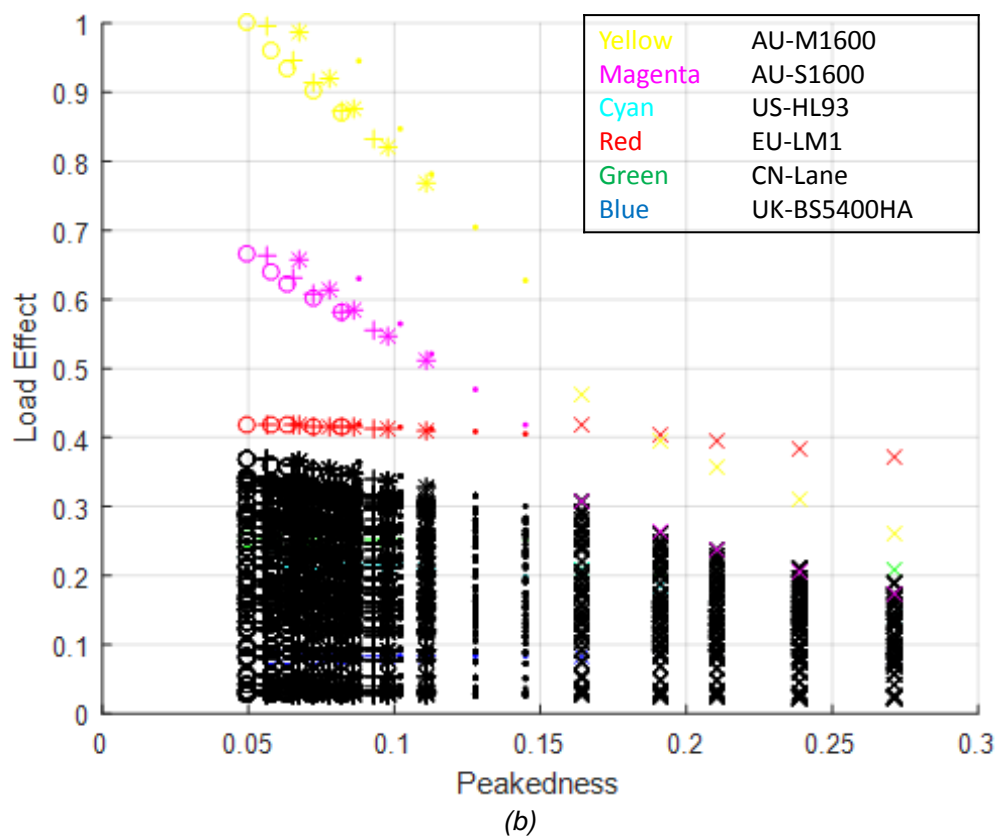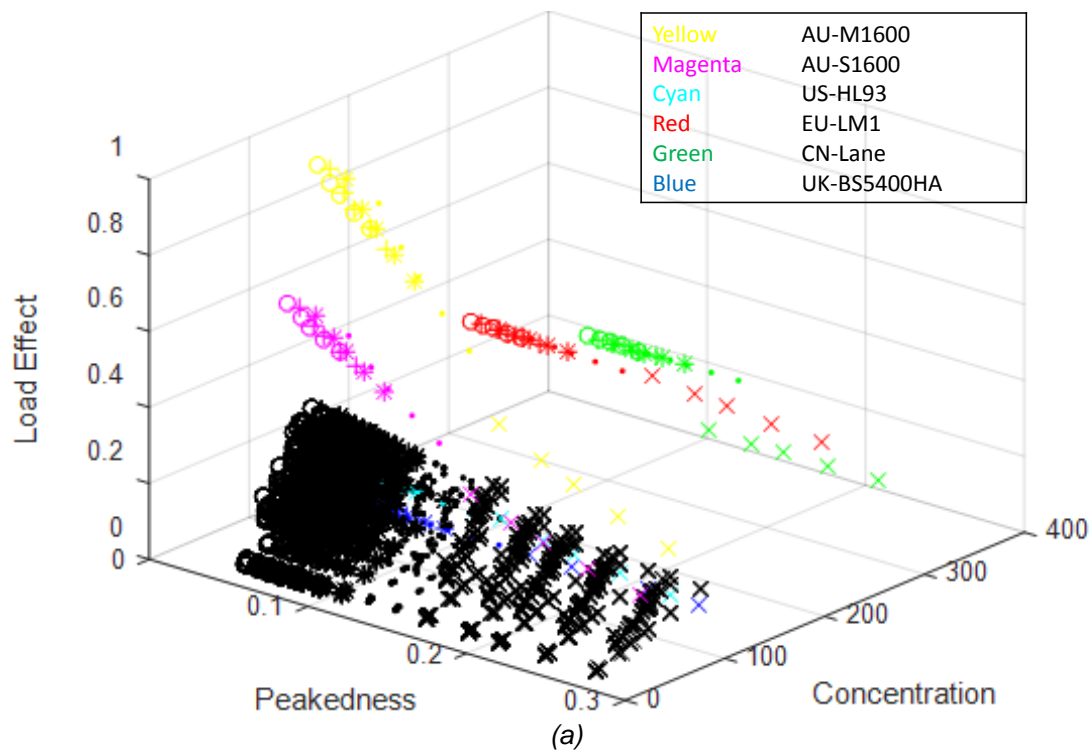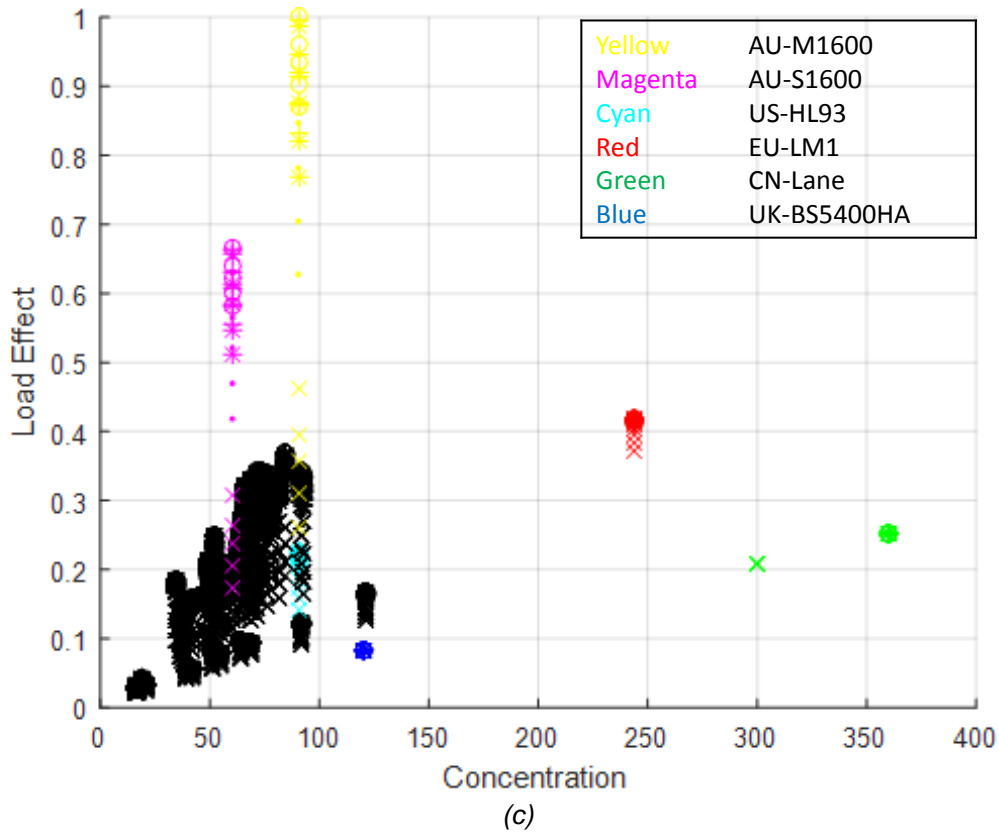
Figure 5-18. The LE from varies load models and actual vehicles from European dataset. (a) is a 3D view plot. (b) and (c) are 2D plot compressed from two different directions in (a). In the plot, assorted colours represent different load models, and different marker type represents the different bridge length.

With no doubt, the LE from actual vehicles in Australia and Europe are less than their standard load models. However, there are still some differences. SM1600 converges to the actual vehicles when peakedness is getting higher while LM1 diverges. SM1600 represents the actual vehicles better as the concentration value is much closer to the actual vehicles, compared to LM1.

To design the next-generation load model, the traffic data and bridge data are to be examined. For example, based on the European data mentioned above and a triangle IL, we suggest using a short vehicle as the prototype because short vehicles are more sensitive to the peak ILs. The candidate load model could be a 4-axle load model with a 15-metre length and its GVW is around 500 kN, based on the relationship between GVW and concentration. Though the LE analysis is still needed but it can accelerate the design process at the very beginning.

CHAPTER 6
IMPROVED LOAD PATTERNING FOR LONG SPAN BRIDGES

6.1 Introduction

This chapter examines design standards' approach to load patterning. Traffic microsimulation is adopted to simulate the traffic flows on a generic 1200 m bridge. We consider the possible road topologies that might give rise to design standard loading patterns. The LEs results are extrapolated to 5, 75 and 1000-year return periods, representing typical assessment and design return periods respectively. A proposed load patterning considers the free flow traffic as supplementary on the bridge loading and two more actual bridges are tested.

6.2 Traffic Load Patterning Phenomenon

6.2.1 Hypothesis

In this section, we investigate the phenomenon of traffic load patterning and address some precepts about its real behaviour and the relationship to code-implied behaviour. To do this, a hypothetical bridge is considered with an IL that is sensitive to patterned loading.

- **Study 1**: Firstly, we examine whether the natural patterning of traffic has a significant effect on bridge loading. This is done by generating several types of congestion on the bridge and examining the resulting LEs.

- **Study 2**: Secondly, we impose the code-implied traffic patterning by cropping the ILs, perfectly ignoring traffic on the beneficial parts of the IL, and examine the resulting LEs.

- **Study 3**: Finally, we examine whether it is possible for the code-implied patterned traffic to be created by the occurrence of some critically spatially arranged incidents that affect the traffic flow. For these hypothetical critical traffic scenarios, we determine the resulting LEs. The road topology can even be unrealistic as we only pursue code-referred traffic.

Comparison of the LEs from these studies is informative on both the nature of natural traffic patterning and its relation to code-implied patterning. However, before examining the results of these studies, the details of the studies are described.

6.2.2 Basis of the Studies

For the studies, a generic 1200 m bridge is used, which can be regarded as a large multi-span bridge (Figure 6-1). This geometry is reflective of some existing bridges, such as The Millau Viaduct (204+6×342+204), Charilaos Trikoupis Bridge (286+3×560+286), Brooklyn Bridge (283+487+283) and Jiaxing-Shaoxing Sea Bridge (270+5×428+270). The two traffic directions on the bridge are considered as independent, and so only one direction is considered, consisting of two lanes of traffic.
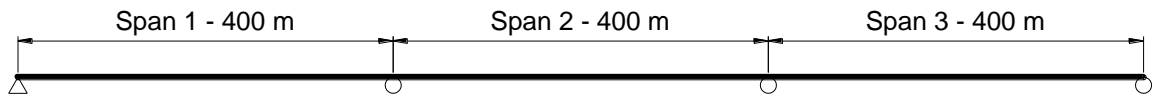
Figure 6-1. The elevation view of a generic 1200 m bridge.

For the generic bridge, one LE is considered through a hypothetical IL which is sensitive to patterning, shown in Figure 6-2. Both maximum (most positive) and minimum (most negative) values of the LE are studied. The complete IL is studied as the real response to the traffic stream (Figure 6-2(a)). Code-implied traffic patterning is considered by cropping the beneficial regions of the IL to consider the worst-case maximum LE (Figure 6-2(b)), and similarly for the worst case minimum LE (Figure 6-2(c)).
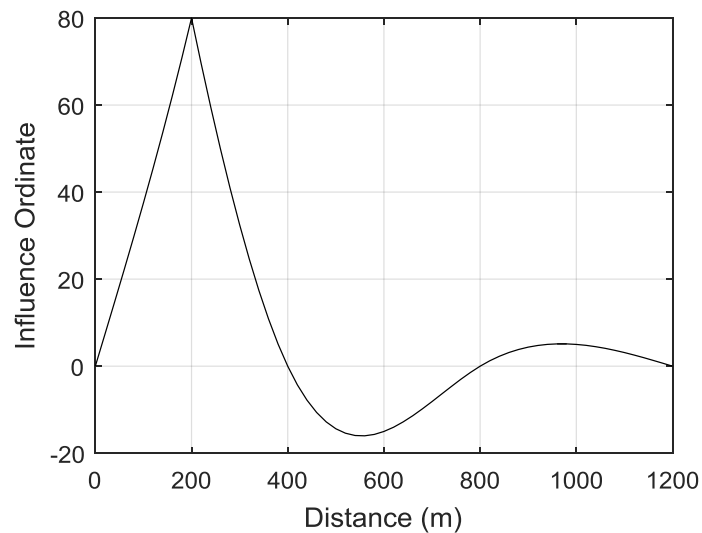
(a) Full IL
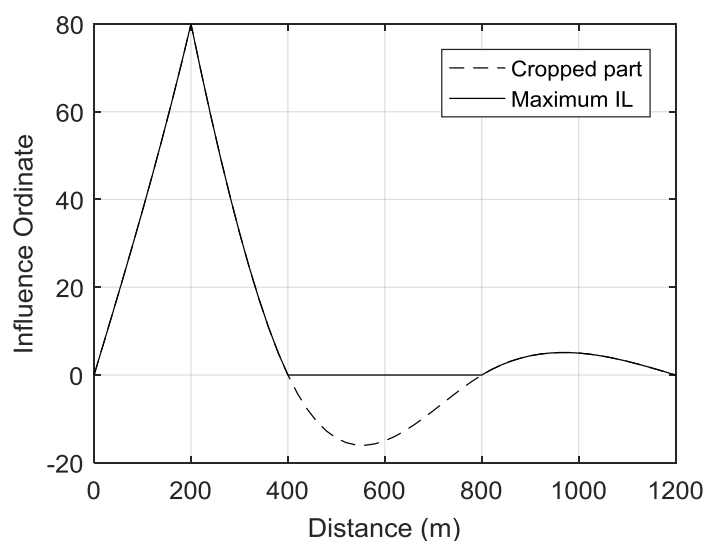
(b) Maximum IL
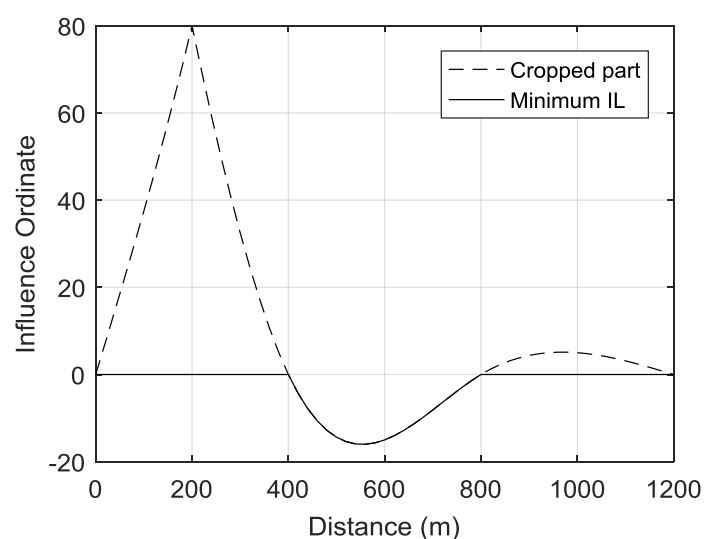
(c) Minimum IL

Figure 6-2. Hypothetical IL of a generic 1200 m long bridge for consideration of traffic patterning.

The same input traffic dataset is used throughout the work, to avoid this variable affecting the results. Since the studies are solely relative comparisons, and not intended to quantify actual values of loading, this is acceptable. The traffic characteristics are modelled on data taken from the A6 motorway near Auxerre in France. This data is significant as it formed the basis for the Eurocode load mode (Bruls et al., 1996b). The traffic used in this work is randomly generated

using Monte Carlo simulation (Jacob and Labry, 2002; Caprani, 2005). Cars were not measured at Auxerre but are artificially injected into the traffic stream for these studies, since it is vital to represent real traffic streams in the microsimulation (Caprani, 2013; Caprani et al., 2016). The traffic flow is set to 1500 veh/h/lane and the truck percentage as 16% (Lipari, 2013). Additionally, an 80:20% distribution of trucks between lanes is set for this two-lane bridge (Fwa and Li, 1995; Caprani et al., 2016).

For the studies, the road is taken as 6 km long, and the bridge is located starting at 3 km. The first 3 km is used to allow the traffic settle after injection to avoid boundary effects (Lipari, 2013). Bottlenecks are introduced into the traffic stream by locally altering the safe-time headway parameter of the IDM, as recommended by Treiber et al. (2000). This alteration is made gradually (transition part in the figures) to avoid sudden shocks to the traffic stream —see OBrien et al. (2015) for further details. The bottleneck (or transition) starts at 4.2 km – just at the end of the bridge.

For each study, 100-hours of congestion data is generated and recorded. It is considered that 1 hour of congestion occurs in each day, and so the 100 hours of congestion corresponds to 100 days of the bridge lifetime. Simultaneous to recording the value of the LE through time, the coincident total amount of load on each span, or lobe of the IL, is also recorded. The maximum LE in each simulated hour of congestion is retained for this analysis as the 'block' maximum. Of course, congestion does not occur immediately at the start of the simulation but takes time to build upon the virtual road. Hence the LEs for the first hour of the simulation are discarded as being from a mix of free- and congested-flow traffic.

6.2.3 Study 1: The Relationships between Bottleneck and Time Headway

OBrien et al. (2015) and Caprani et al. (2016) respectively consider single and multi-lane LEs caused by different forms of traffic. However, the ILs used in these works are not sensitive to load patterning. Indeed, there is little work in the literature that analyses the significance of different forms of congested traffic on ILs with multiple lobes: those ILs with alternating positive and negative regions that are sensitive to load patterning. To address this for the considered generic

bridge and hypothetical IL, a range of congestion types are generated with the layout setup in Figure 6-3.
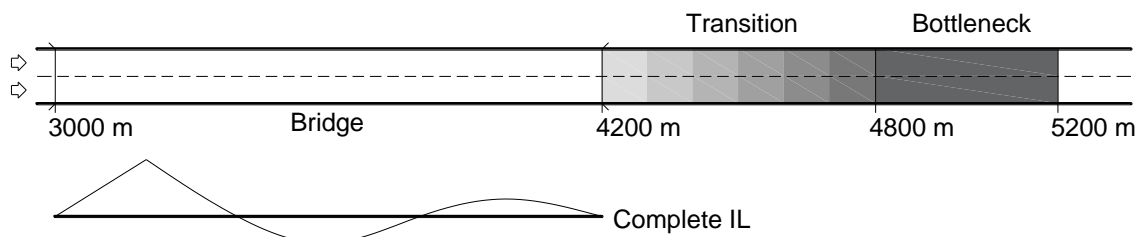
Figure 6-3. The simulation layout for Study 1.

Figure 6-4 shows the relationship between the locally-modified safe time headway parameter and resulting bottleneck strength which serves as a proxy for the type of congestion (Caprani et al., 2016). The results are close to those found in the previous papers (Treiber et al., 2000; Caprani et al., 2012; OBrien et al., 2015; Caprani et al., 2016).
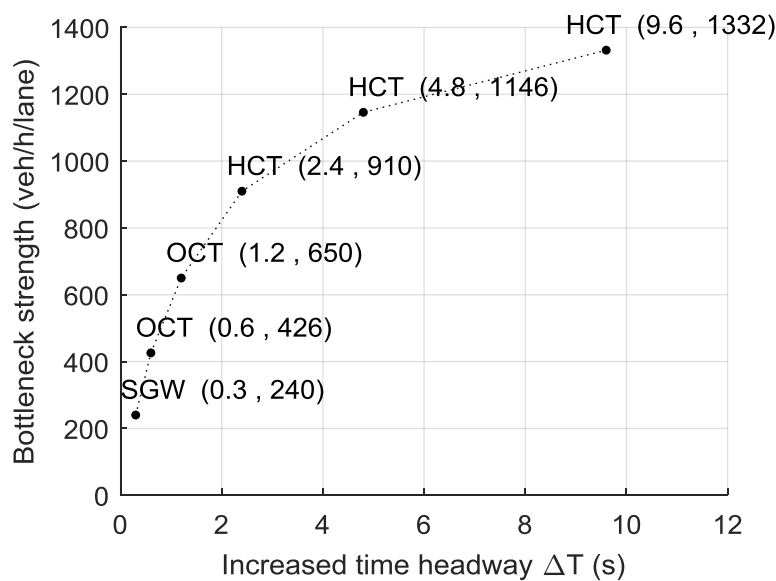
Figure 6-4. Congestion types and the relationship between time headway ΔT and bottleneck strength ΔQ. The numbers in the bracket are the exact coordinate of each dot point.

For each bottleneck strength considered, the maximum (most positive) and minimum (most negative) LEs are calculated using the extreme value extrapolation previously described (Figure 6-5). As may be expected, for the maximum LE, free flow traffic is the least onerous form of traffic, and congested

traffic types give higher LEs. Interestingly, there is a 'saddle' in the graph. The light bottleneck ΔQ = 240 veh/h and strongest bottleneck ΔQ = 1332 veh/h both trigger high LEs. These correspond to SGW and HCT congestion respectively. The fact that stop-and-go-wave traffic gives high LEs indicates that the natural 'pressure waves' in traffic do cause onerous LEs for patterning-sensitive ILs. Further, these LEs are similar to those caused by the most onerous form of traffic, HCT, which is the one that codes of practice attempt to replicate. Finally, the LE caused by second strongest bottleneck ΔQ = 1146 veh/h veh/h is similar to that of the strongest bottleneck ΔQ = 1332 veh/h, but the simulation time is far shorter. Besides, the vehicle speed before these two bottlenecks are 5 km/h and 3 km/h, respectively. The bottleneck ΔQ = 1332 veh/h for the 3 km/h is too severe, which is too unrealistic. Consequently, for Study 2 and Study 3, the bottleneck of ΔQ = 1146 veh/h is used.
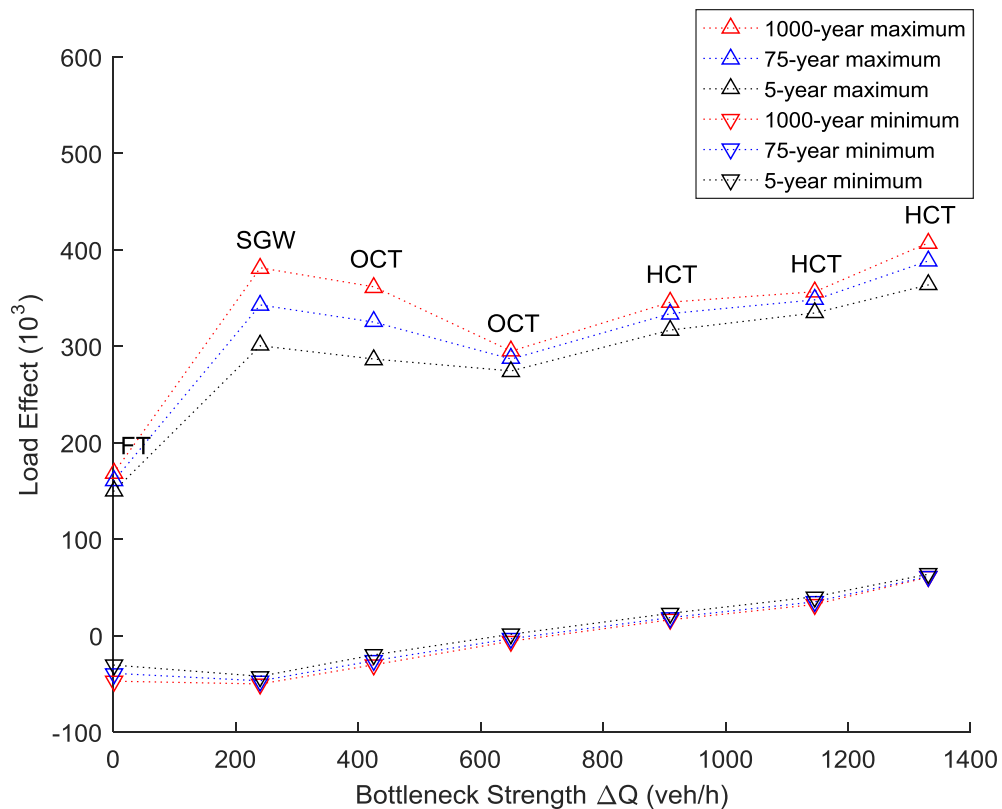
Figure 6-5. Relationship between middle bottleneck strength and extrapolated LE in Study 1.

Similar to the maximum LE result, for the minimum LE, the congested traffic types give the most severe loading. Most interestingly, the SGW bottleneck ΔQ = 240 veh/h yields the minimum LE. This is further evidence that natural variations in

the traffic are important for patterning-sensitive ILs. Further, by comparing the critical form of traffic for the maximum and minimum results, the ratio of the areas of the positive and negative lobes of the IL also plays a role in determining the most onerous form of congested traffic. The critical bottleneck of $\Delta Q = 240$ veh/h is selected as the characteristic minimum LE for Study 1.

A useful visual representation of the traffic state is a spatio-temporal space mean speed (ST-SMS) plot (Treiber and Kesting, 2013). For the two critical types of traffic identified above, $\Delta Q = 240$ veh/h and $\Delta Q = 1146$ veh/h, the ST-SMS plots are shown in Figure 6-6. The difference in behaviour of the SGW and HCT forms of congestion is clear, and it is also clear that the pressure waves of the SGW are responsible for the high negative (minimum) LE observed. Of course, these findings are intuitively obvious, but the methodology adopted here allows their quantification and enables further analysis of less intuitive results.

(a) ΔQ = 240 veh/h traffic
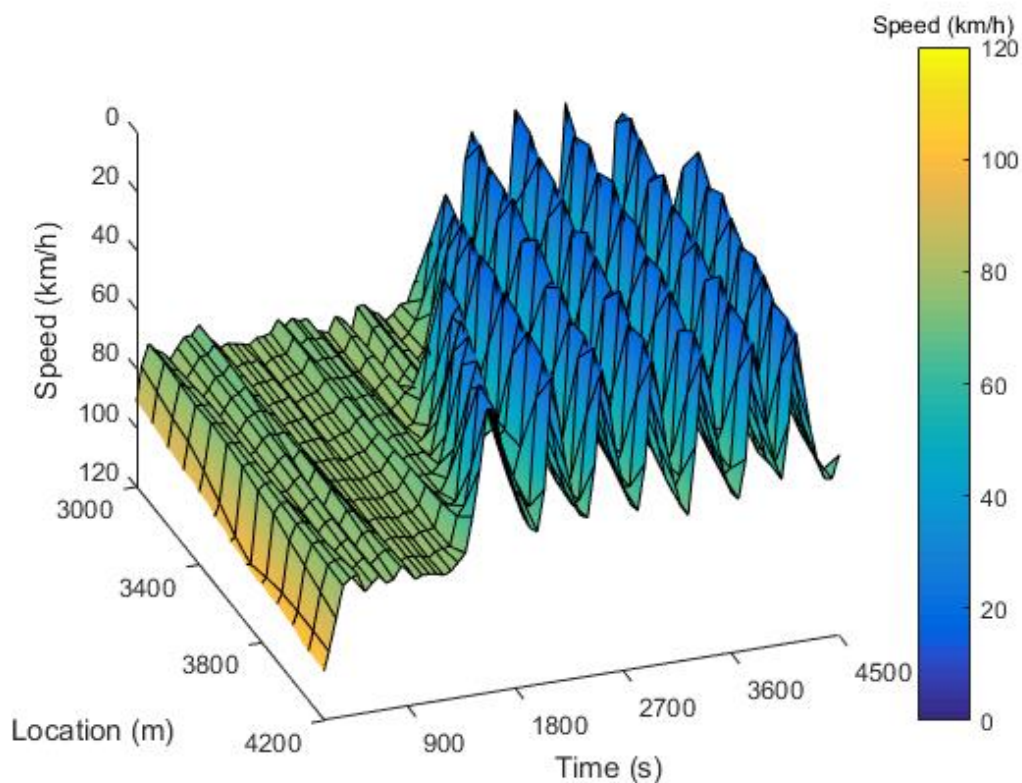
(b) ΔQ = 1146 veh/h traffic
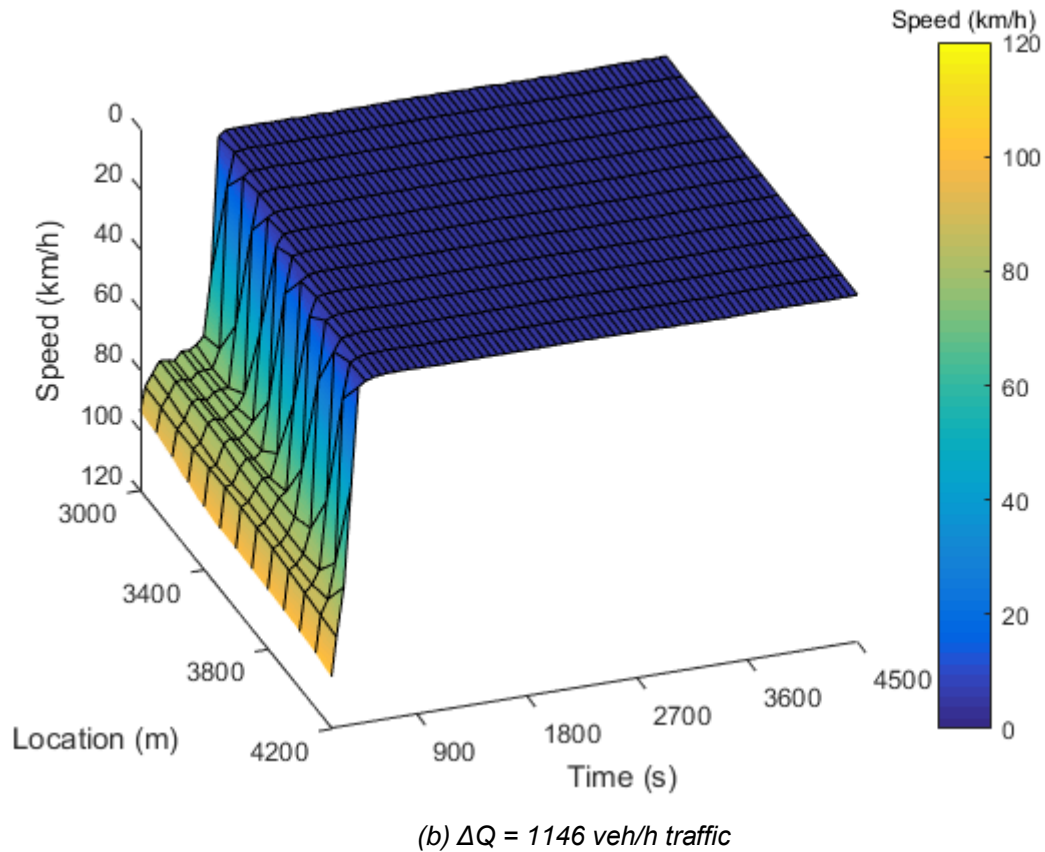
Figure 6-6. ST-SMS plots in Study 1.

6.2.4 Study 2: Comparison between Real LE and Load Patterned LE

In this study, the implications of typical code requirements to pattern live load are examined. The road and bridge layout for this study is shown in Figure 6-7. For the traffic stream simulated, this is affected by cropping the ILs as noted earlier, to remove contributions of the load from regions that are beneficial to the effect of interest. From the results of Study 1, the bottleneck strengths $\Delta Q = 1146$ veh/h is used to cause HCT traffic in Study 2, which generates the maximum loading on the adverse or beneficial parts, leading to the maximum and minimum LEs. The layout (b) functions as a check to illustrate that transition has an ignorable impact on the LEs.

(a) Layout with transition part

(b) Layout without transition part
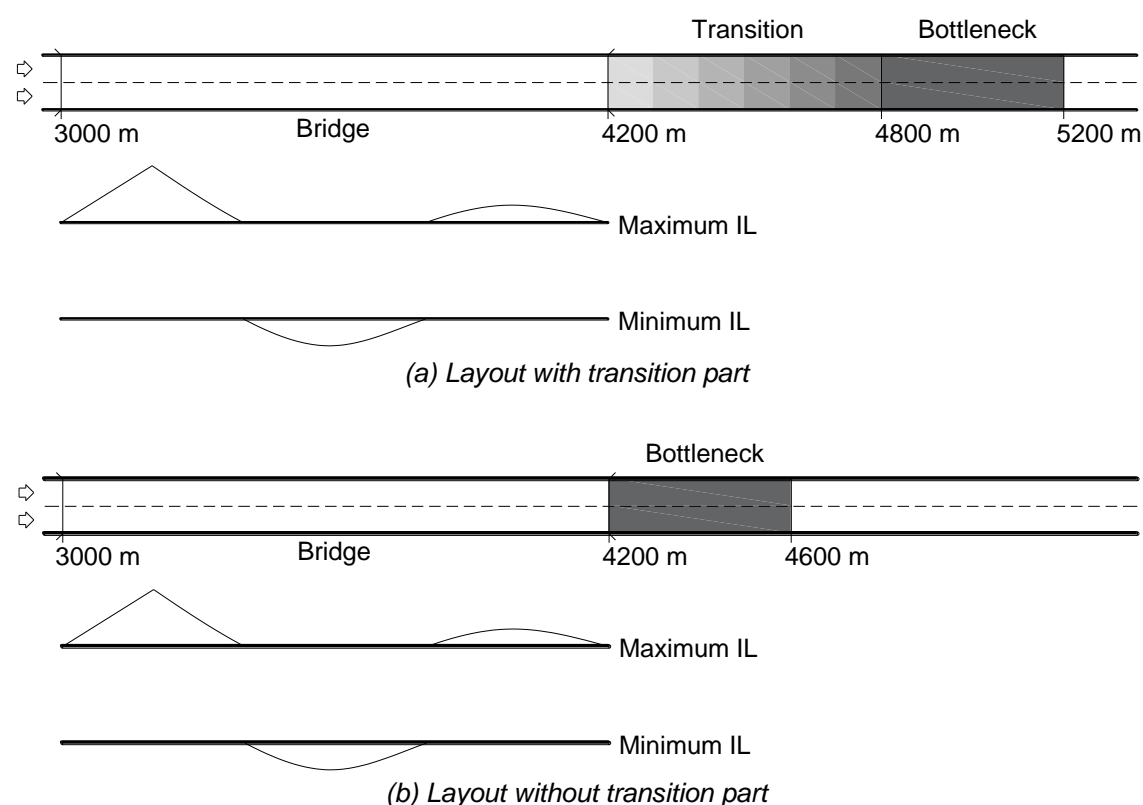
Figure 6-7. The simulation layout for Study 2.

The characteristic maximum and minimum LE results are calculated as described earlier. The results are expressed as a ratio to those of Study 1, for the bottleneck considered, and given in Table 6-1. The total coincident loads on each span are also extrapolated and converted to an EUDL, and these are shown in Figure 6-8.

Table 6-1. LEs of a generic bridge, expressed as a ratio of the real traffic results from Study 1

LE	Return period	Study 1	Study 2		Study 3	Proposal
		Bottleneck transition	Bottleneck transition	No transition	Two bottlenecks	
Maximum	5	93.8%	114.3%	109.2%	107.2%	106.7%
	75	97.6%	120.1%	113.1%	113.0%	111.0%
	1000	100.0%	124.2%	115.6%	117.2%	113.8%
Minimum	5	84.1%	205.6%	195.5%	130.7%	109.6%
	75	93.5%	216.7%	203.6%	141.3%	118.3%
	1000	100.0%	224.4%	208.9%	148.0%	124.1%

For the maximum LE, the patterned traffic gives 24.2% higher value than real traffic. The reason for this is evident from the EUDLs in Figure 6-8: as the congestion traffic states for the characteristic LEs are the same, the EUDLs on spans 1 and 3 are quite similar. Thus, the major difference arises from the beneficial effect contributed from the load in span 2. For the minimum LE, the difference becomes quite considerable at 124.4% of the LE for real traffic. Two aspects are different for this case: the critical traffic is SGW in the actual traffic (ΔQ = 240 veh/h), and the ratio of the beneficial/adverse areas of the IL is different. Nevertheless, it is interesting to note that the coincident EUDLs on the adverse portions of the IL, for both maximum and minimum, situations are quite similar (around 24.6 and 23.9 kN/m respectively – quite close to Eurocode's 27 kN/m). Overall though, the level of conservatism in the load patterning approach is seen to be significant, at least for this bridge and IL.
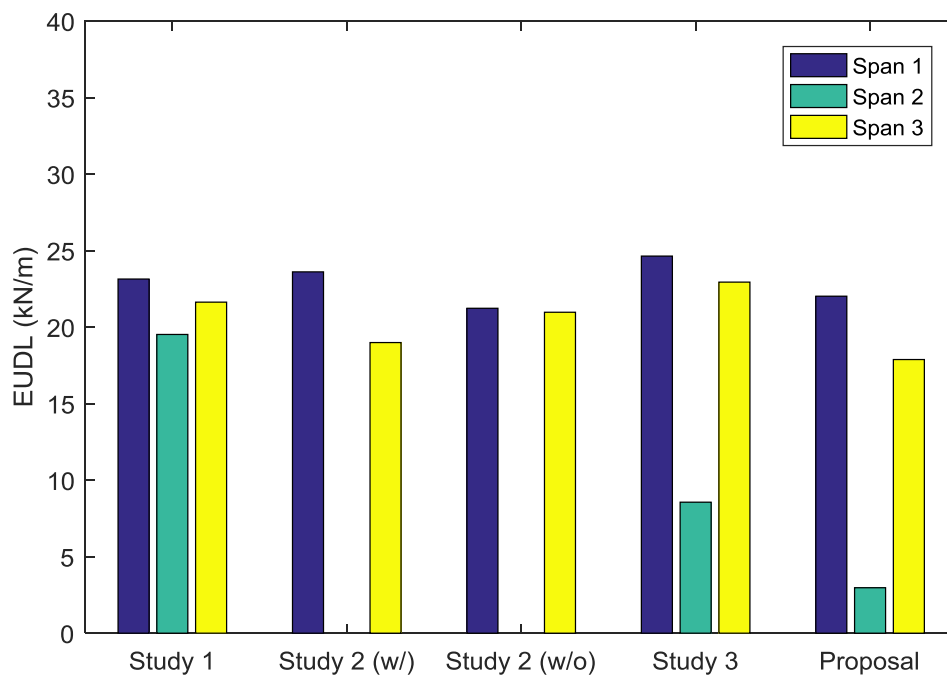
(a) Maximum LE

(b) Minimum LE
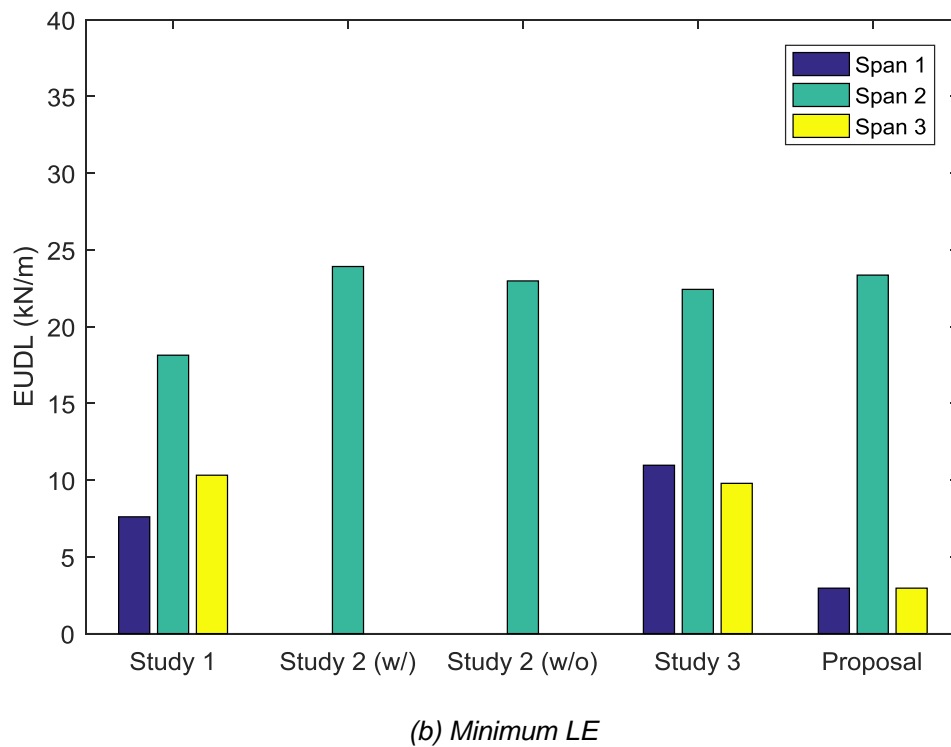
Figure 6-8. 1000-year extrapolated EUDL arrangement of a generic 1200m bridge.

In Study 1, the typical arrangement of a gradual introduction of the bottleneck is adopted, as explained earlier. However, to make the bottlenecks occur at the critical locations relative to the bridge for this study, the transition would overrun the intended bottleneck location on the bridge at 3.4-3.8 km (see Figure 6-3). Therefore, an initial simulation was conducted to determine the influence of the transition region on the resulting LEs. This road layout is shown in Figure 6-7(b), and the results given in Figure 6-8. It is clear that the results are not much affected by the absence of the transition region.

6.2.5 Study 3: Cause of the Critical Case Load Patterning

In this study, we examine the possibility of traffic becoming patterned in the manner implied by codes. To do this, we hypothesise the occurrence of two traffic incidents, at the same time, located at exactly the critical positions for this IL, to cause both worst-case maximum and minimum LE values. As the rationality of the road is not the priority, and the most code-referred traffic is of concern, we assume two bottlenecks are formed in this short distance, and the bottleneck strengths are suddenly changed. Figure 6-9(a) shows the hypothesised road layout for the worst-case scenario maximum LE, while Figure 6-9(b) shows that

for the minimum. The bottleneck strength in bottleneck 1 varies while that in bottleneck 2 is 1146 veh/h/lane.

(a) Maximum LE

(b) Minimum LE
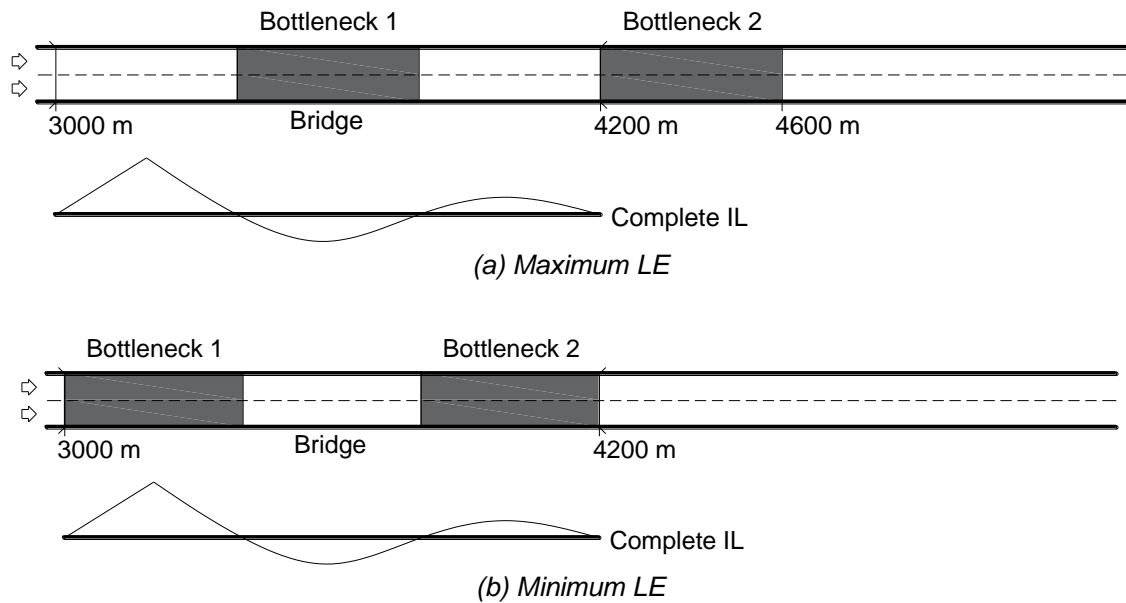
Figure 6-9. The simulation layout for Study 3.

The additional bottleneck on the bridge is found to interact with the first bottleneck, limiting the throughput of vehicles in total. Therefore, several trial bottleneck strengths for the additional region are conducted. Again, in a worst-case scenario approach, we select the bottleneck strength that reduces to a minimum the traffic density at the beneficial parts of the IL, while making the density on the adverse part a maximum. If the bottleneck strength is too small, there would be too many vehicles in the middle span. While if the bottleneck strength is too large, the full congestion on the span 3 will take much longer to occur. In short, there is a trade-off between the vehicle density and congestion formation time. The result indicates that a bottleneck strength of $\Delta Q = 1073$ veh/h at the second incident location is suitable.

Spatio-Temporal density plots illustrate the vehicle numbers on the road sections. Figuratively then, the code-implied spatio-temporal density plot would have a maximum density on the adverse regions and zero traffic density on the beneficial regions. This situation is shown in Figure 6-10, and this is considered the target load patterned traffic densities. Note that in this figure, a maximum possible density of 250 veh/km (100% cars of 4 m length positioned bumper to

bumper) is shown. Corresponding to the target spatio-temporal plot, Figure 6-11 shows the actual spatio-temporal densities achieved in the simulation of the road layout in Figure 6-9a. It is seen that the road layout generates quite a similar result to the target, with a large number of the vehicles occupying the adverse parts. However, there are two aspects to note: (a) the lowest density in the beneficial region occurs as traffic builds up at the second incident, since the vehicles can travel at high speed; (b) once the second incident has caused a high-density backlog of vehicles, a non-zero density of vehicles exists in the adverse portion of the IL. Interestingly, for this optimised bottleneck setup (ΔQ_1 =1073 veh/h and ΔQ_2 = 1146 veh/h), the beneficial region has around 80 veh/km, which is close to that of free-flow traffic. The result for the minimum follows the same logic and it is listed in Table 6-1.
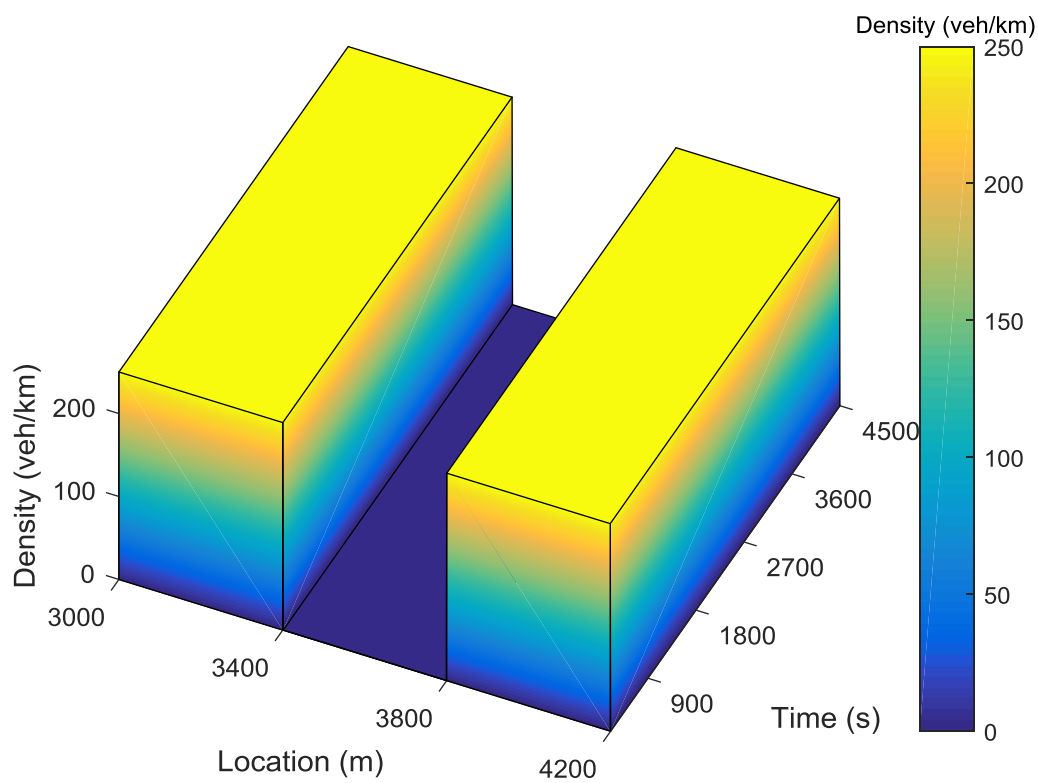
Figure 6-10. ST-Density plot for the target load pattern of maximum LE
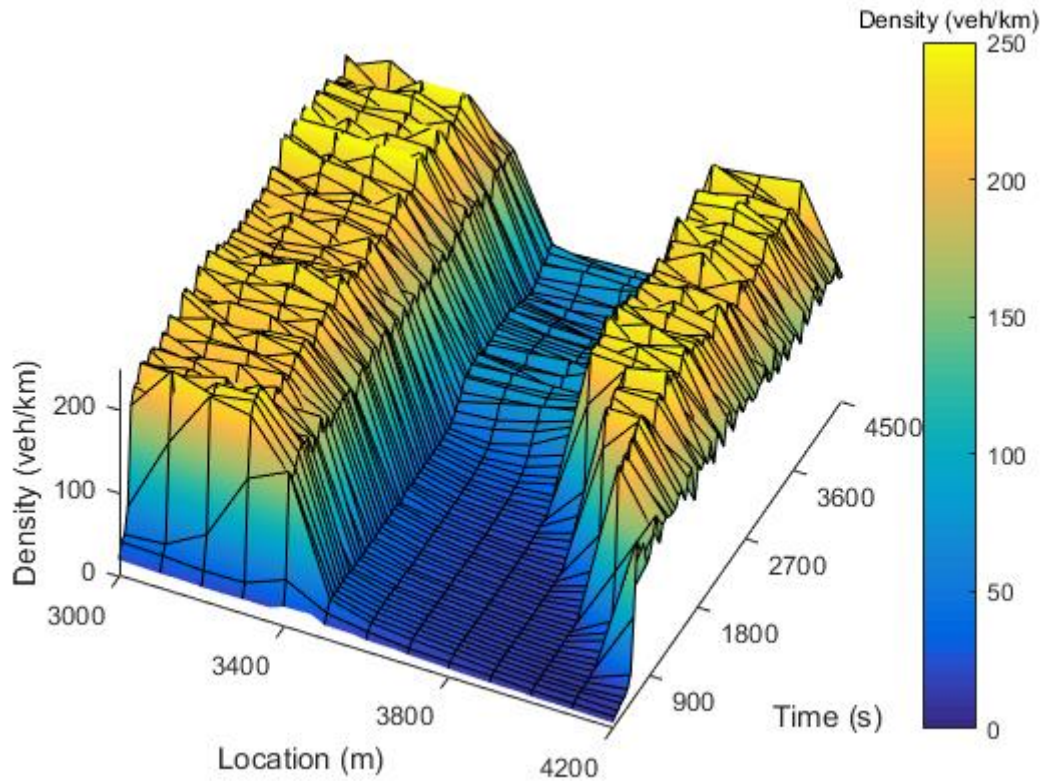
(a). ST-Density plot for the actual load pattern of maximum LE
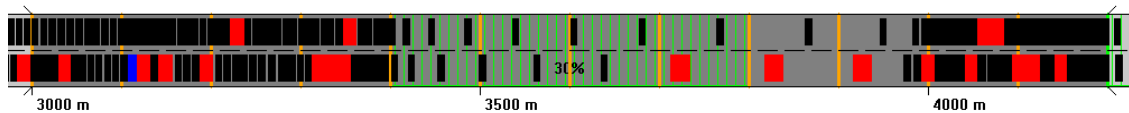
(b). the vehicle topology at time 1000 s in (a)
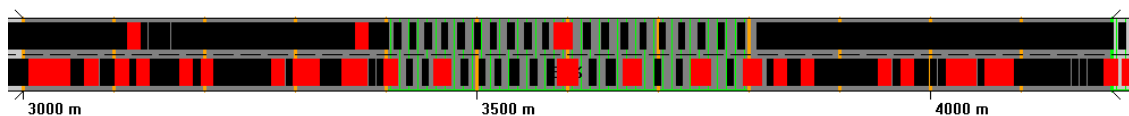
(c). the vehicle topology at time 3000 s in (a)

Figure 6-11. ST-Density plot for the actual load pattern of maximum LE and its corresponding traffic at different times. Note that the black boxes are cars and red boxes are trucks in SIMBA.

This study shows that it is possible to come close to code-implied traffic patterning. However, multiple aspects must converge to make this possible: incidents must occur at the right locations, and at a very specific set of inter-related bottleneck strengths. The joint probability of these occurrences is infinitesimally small for regular traffic situations. Finally, and importantly, despite

the worst-case scenario approach, the results also show that it is not possible to have no traffic on the beneficial parts of the IL. Clearly then, a more rational approach to load patterning is needed.

6.3 Innovative Method of Load Patterning

6.3.1 Proposed Approach

The results of the previous studies demonstrate that it is impossible to obtain the code-implied traffic topology for real traffic. This is not to say that engineers should not consider a worst-case scenario approach, but if it is, it could conceivably be better treated as an accidental load case. For lifetime levels of in-service (non-accidental) loading scenarios, it is prudent to propose a load patterning scheme that is commensurate with the phenomenon of traffic loading. Nevertheless, in doing so, we ignore the improbability of joint occurrence of onerous events and consider that the road topology is a worst-case scenario and that the bottleneck strengths are also worst-case-scenario. Clearly these conservative assumptions could be relaxed in future work.

For our proposal, we consider both the results of Study 3 in combination with the well-known load combination method, Turkstra's Rule (Turkstra and Madsen, 1980). Mathematically, Turkstra's Rule can be expressed as:

$$X_{\max,T} = \max\{[\max(x_1) + \bar{x}_2], [\bar{x}_1 + \max(x_2)]\} \qquad (26)$$

where $X_{max,T}$ is the maximum combined LE in period T; x_1 and x_2 are two sources of loading, with maximum lifetime levels and mean values indicated. In the context of this work, the various sources of loading can be considered as types of traffic on the adverse and beneficial parts of the ILs. Based on the results of the phenomenological studies, the maximum load process is considered as the HCT traffic, and the average load process is free-flow traffic. Based on this then, the proposal for load patterning is shown in (b) Layout for the minimum LE

Figure 6-12 for maximum and minimum LE on the example generic bridge IL: adverse portions are covered with a congested traffic loading, which is the same as current practice, but in addition, the beneficial parts are covered with free-flow traffic loading.

(a) Layout for the maximum LE

(b) Layout for the minimum LE
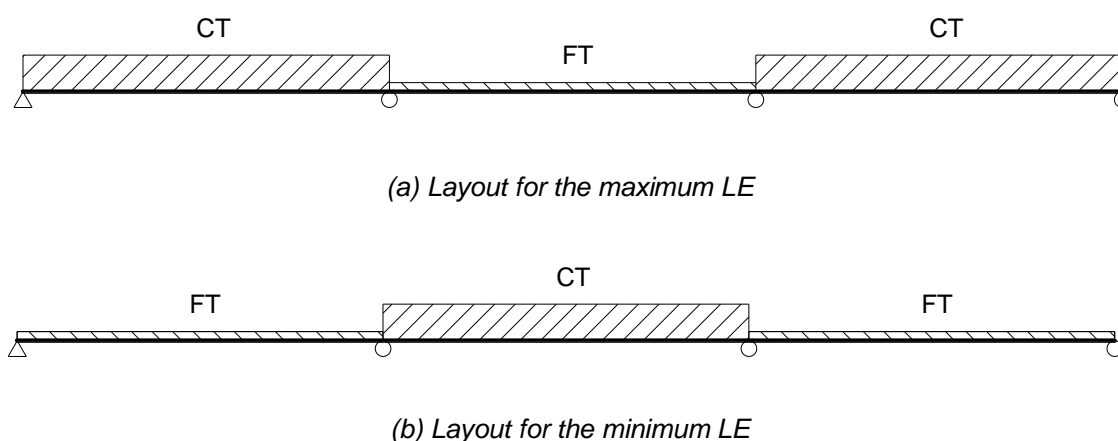
Figure 6-12. Layouts for the proposal. FT is free flow traffic and CT is congested traffic.

6.3.2 Implementation using Traffic Microsimulation

The proposed load patterning approach is easily implemented using traffic microsimulation. Since there are two different traffic types involved, the simulation is run twice, as follows:

- For the HCT traffic, the adverse portions of the IL are considered, and the beneficial portions cropped. As before, in each 1-hour block, the block maximum HCT LE is noted, and the characteristic extreme LE calculated.
- For the mean FT LE, the beneficial portions of the IL are considered, and the adverse portions cropped. The temporal average of the complete time-history of resulting FT LE is calculated.

The lifetime LE is then the combination of the two results. The HCT LE is the same as the prevailing method, and so the benefit of the FT (beneficial) LE represents the improvement of our approach to current practice.

The LE results for the proposal are shown in Table 6-1. All values are compared to those of Study 1 from earlier. The proposed load patterning approach gives similar results to those of Study 3. Compared to Study 2 results (current practice), up to a 105% reduction for the minimum 100-year characteristic LE can be observed. The EUDL for the proposed approach on each span is shown in Figure 6-8, along with those of the earlier studies. Again, it is clear that our proposal is quite similar to Study 3. It is neither entirely congested with the traffic as Study 1 indicates, nor are no vehicles applied to the beneficial parts as Study 2 (current practice) indicates. For the minimum LE, the load on span 2 is consistent with

Page | 96

that of Study 2 but maintains the onerous loads of Study 1 on the remaining. It is seen from these results that our approach is a compromise between real traffic behaviour and current practice.

6.3.3 Implementation using Design Code Traffic Live Load Models

Mean free-flow traffic loading is not readily available from codes of practice. A means to determine the mean free-flow traffic from the code live load model, which is typically based on lifetime levels of HCT loading, is needed. However, since it is being used for beneficial portions of the IL, it is not appropriate to overestimate it. Writing the code lifetime loading as w^*, we propose that the mean free-flow traffic is determined from the code stipulated loading as:

$$w_{FF} = \frac{k}{\lambda} w^*$$

(27)

In this, k is the ratio of mean daily maximum congested traffic to mean free flow traffic, and λ is the bias factor of the loading distribution: the ratio of lifetime characteristic extreme to mean daily maximum loading, all considered as being for HCT. The ratio k is approximately 0.25, based on results from Lipari (2013), OBrien et al. (2015) and Caprani et al. (2016).

Considering traffic loading to the Gumbel-distributed as is common, Caprani et al. (2017) show that the ratio of characteristic value to mean value (the bias factor) is given by:

$$\lambda = \frac{1 + r s_p}{1 + r \gamma}$$

(28)

where the ratio of scale to location parameter, r, of the Gumbel distribution is given by:

$$r = \frac{\theta}{u} = \left(\frac{\pi}{CoV\sqrt{6}} - \gamma \right)^{-1}$$

(29)

and coefficient of variation, CoV, is the ratio of the standard deviation to mean value. The SEV is $s_p = -\ln(-\ln(1-p))$ where p is the probability of exceedance. As before, we consider there to be 250 working days per year, and so $p = 1/(250 T_R)$. Consequently, once the return period, T_R, and CoV are known, the bias factor of

Equation 28 can be found. Table 6-2 gives the ratios of congested traffic lifetime loading levels to mean free-flow ($w*/w_{FF}$) for some selected *CoV* of loading. Typically, traffic loading is considered to have a *CoV* of around 0.18 and so depending on the design life or return period of the code in use, the mean free flow traffic can be estimated from Table 6-2. For example, the Eurocode has a UDL component of 27 kN/m for a standard lane, and is based on a 1000-year return period, so its mean free-flow traffic can be estimated as 27/10.65 = 2.53 kN/m (for a lane).

Table 6-2. Ratios of congested traffic lifetime loading levels to mean free-flow (w/wFF) for different CoV of loading based on k = 0.25.*

CoV	Return Period (years)			
	5	75	100	1000
0.12	6.45	7.47	7.57	8.43
0.16	7.27	8.62	8.77	9.91
0.18	7.68	9.20	9.36	10.65
0.20	8.09	9.78	9.96	11.39
0.24	8.91	10.93	11.15	12.87

6.4 Case Study Applications

Two case study bridges are selected to demonstrate the application of the proposed traffic load patterning approach. The two bridges are the Queensferry Crossing, a four-lane bridge with a total length of 2700 m, and Golden Gate Bridge, a six-lane bridge with a total length of 2737 m. Although the traffic on both bridges is two-way traffic, only one direction is considered, as before. For both bridges, the input traffic data is the same as that of the generic bridge considered earlier, and the same input flow rate per lane is used. The ILs for these two bridges are shown in Figure 6-13. The IL for the Queensferry Crossing is estimated from drawings for the central tower bending moment (Jacobs and Arup, 2009), and the IL for the Golden Gate Bridge is taken from Enright et al. (2013). The road topologies of Studies 1 and 2 (Figure 6-3 and Figure 6-7a) are used as a comparison to the proposed approach.

(a) Central tower bending moment of Queensferry Crossing

(b) Bending moment at the middle span of Golden Gate Bridge.
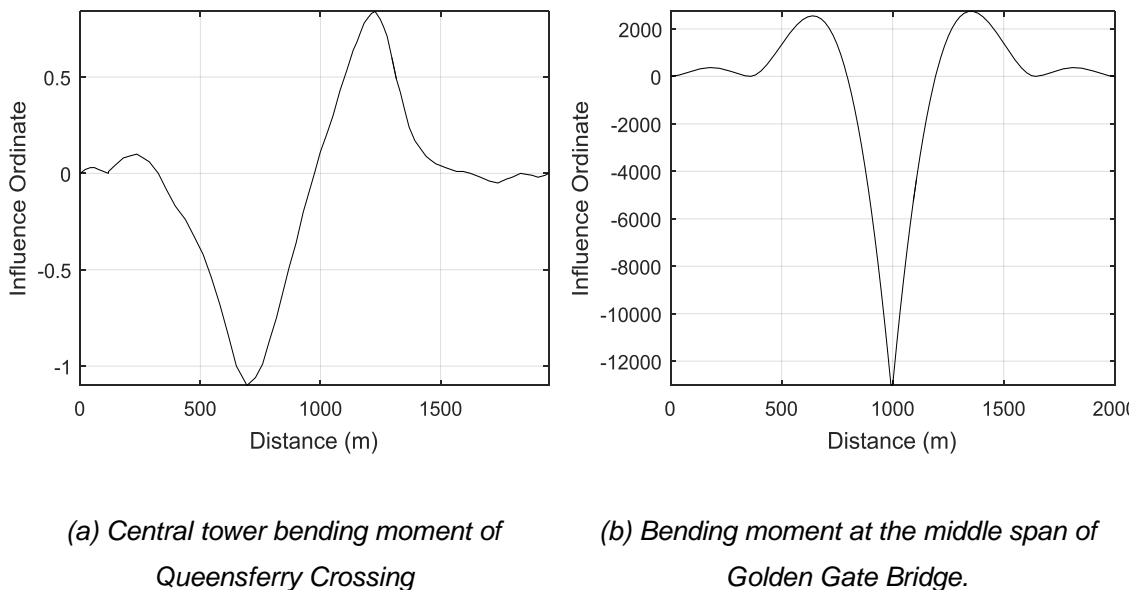
Figure 6-13. ILs of the two existing bridges

Table 6-3 summarises the 1000-year relative results for both the Queensferry Crossing and Golden Gate Bridge. It can be inferred that the Study 1 (actual LE) is lowest, as expected. The LEs from the proposed approach are smaller than those of the onerous Study 2 scenario, by up to 31.3% actual traffic (Study 1). Therefore, it can be concluded that the proposed approach is still conservative

but has a more rational than the traditional load patterning approach for long-span bridge assessment and design.

Table 6-3. Case study application of proposed method to two bridges

Bridge	LE (1000 year)	Study 1	Study 2	Proposal
Queensferry Crossing	Maximum	100.0%	127.3%	110.0%
	Minimum	100.0%	126.8%	119.1%
Golden Gate Bridge	Maximum	100.0%	300.9%	269.6%
	Minimum	100.0%	136.3%	125.1%

Earlier it was noted that the critical form of traffic seems sensitive to the relative areas of adverse and beneficial regions of the IL. Table 6-4 summarises the results for the three bridges considered in this paper, compared against the relative influence lobe areas. The differences in LE between the proposed approach and current practice (Study 2) are given and shown along with the coincident EUDLs applied to each lobe of the IL. It is interesting to note that the EUDL on the beneficial regions of the IL, is around 12% (1/9) of that on adverse parts.

Table 6-4. IL area ratios, 1000-year characteristic LE and EUDL ratios for experiment bridges.

Bridge	IL Area Ratio		The 1000 Year Difference[1]		EUDL ratio[2]	
	Positive	Negative	Max.	Min.	Max.	Min.
Generic 1200	80%	20%	8%	45%	8.05	8.56
Queensferry Crossing	40%	60%	14%	6%	9.30	8.97
Golden Gate Bridge	40%	60%	10%	8%	9.63	10.72

[1] The LE ratio between the Proposal to Study 2 (traditional load patterning method).
[2] EUDL ratio is the ratio between EUDL at beneficial IL region and EUDL at adverse IL region.

CHAPTER 7
CONCLUSIONS AND FURTHER RESEARCH

7.1 Conclusions

This thesis aims to improve the traffic load estimation for long-span bridges in three aspects: axle-to-axle gaps, load model design, and load patterning. The wheel locations are obtained by the new PWF-based algorithm for more accurate axle-to-axle gaps, and the result is compared with the existing algorithms. We also examined the current load models and their means of load patterning. The load models are compared quantitatively with new proposed metrics. Traffic microsimulation is used to simulate the vehicles on the bridges, which mimics the traffic load patterning. Major conclusions from this thesis are:

- A new method based on a PWF and circularity is described. The likelihood of a location in an image being at the centre of a circle is calculated based on the response to the PWF combined with the circularity of the object. The proposed algorithm, Hough Transform, Template matching and DPM methods, are applied to a sample set of 80 cars.

- The PWF-based algorithm is a less complex algorithm and no training or validation is needed, which is a key advantage. The results show that the proposed method is viable for locating wheels in images of traffic and should, therefore, find good use in a range of traffic applications.

- The relationship between bridges and vehicles, and the resulting LEs is complicated, but some trends are identified. Peakedness and concentration are proposed as the metrics for the bridge and the vehicle, respectively. The metrics can identify the different the shape of the ILs and different vehicle configurations. The relationship is found to be complicated due to a considerable number of variables involves but the trends are clear. Lower peakedness ILs always yield the most adverse LE when comparing in the same bridge length. The critical cases for peaked ILs are relatively high-concentrated vehicles while relatively low-concentrated vehicles govern the flat ILs. However, there is a trade-off between the concentration and LE. The most concentrated vehicle and least concentrated vehicle are not generally the most critical.

- A new 3D plot tool is developed. It illustrates the vehicle distribution feature, bridge IL feature as well as the LE quantitatively in the same figure, which indicates relationship for the given vehicle and the given bridge. It

can examine the current load models and help the next-generation load model design.

- By using the load model design tool, it is expected that the new load model should correspond to the local traffic. If possible, a larger dataset is recommended.

- As the axle spacing, axle loads and loading sequence vary, there are many combinations. For load model design, it is expected to see many candidate load models.

- Current codes and standards use a quite conservative load patterning approach to determine the live load on the bridge. It only considers the worst-case scenario theoretically but ignores the probabilities of occurrence. The LE of load-patterned traffic is more than doubled the actual traffic. The traffic flow in beneficial regions of the IL is idealised. It is not possible that no vehicles are on the road between two adjacent congestion regions.

- Based on the possible road topology from SGW, a new load pattern is proposed to estimate the LEs more precisely for long-span bridges. It is found that the SGW can trigger worst-case scenario as well, which is usually ignored. The new load patterning method considers not only HCT on the adverse parts of the ILs but also FT on the beneficial parts. The LE estimation can be reduced up to 45% from the traditional way. It is strongly recommended for MSLB, whose ILs usually are alternate up and down. The load on the free flow region can be determined by using of congested traffic lifetime loading levels to mean free-flow ratio.

7.2 Recommendations for Further Research

Key aspects for further work identified are:

- More complicated cases can be investigated such as multi-lane factors, bidirectional traffic, and dynamic effects. Also, more bridges with different ILs should be analysed, and there still is a space for improvement in the traffic load estimation.

- The proposed concentration algorithm is still not perfect due to the limitation on the equivalent axle number calculation. Further development is needed for more complicated cases.

REFERENCES

AASHTO 2007. Bridge Design Specifications, Si Units. Washington DC: American Association of State Highway and Transportation Officials.

ACHLER, O. & TRIVEDI, M. M. Camera based vehicle detection, tracking, and wheel baseline estimation approach. Intelligent Transportation Systems, 2004. Proceedings. The 7th International IEEE Conference on, 2004a. IEEE, 743-748.

ACHLER, O. & TRIVEDI, M. M. Vehicle wheel detector using 2D filter banks. Intelligent Vehicles Symposium, 2004 IEEE, 2004b. IEEE, 25-30.

AMERICAN ASSOCIATION OF STATE HIGHWAY AND TRANSPORTATION OFFICIALS 1931. Standard Specifications for Highway Bridges and Incidental Structures, 1st Edition.

AMERICAN ASSOCIATION OF STATE HIGHWAY AND TRANSPORTATION OFFICIALS 1944. Standard Specifications for Highway Bridges and Incidental Structures, 4th Edition.

AMERICAN ASSOCIATION OF STATE HIGHWAY AND TRANSPORTATION OFFICIALS 2017. AASHTO LRFD Bridge Design Specifications, 8th Edition.

ASCE 2017. ASCE 2017 Report Card for America's Infrastructure.

AUSTRALIAN BUREAU OF STATISTICS 2017. Motor Vehicle Census, Australia.

BALLARD, D. H. 1981. Generalizing the Hough transform to detect arbitrary shapes. *Pattern recognition,* 13**,** 111-122.

BAOHUA, Z., YUANCHUN, J., JIANFENG, Z., DAHUA, Y. & QUANLIN, Z. Fingerprint Template Matching Algorithm Based on Daubechies Wavelet. Communication Software and Networks, 2009. ICCSN'09. International Conference on, 2009. IEEE, 807-811.

BRITISH STANDARDS INSTITUTION 1978. BS 5400-2:1978 Steel, concrete and composite bridges. *Specification for loads.*

BROCKFELD, E., KüHNE, R. & WAGNER, P. 2004. Calibration and validation of microscopic traffic flow models. *Transportation Research Record: Journal of the Transportation Research Board***,** 62-70.

BRULS, A., CALGARO, J., MATHIEU, H. & PRAT, M. 1996a. ENV 1991, Part 3: The main models of traffic loads on road bridges Background studies. *IABSE REPORTS***,** 215-228.

BRULS, A., CROCE, P. & SANPAOLESI, L. 1996b. ENV1991 - part 3: traffic loads on bridges: calibration of road load models for road bridges. *IABSE reports,* 74.

BUCKLAND, P. G. 1981. Recommended design loads for bridges. *Journal of the Structural Division,* 107.

BURGOYNE, C. J. 1987. Calculation of shear and moment envelopes by Macauley's method. *Engineering Computations,* 4**,** 247-255.

CANNY, J. 1986. A computational approach to edge detection. *IEEE Transactions on pattern analysis and machine intelligence***,** 679-698.

CAPRANI, C. 2013. *Traffic Microsimulation for Bridge Loading Assessment and Management*.

CAPRANI, C. & OBRIEN, E. The governing form of traffic for highway bridge loading. 2008.

CAPRANI, C., OBRIEN, E. & LIPARI, A. 2011. Extension of a lane-changing model to a micro-simulation tool. *Proceedings of the Irish Transport Research Network 2011, Cork, 31 August-1 September 2011.*

CAPRANI, C. C. 2005. Probalistic analysis of highway bridge traffic loading.

CAPRANI, C. C. 2012. Calibration of a Congestion Load Model for Highway Bridges Using Traffic Microsimulation. *Structural Engineering International,* 22**,** 342-348.

CAPRANI, C. C., LIPARI, A. & OBRIEN, E. J. 2012. Load effect of multi-lane traffic simulations on long-span bridges. *Bridge Maintenance, Safety, Management, Resilience and Sustainability.* CRC Press.

CAPRANI, C. C., MELHEM, M. M. & SIAMPHUKDEE, K. 2017. Reliability analysis of a Super-T prestressed concrete girder at serviceability limit state to AS 5100:2017. *Australian Journal of Structural Engineering,* 18**,** 60-72.

REFERENCES

CAPRANI, C. C., OBRIEN, E. J. & LIPARI, A. 2016. Long-span bridge traffic loading based on multi-lane traffic micro-simulation. *Engineering Structures,* 115**,** 207-219.

CAREY, C., CAPRANI, C. C. & ENRIGHT, B. 2017. A pseudo-microsimulation approach for modelling congested traffic loading on long-span bridges. *Structure and Infrastructure Engineering***,** 1-14.

CASTILLO, E. 2012. *Extreme value theory in engineering*, Elsevier.

CEN 2003. EN 1991-2:2003 Eurocode 1: Actions on Structures. *Part 2: Traffic Loads on Bridges.* Brussels: European Committee for Standardization.

CHEN, C., LI, L., HU, J. & GENG, C. Calibration of MITSIM and IDM car-following model based on NGSIM trajectory datasets. Vehicular Electronics and Safety (ICVES), 2010 IEEE International Conference on, 2010. IEEE, 48-53.

CHEN, N.-S., HARTMANN, G. & DRUE, S. Circle location from intensity and range data using the singular value decomposition. Pattern Recognition, 2000. Proceedings. 15th International Conference on, 2000. IEEE, 774-777.

CHO, H., RYBSKI, P. E. & ZHANG, W. Vision-based bicycle detection and tracking using a deformable part model and an EKF algorithm. Intelligent Transportation Systems (ITSC), 2010 13th International IEEE Conference on, 2010. IEEE, 1875-1880.

CHO, H. G., RYBSKI, P. E., BAR-HILLEL, A. & ZHANG, W. D. 2012. Real-time Pedestrian Detection with Deformable Part Models. *2012 Ieee Intelligent Vehicles Symposium (Iv)***,** 1035-1042.

COHEN, H., FU, G., DEKELBAB, W. & MOSES, F. 2003. Predicting Truck Load Spectra under Weight Limit Changes and Its Application to Steel Bridge Fatigue Assessment. *Journal of Bridge Engineering,* 8**,** 312-322.

DALAL, N. & TRIGGS, B. 2005. Histograms of oriented gradients for human detection. *2005 IEEE Computer Society Conference on Computer Vision and Pattern Recognition, Vol 1, Proceedings***,** 886-893.

DARLINGTON, R. B. 1970. Is Kurtosis Really "Peakedness?". *The American Statistician,* 24**,** 19-22.

DAWE, P. 2003. *Research perspectives: Traffic loading on highway bridges*, Thomas Telford.

DECARLO, L. T. 1997. On the meaning and use of kurtosis. *Psychological methods,* 2**,** 292.

DITLEVSEN, O. & MADSEN, H. O. 1994. Stochastic vehicle-queue-load model for large bridges. *Journal of engineering mechanics,* 120**,** 1829-1847.

ENRIGHT, B., CAREY, C. & CAPRANI, C. C. 2013. Microsimulation Evaluation of Eurocode Load Model for American Long-Span Bridges. *Journal of Bridge Engineering,* 18**,** 1252-1260.

FELZENSZWALB, P., MCALLESTER, D. & RAMANAN, D. 2008. A discriminatively trained, multiscale, deformable part model. *2008 Ieee Conference on Computer Vision and Pattern Recognition, Vols 1-12***,** 1984-+.

FELZENSZWALB, P. F., GIRSHICK, R. B., MCALLESTER, D. & RAMANAN, D. 2010. Object Detection with Discriminatively Trained Part-Based Models. *Ieee Transactions on Pattern Analysis and Machine Intelligence,* 32**,** 1627-1645.

FOONG, M. F. & CAPRANI, C. 2016. Victoria traffic modelling for bridge loading application.

FRENZE, J. F. 2002. A VIDEO-BASED METHOD FOR THE DETECTION OF TRUCK AXLES. *NIATT Report,* No. 2.

FUNG, Y. F., LEE, H. & ERCAN, M. F. 2006. Image processing application in toll collection. *Recent Advances in Engineering and Computer Science 2007,* 62**,** 85-90.

FWA, T. F. & LI, S. 1995. Estimation of Lane Distribution of Truck Traffic for Pavement Design. *Journal of Transportation Engineering-Asce,* 121**,** 241-248.

GONZALEZ, R., WOODS, R. & EDDINS, S. 2009. Digital Image Processing Using Matlab Gatesmark Publishing.

HARMAN, D. J., DAVENPORT, A. G. & WONG, W. S. S. 1984. Traffic loads on medium and long span bridges. *Canadian Journal of Civil Engineering,* 11**,** 556-573.

HELBING, D., TREIBER, M., KESTING, A. & SCHöNHOF, M. 2009. Theoretical vs. empirical classification and prediction of congested traffic states. *The European Physical Journal B-Condensed Matter and Complex Systems,* 69**,** 583-598.

HENDERSON, W. 1954. British highway bridge loading. *Proceedings of the Institution of Civil Engineers,* 3**,** 325-350.

HEYWOOD, R. 1995. Live loads on Australian bridges-statistical models from weigh-in-motion data. *TRANSACTIONS OF THE INSTITUTION OF ENGINEERS, AUSTRALIA, CIVIL ENGINEERING.*

HEYWOOD, R. & ELLIS, T. Australia's new bridge design load-improving transport productivity. 5th International Symposium on Heavy Vehicle Weights and Dimensions, Australian Road Research Board, Melbourne, Mar, 1998.

HEYWOOD, R., GORDON, R. & BOULLY, G. 2000. Australia's bridge design load model: Planning for an efficient road transport industry. *Transportation Research Record: Journal of the Transportation Research Board***,** 1-7.

HIROSE, K., TORIU, T. & HAMA, H. Accurate Estimation of Wheel Center Points for Estimate of Vehicle Baseline Length in a Circular Fisheye Image. Innovative Computing, Information and Control (ICICIC), 2009 Fourth International Conference on, 2009. IEEE, 306-309.

IVY, R., LIN, T., MITCHELL, S., RAAB, N., RICHEY, V. & SCHEFFEY, C. 1954. Live loading for long-span highway bridges. *American Society of Civil Engineers Transactions*.

JACOB, B. & LABRY, D. Evaluation of the effects of heavy vehicles on bridges fatigue. Proceedings 7th International Symposium on Heavy Vehicle Weights & Dimensions, 2002.

JACOBS & ARUP 2009. Forth Replacement Crossing: Main Crossing (Bridge) Scheme Assessment Report Development of Options.

JIA, Z., BALASURIYA, A. & CHALLA, S. Target tracking with Bayesian fusion based template matching. Image Processing, 2005. ICIP 2005. IEEE International Conference on, 2005. IEEE, II-826.

JIANG, F. & LIN, X. A Learning Based Approach for Vehicle Detection. TENCON 2006. 2006 IEEE Region 10 Conference, 2006. IEEE, 1-4.

KASTRINAKI, V., ZERVAKIS, M. & KALAITZAKIS, K. 2003. A survey of video processing techniques for traffic applications. *Image and vision computing,* 21**,** 359-381.

KESTING, A. & TREIBER, M. 2008. Calibrating car-following models by using trajectory data: Methodological study. *Transportation Research Record: Journal of the Transportation Research Board***,** 148-156.

KESTING, A., TREIBER, M. & HELBING, D. 2007. General Lane-Changing Model MOBIL for Car-Following Models. *Transportation Research Record: Journal of the Transportation Research Board,* 1999**,** 86-94.

KITCHENHAM, B. A., PICKARD, L. M., MACDONELL, S. G. & SHEPPERD, M. J. 2001. What accuracy statistics really measure [software estimation]. *IEE Proceedings - Software,* 148**,** 81-85.

KITE, S., HUSSAIN, N. & CARTER, M. 2011. Forth Replacement Crossing – Scotland, UK. *Procedia Engineering,* 14**,** 1480-1484.

KULICKI, J. M. & MERTZ, D. 2006. Evolution of vehicular live load models during the interstate design era and beyond. *Transportation Research Circular E-C10***,** 1-26.

LARNACH, W. J. 1964. *Influence lines for statically indeterminate plane structures,* London, London : Macmillan.

LEON, L. C. & HIRATA JR, R. Vehicle detection using mixture of deformable parts models: Static and dynamic camera. Graphics, Patterns and Images (SIBGRAPI), 2012 25th SIBGRAPI Conference on, 2012. IEEE, 237-244.

LEWIS, J. P. Fast normalized cross-correlation. Vision interface, 1995. 120-123.

LI, S., WANG, B., ZHENG, Z. H. & WANG, H. L. Multi-view vehicle detection in traffic surveillance combining hog-hct and deformarle part models. Wavelet Analysis and Pattern Recognition (ICWAPR), 2012 International Conference on, 2012. IEEE, 202-207.

LI, Y., BAO, W. & GUO, X. 1997. *Structural Reliability and Probability Limit Design of Highway Bridges,* Beijing, China Communications Press [In Chinese].

LI, Y., ER, M. J. & SHEN, D. Y. 2015. A Novel Approach for Vehicle Detection Using an AND-OR-Graph-Based Multiscale Model. *Ieee Transactions on Intelligent Transportation Systems,* 16**,** 2284-2289.

LIPARI, A. 2013. *Micro-simulation modelling of traffic loading on long-span bridges.* University College Dublin.

LIPARI, A., CAPRANI, C. C. & OBRIEN, E. J. 2017. A methodology for calculating congested traffic characteristic loading on long-span bridges using site-specific data. *Computers & Structures,* 190**,** 1-12.

LIU, X., JIANG, W., XIE, J. & JIA, Y. An image template matching method using particle swarm optimization. Computational Intelligence and Industrial Applications, 2009. PACIIA 2009. Asia-Pacific Conference on, 2009. IEEE, 83-86.

MARIA, J. D., CAPRANI, C. C. & GUO, D. 2018. Long span bridges – current age & design life – a global survey. *9th International Conference on Bridge Maintenance, Safety and Management (IABMAS 2018).* Melbourne.

MCKINNON, A. C. 2005. The economic and environmental benefits of increasing maximum truck weight: the British experience. *Transportation Research Part D: Transport and Environment,* 10**,** 77-95.

MINISTRY OF COMMUNICATIONS 2004. JTG D60 – 2004 General Code for Design of Highway Bridges and Culverts Beijing.

MINISTRY OF TRANSPORT 2015. JTG D60 – 2015 General Specification for Design of Highway Bridges and Culverts Beijing.

MOSHIRI, M. & MONTUFAR, J. Comparison of International Bridge Formulae and the Analysis of Imposed Bridge Load Stresses for Consideration in the Development of a European Bridge Formula TRB 2014 Annual Meeting, 2013.

NATIONAL ASSOCIATION OF AUSTRALIAN STATE ROAD AUTHORITIES 1976. *NAASRA bridge design specification*, National Association of Australian State Road Authorities.

NOWAK, A. S. 1993. Live load model for highway bridges. *Structural safety,* 13**,** 53-66.

NOWAK, A. S. 1995. Calibration of LRFD bridge code. *Journal of Structural Engineering,* 121**,** 1245-1251.

NOWAK, A. S., LUTOMIRSKA, M. & SHEIKH IBRAHIM, F. 2010. The development of live load for long span bridges. *Bridge Structures,* 6**,** 73-79.

OBRIEN, E. J., BORDALLO-RUIZ, A. & ENRIGHT, B. 2014. Lifetime maximum load effects on short-span bridges subject to growing traffic volumes. *Structural Safety,* 50**,** 113-122.

OBRIEN, E. J., HAYRAPETOVA, A. & WALSH, C. 2012. The use of micro-simulation for congested traffic load modeling of medium- and long-span bridges. *Structure and Infrastructure Engineering,* 8**,** 269-276.

OBRIEN, E. J., LIPARI, A. & CAPRANI, C. C. 2015. Micro-simulation of single-lane traffic to identify critical loading conditions for long-span bridges. *Engineering Structures,* 94**,** 137-148.

OROSZ, G., WILSON, R. E. & STÉPÁN, G. 2010. Traffic jams: dynamics and control. *Philosophical Transactions of the Royal Society A: Mathematical, Physical and Engineering Sciences,* 368**,** 4455-4479.

PEARSON, K. 1905. "Das Fehlergesetz und Seine Verallgemeinerungen Durch Fechner und Pearson." A Rejoinder. *Biometrika,* 4**,** 169-212.

PEARSON, R. A. & BAYLEY, C. 1997. Economic Impacts of Higher Bridge Design Loadings, Stage I: Vehicle Alternative and Benefits. *AUSTROADS Project RUM.H.96 working paper.*

RADFORD, C. & HOUGHTON, D. Vehicle detection in open-world scenes using a hough transform technique. Image Processing and its Applications, 1989., Third International Conference on, 1989. IET, 78-82.

RAZAVI, N., GALL, J. & VAN GOOL, L. Scalable multi-class object detection. Computer Vision and Pattern Recognition (CVPR), 2011 IEEE Conference on, 2011. IEEE, 1505-1512.

RICKETTS, N. & PAGE, J. 1997. Traffic data for highway bridge loading. *TRL REPORT 251.*

SAO, A. K. & YEGNANARAYANA, B. 2007. Face verification using template matching. *IEEE Transactions on information Forensics and Security,* 2**,** 636-641.

STANDARDS AUSTRALIA 2017. AS 5100.2:2017 Bridge design. *Design loads.* Standards Australia.

TAPLIN, G. & AL-MAHAIDI, R. 1997. Methods of analysis and strengthening for shear capacity of cast-in-place T-beam bridges. *Report to VicRoads*.

TREIBER, M., HENNECKE, A. & HELBING, D. 2000. Congested traffic states in empirical observations and microscopic simulations. *Physical Review E.*

TREIBER, M. & KESTING, A. 2013. *Traffic flow dynamics*.

TURKSTRA, C. J. & MADSEN, H. O. 1980. Load combinations in codified structural design. *Journal of the Structural Division,* 106**,** 2527-2543.

VILLORIA, B., VEIE, J., HOLTBERGET, S. & JENA, P. Multi span suspension bridge on floating foundations – behaviour under operation. IABSE Symposium, 2017a Vancouver. 509-516.

VILLORIA, B., VEIE, J., HOLTBERGET, S., JENA, P., CATO, D. & MADSEN, P. Concept overview of a multi-span suspension bridge on floating foundations. IABSE Symposium, 2017b Vancouver. 3037-3044.

WANG, N., O'MALLEY, C., ELLINGWOOD, B. R. & ZUREICK, A.-H. 2011. Bridge rating using system reliability assessment. I: Assessment and verification by load testing. *Journal of Bridge Engineering,* 16**,** 854-862.

WANG, Z. 2005. The Development History of the Vehicle Load Standard in Our Country's Road and Bridge Design Regulations. *Communications Standardization***,** 32-33 [In Chinese].

WORLD HEALTH ORGANIZATION. 2017. *Number of registered vehicles: Situation and trends* [Online]. Available: http://www.who.int/gho/road_safety/registered_vehicles/number_text/en/# [Accessed 18/12/2017].

ZHOU, J., RUAN, X. & CAPRANI, C. C. 2015. Characteristic of traffic loading response for multi span large bridge. *In:* MAGALHAES, P. P. A. F. (ed.). CRC Press.

APPENDIX: DIGITAL DATA

The digital data involved in this work is available at *monash.figshare*:

https://figshare.com/s/f5fc9a7fb4b5e785e294

All data are compressed into a zip file. Its directory structure and brief description are listed below:

Item Name	Description
Folder: **_BTLS_**	This folder contains in-house BTLS traffic file generator. It is used to generate required traffic data file for SIMBA use. Users can define the traffic by nominating the truck distribution, traffic volume, lane distribution and so on.
Folder: **_DPM_**	This folder contains the DPM code modified for wheel detection. The test file and result are also included.
Folder: **_InfluenceLines_**	This folder contains the ILs used in the test, such as IL from GGB and Queensferry. Besides, the general IL generator is also included. It is the basis of GILF.
Folder: **_Matlabs_**	This folder contains all the script and functions used in this work, such as extrapolation and metric calculation. They are used to process the raw data.
Folder: **_Simba Files_**	This folder contains all the raw data and road topology setup file for SIMBA use.
File: **_concentration example.xlsx_**	This file is an example file showing how to calculate the concentration metric step by step.
File: **_Iteration for axle no.xlsx_**	This file shows how the equivalent number of axle come from.
File: **_Standard vehicle data.xlsx_**	This file provides the standard vehicles in numerical format. Ready to use for MATLAB.